A study of the synthesis of CoAlO and the inducement of reactions and rearrangements in the solid state by mechanical milling.

Thesis

UNRESTRICTED

A STUDY OF THE SYNTHESIS OF $CoAl_2O_4$ AND THE INDUCEMENT OF REACTIONS AND REARRANGEMENTS IN THE SOLID STATE BY MECHANICAL MILLING

Paul G Wynn.

BSc. (HONS), **M.R.S.C.**

Thesis submitted for the Degree of Doctor of Philosophy

Department of Chemistry

The Open University

2005

DATE OF SUBMISSION 17 NOVEMBER 2005

DATE OF AWARD 27 MARCH 2006

DECLARATION

The work reported in this thesis was carried out solely by me and where the work of others is cited, it is fully acknowledged. No part of this work has been submitted for the award of a degree in any other Institution.

Paul Wynn

ACKNOWLEDGEMENTS

- Professor F.J. Berry at The Open University, for his kind help and supervision throughout this research.
- Dr D. Eden, at Cookson Matthey Ceramics plc, Meir, for his assistance and support.
- Professor S. Mørup and Dr J.Z. Jiang at The Technical University of Denmark, for their help and assistance during my visit to Denmark.
- Dr. T. Rayment, for allowing me to collect high temperature X-ray powder diffraction data *in situ* in The University of Cambridge
- The technical staff at the Department of Chemistry in The Open University, for their help during this work.
- The European Commission Socrates Student Mobility Programme.
- Cookson Matthey Ceramics plc, for their financial support.
- My friends and relatives whom have given me persistent encouragement throughout and especially in the later stages of this work.

ABSTRACT

The nature of commercial samples of Co_3O_4, γ-$Al(OH)_3$, γ-AlO(OH) and α-Al_2O_3 have been examined and the phase changes undergone by these materials as a function of heating in air examined *ex situ* and *in situ* by X-ray powder diffraction and by thermal analysis. The thermally induced reaction between the pre-milled cobalt- and aluminium-containing species, to form $CoAl_2O_4$ with a spinel-related structure, has been investigated. Pre-milling of the reactants facilitates the formation of $CoAl_2O_4$ in shorter periods of time. An attempt to produce a series of phases in the solid solution series $Co_xAl_{3-x}O_4$ was not successful.

Nanoparticle calcium stannate ($CaSnO_3$) and calcium titanate ($CaTiO_3$) have been prepared by the mechanical milling of mixtures of calcium (II) oxide with tin (IV) oxide or titanium (IV) oxide. The reaction of the rutile form of titanium (IV) oxide with calcium (II) oxide is faster than that between the anatase modification of titanium (IV) oxide and calcium (II) oxide.

Nanostructured partially inverse spinel-related zinc ferrite ($ZnFe_2O_4$) particles have been synthesised from bulk normal spinel-related $ZnFe_2O_4$ by means of mechanical milling using a planetary ball mill. This process is shown by a combination of X-ray powder diffraction and Mössbauer spectroscopy to result in a rearrangement of the zinc and iron ions in the A and B sub lattices with the resultant change of magnetic properties from antiferromagnetic to ferromagnetic or ferrimagnetic.

The changes in the local coordination of aluminium in γ-$Al(OH)_3$ when milled with zinc oxide has been monitored by ^{27}Al MAS NMR spectroscopy. The results give evidence for the onset of the formation of a precursor to spinel-related $ZnAl_2O_4$ and may have implications for the more facile formation of $CoAl_2O_4$ by the calcination of pre-milled mixtures of cobalt- and aluminium-containing oxides.

TABLE OF CONTENTS

Chapter 1

Introduction

1.1 Aims

The aims of the work reported in this thesis have been to:

- examine the phase changes undergone by some cobalt- and aluminium–oxides, -hydroxides and -oxyhydroxides when heated in air.
- investigate the thermally induced reaction between pre-milled cobalt- and aluminium-containing species to form the blue, spinel-related cobalt aluminate of composition $CoAl_2O_4$.
- investigate the effect of planetary ball milling upon the solid state reaction of Co_3O_4 and aluminium-oxides, -hydroxides and -oxyhydroxides.
- investigate the formation of other mixed metal oxides with a perovskite-related structure by mechanical milling.
- investigate the effect of mechanical milling on the cation distribution and the magnetic properties of $ZnFe_2O_4$.
- Investigate the changes to the local coordination of aluminium in γ-$Al(OH)_3$ when milled with zinc oxide.

1.2 Introduction

The work reported in this thesis concerns the use of mechanical milling to either - initiate the first steps of a chemical reaction, - take a chemical reaction to completion, - induce rearrangements of ions in the solid state.

The results presented in Chapter 4 are associated with the thermally induced reaction between cobalt- and aluminium-oxides, -hydroxides and -oxyhydroxides to form cobalt aluminate. The nature of the various cobalt-

and aluminium-oxides, -hydroxides and -oxyhydroxides used in the reactions is investigated in Section 4.1. and the formation of cobalt aluminate by calcination of the pre-milled reactants is addressed in Section 4.2. The specific effects of pre-milling the reactants prior to calcination are discussed in Section 4.3.

The use of mechanical milling to take a chemical reaction to completion and to induce structural rearrangements in the solid state are collected in Chapter 5. The direct formation of calcium-stannate and -titanate by mechanical milling of calcium- and either tin- or titanium-oxides is discussed in Section 5.1. and the rearrangement of ions resulting from the milling of zinc ferrite and a mixture of zinc oxide and aluminium hydroxide in Sections 5.2., 5.3. and 5.4.

The principles of mechanical milling and a discussion of the oxides, hydroxides and oxyhydroxides used in the work reported in this thesis are contained in subsequent sections of this chapter.

1.3 Mechanical milling

1.3.1 Background

Mechanical milling has been widely used in industry for many years, primarily as a method of reducing the particle size of solid materials, increasing intimacy of mixing and as a method of powder pigment dispersion in the paint industry[1].

Over the last twenty five years, the laboratory use of ball milling has evolved from a standard technique of powder metallurgy, used primarily for particle

size reduction, to a method for the preparation of alloys with compositions far from stoichiometry and, more recently, other inorganic materials[2].

Introductory perspectives[3,4] on mechanical alloying based on milling techniques were first published by Benjamin in the 1970's and the extent of the field was subsequently reviewed by The American Society for Metals Committee on Milling[5]. It is now recognised that, as well as a wide range of alloys, mechanical milling treatments are suitable for the synthesis of metal-metal oxide nanocomposite transition metal compounds[6,7,8], nanocrystalline materials[9,10], non-metallic inorganic materials[11], materials far from equilibrium such as metastable solid solutions of metals, e.g. iron-copper systems[12], mixed oxides such as α-Fe_2O_3-SnO_2[13] and CeO_2-ZrO_2[14], metal sulphides such as FeS[15] and more recently the formation of titanium hydride from titanium and gaseous hydrogen[16]. Correspondingly, terms such as mechanical alloying, mechanochemistry and mechanosynthesis have become increasingly common within the materials science and condensed physics literature.

1.3.2 Milling devices

The first overall description and analysis of the different mills used in mechanical alloying was presented by Maurice and Courtney[17] in 1990. The majority of mills used for experimental research and for the production of small batches of materials are variants of the ball mill. The high energies associated with heavy balls impacting upon powdered material produces, for example, the cold welding needed for the formation of alloys in ductile metal systems or, in the case of brittle materials, the force required for particle size reduction. The mills currently used in the field of mechanical alloying include

attriators, vibratory mills, rotary (horizontal) mills, planetary (vertical) mills and bead mills.

Numerous studies[6,18,19,20,21,22] have reported on the mechanics and physics of the milling process, identifying factors such as ball mass, impact velocity, impact angle and impact deviation, as well as the geometrical proportions of the milling chamber, the ratio of ball to powder mass, and the filling volume to influence the performance of the mill and the properties of the resulting materials.

Milling is usually performed in a horizontal cylindrical container or vial into which the appropriate ball charge or milling media are placed together with the constituent powders or mill base and, in the case of wet milling, a liquid lubricant. The cylinder is rotated at a critical rate[19], such that the contents are held against the sides of the vial by centrifugal forces until falling as they approach the top of the vial. Collision of the milling media, both with the walls of the vial and with other media, is used to grind the contents. This motion is further illustrated in Figure 1.3.1.

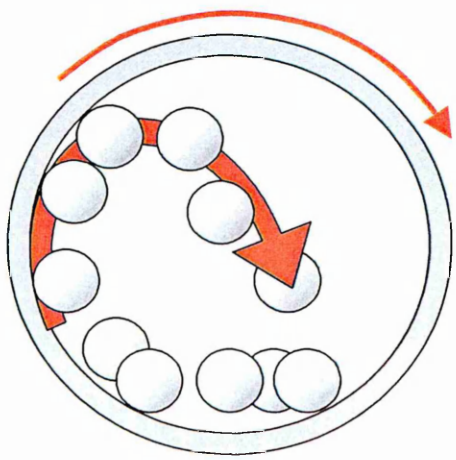

Figure 1.3.1 –Diagram showing the motion of balls within a typical ball mill.

Planetary ball milling, which has been used for most of the work reported in this thesis, is a variation to the standard ball milling technique. Planetary ball mills are commonly used for mechanical milling applications that require greater impact energies than can be achieved using the other methods. In this case the vial is mounted vertically upon a supporting "sun" wheel. Centrifugal forces caused by the rotation of the "sun" wheel and the autonomous counter-rotation of the grinding vials both act on the contents. This action causes centrifugal forces to alternately roll the contents on the inner wall of the vial and then throw them across the container at much higher velocities and a higher rate than is achievable using a conventional ball mill. Whilst this motion initially appears more complex than within a normal ball mill, the result is the same as a normal ball mill operating under an increased gravitational force. A photograph of a planetary ball mill showing the "sun" wheel and counter rotating milling vials is shown in Figure 1.3.2.

Bead milling[1] is another variation of ball milling and uses small beads of 1-3 mm diameter. This technique, developed for use in the paint industry over forty years ago, has essentially replaced other methods for dispersion of extremely small powder particles, e.g. paint pigments, within a liquid carrier to form suspensions and slurries. Particles of fine powders tend to form large agglomerates that may consist of thousands of smaller, primary particles and which may be efficiently dispersed using bead milling techniques[1].

The greater number of smaller milling beads results in a greatly increased number of bead collisions as compared to the other milling methods. Since the clusters do not require large forces to separate the constituent particles, this method is far more effective at dispersion of powder agglomerates. Some

modern bead mills are also highly effective at primary particle size reduction[1] to yield a mean diameter of less than 1 μm. Industrial bead mills usually consist of a stationary drum in which high-speed paddles act to agitate the milling beads and mill-base. These have an advantage in industrial applications since they are normally operated as a continuous flow rather than batch process. A representation of a typical industrial bead mill is shown in Figure 1.3.3.

Figure 1.3.2 - Photograph of a Frisch Pulverisette planetary ball mill, showing the "sun" wheel and two counter-rotating milling vials.

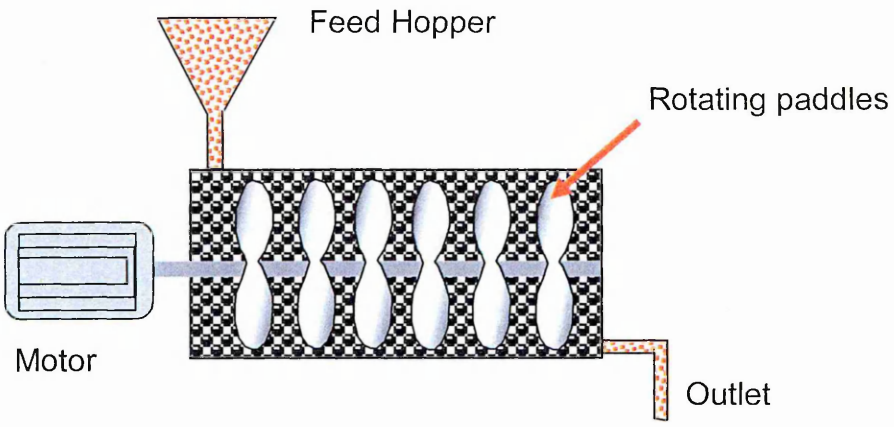

Figure 1.3.3 - Diagrammatic representation of an industrial bead mill.

1.3.3 Mechanisms of milling

An understanding of mechanical milling and its effect upon reactions is not fully developed. In the case of high-energy ball milling techniques, Davies, McDermott and Koch[2] proposed that the alloying of brittle powders within a mechanical mill is the result of repeated deformation, fracture and cold welding of particles. In this case the rates of welding and fracturing are in equilibrium. In contrast, conventional ball milling in a low energy environment gradually reduces the particle size by a process of attrition. However, Shrewman and Sundararajan[23] demonstrated that the competing processes of fracture and cold welding also occur in conventional ball milling but are normally inhibited by the use of milling liquids or surfactants. The effects of the cold welding are minimal until the powder reaches a particle size of the order of one micrometer in diameter.

In systems containing ductile components, plastic deformation allows alloying of materials[24], e.g. body centred cubic brass can be formed from face centred

cubic copper and hexagonally close packed zinc[25], and in the case of ductile-brittle systems, e.g. oxide dispersion in metals, milling results in the brittle phase being encapsulated by the ductile one. Brittle-brittle systems are less well understood. However, by using liquid nitrogen cooled equipment, Davies, McDermott and Koch[2] have suggested that the mechanical alloying of brittle systems, e.g. the formation of diamond-cubic structured substitutional solid solutions in the germanium-silicon system[25] are thermally activated processes and that collision phenomena such as surface melting or temperature enhanced diffusion, micro-deformation and temperature enhanced deformation are involved in the mechanism. The local temperature of particles during milling has been calculated[2] to reach a maximum of 200-300 °C above ambient, values far lower than the melting points of most metal oxides.

The reaction of metal oxides using ball milling techniques have been examined by Berry[13] *et al* who have shown that systems such as α-Fe_2O_3 and SnO_2 form a metastable solid solution and, by using techniques such as Mössbauer spectroscopy, have shown that alloying occurs on a truly atomic scale. Furthermore they suggest that the high defect concentration and the chemical enthalpy of Fe^{3+}- O^{2-}- Sn^{4+} interfaces between nano-structured α-Fe_2O_3 and SnO_2 may act as the driving force for the formation of such a solid solution in an immiscible ceramic system. Jiang, Linderoth and Mørup[26] demonstrated the reversible transformation of α-Fe_2O_3 to Fe_3O_4 during ball milling and have attributed this to a mechanism that involves bond breaking during the milling process.

1.4 Metal oxides investigated in this work

1.4.1 Cobalt aluminate

Cobalt aluminate, $CoAl_2O_4$, known as Thénard's blue, has been known for many years and is still widely used as a commercial pigment within the ceramics industry. The pigment is traditionally formed by the solid state reaction between Co_3O_4 and aluminium oxyhydroxides at temperatures above 900 ^{o}C.

Cobalt aluminate is an intensely deep royal blue, highly crystalline solid that adopts a *normal* spinel crystal structure.

Normal spinels have the general formula AB_2O_4 in which A and B represent the cations. In the case of cobalt aluminate, A = Co^{2+} and B = Al^{3+}. The unit cell is based upon a cubic close packed array of 32 O^{2-} anions. Cations are located on the interstitial sites, 64 of which are tetrahedrally co-ordinated and 32 octahedrally co-ordinated. One eighth of the tetrahedral and one half of the octahedral sites are occupied, relating to the A and B sites respectively[27]. The unit cell may therefore be represented as a combination of 4 A and 4 B octants arranged alternately. These 8 octants are encompassed by a cubic close packed array of A ions as shown in Figure 1.4.1. The *normal* spinel structure can also be represented empirically as $A[B_2]O_4$, where square brackets represent the octahedral cationic sites.

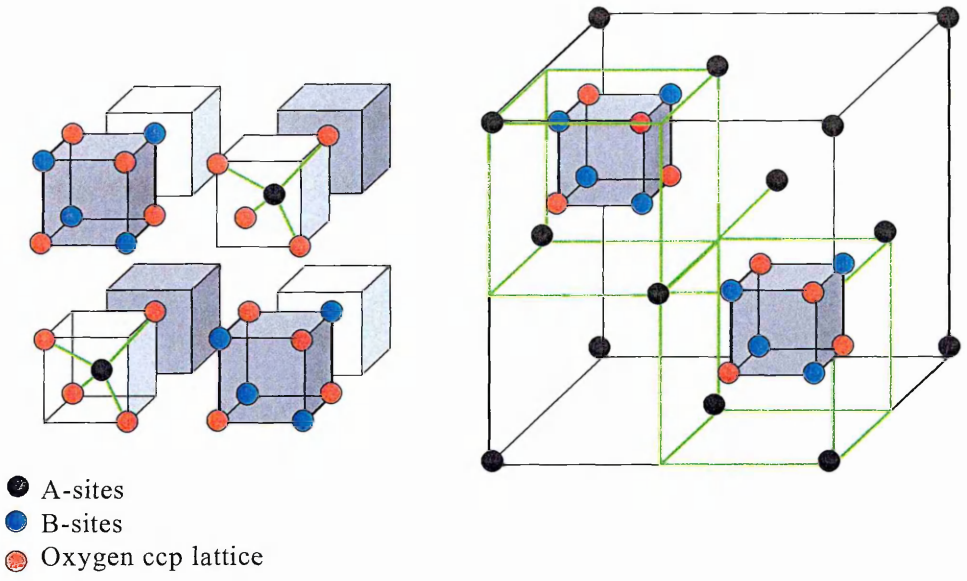

Figure 1.4.1 - Representation of the spinel structure showing AO_4 tetrahedra with B_4O_4 cubes and also the cubic close packed (ccp) lattice of oxygen with two B_4O_4 cubes.

A complicating factor is that the cationic distribution over the A and B sites may vary such that two extreme types, *normal* and *inverse* spinel may exist. In the inverse spinel extreme, half of the B^{3+} ions occupy the tetrahedral sites displacing the A^{2+} ions, which must share the octahedral sites with the remaining B^{3+} ions. This modification to the structure is represented as $B[A,B]O_4$. Between these extremes, intermediate cation distributions are possible, quantified by the inversion parameter, γ, which corresponds to the fraction of A ions on the octahedral sites. This is also sometimes represented by λ, which refers to the fraction of B ions in tetrahedral sites, and may be converted using the relationship, $\gamma = 2\lambda$.

Whilst $CoAl_2O_4$ is generally regarded as a *normal* spinel, a number of recent papers[36] have reported a small partial inversion of γ=0.155. The inversion

parameter has also been reported to be temperature dependent[28]. He and Becker[29] have recently suggested that at high temperatures, cation redistribution is more rapid than previously suspected and that consequently, the quenching methods commonly reported may give phases at low temperature which do not correspond to the cation distribution at high temperature.

It has been found[30] that the industrial production of cobalt aluminate pigments is vulnerable to fluctuation of product quality, the reasons for which are currently not understood. Many factors contribute to the colour quality of the produced pigment although few have been thoroughly investigated. The extent of reaction is believed to be crucial to the industrial production process since the presence of any excess cobalt oxides act to dull the final pigment colour, leaving a "dirty", rather than clear intense colour. There may also be undetermined physical properties of individual reagent batches or an "activation" process that may occur during the milling stages. It is considered that this activation may include some form of naturally occurring dopant or mineralising agent that promotes phase transition.

The role of mechanical milling, which is used in the industrial preparation of cobalt aluminate before the calcination process, has traditionally been envisaged as reducing the particle sizes and increasing the intimacy of mixing between the Co_3O_4 and the aluminium oxyhydroxide reagents.

Further milling after the calcination process has then been used as a method to reduce the particle size of the $CoAl_2O_4$ product.

The work reported in Chapter 4 of this thesis, concerns the formation of cobalt aluminate by the calcination of pre-milled mixtures of reagents with a view to

monitoring the changes, which occur both in the pre-milling stage and during calcination.

It should be noted that both the *pre-*, and the *post-* calcination millings are crucial to the final colour quality. Optical properties of pigments strongly depend on the microstructure[31] and it has been shown that characteristics such as size and shape of particles contribute to the final pigment quality.

The cause of the intense royal blue colour of cobalt aluminate is not entirely clear in the literature[32], but seems to be the result of electronic transitions within the material that occur at visible wavelengths.

The electronic transitions that may cause colour in solids are[32];

- an electron within an inner shell may be promoted to another higher energy level within the localised shells of the same atom. These transitions are typically associated with d-d and f-f transitions and with defects or holes in the crystal structure, which form "colour centres".
- an electron may be promoted from the localised inner shells of one atom to the localised inner shells of an adjacent atom. These transitions are known as charge transfer and generally result in intense colours. Charge transfer within mixed valence transition metal compounds are well known.
- an electron may be promoted from the localised shells of an atom to a de-localised or conduction band, which is present throughout the solid. These transitions usually require the absorption of high energies.
- an electron may be promoted from one energy band (e.g. valence band), to another band of higher energy (e.g. conduction band). These transitions are generally present only in semiconductors.

The effects of d-d transitions are well known[33] to be the cause of colour in many cobalt-containing species where cobalt adopts an octahedral coordination. For example the d^6 low spin Co^{3+} ion undergoes the $t_{2g}^6 \rightarrow t_{2g}^5 e_g^1$ transition to a high spin species. However, tetrahedrally coordinated Co^{2+} in $CoAl_2O_4$ adopts a d^7 configuration. The Co^{2+} is well known[34] for its distinctive intense blue colours such as that of $[CoCl_4]^{2-}$. Hence the blue colour may be due to d-d transitions of the Co^{2+}. However, it is notable that Co_3O_4 which may also be represented as $Co^{2+}Co^{3+}{}_2O_4$ also adopts a similar spinel-related structure to that of $Co^{2+}Al_2{}^{3+}O_4$ and is black, hence the origin of colour in $CoAl_2O_4$ is not clear as has been reported previously[34] and it is possible that the cause of colour in cobalt aluminate may be a charge transfer between the cobalt and aluminium ions in the normal spinel related structure.

1.4.2 Cobalt oxides

The starting reagent used in this study, and often in the industrial preparation of cobalt aluminate pigments, is the mixed valence cobalt (II/III) oxide, Co_3O_4 or $Co^{2+}Co^{3+}{}_2O_4$.

Like cobalt aluminate, Co_3O_4 has a spinel-related crystal structure[35]. It has been suggested by Casardo and Rasines[36] that cobalt aluminate is simply a form of the mixed valence cobalt oxide in which Al^{3+} gradually substitutes Co^{3+} and that a solid solution series, including the phase $Co[CoAl]O_4$, can be formed between Co_3O_4 and alumina. The phase diagram shown in Figure 1.4.2, was produced by Bonnenberg *et al*[37], and shows the cobalt- and aluminium-oxide phases formed as a function of CoO : Al_2O_3 ratio and temperature. This shows that the pure spinel-related $CoAl_2O_4$ phase is

formed with CoO : Al_2O_3 ratios of approximately 1.0 to 0.82 at temperatures exceeding 1000 °C and that, to either side of these boundaries, excess reagent remains.

Co_3O_4 is stable in air to temperatures of *ca.* 600 °C when it undergoes a reversible reduction to the olive green cobalt (II) oxide. This has a rock-salt-related crystal structure[38] consisting of a hexagonal close packed oxygen lattice with cobalt on each octahedral site.

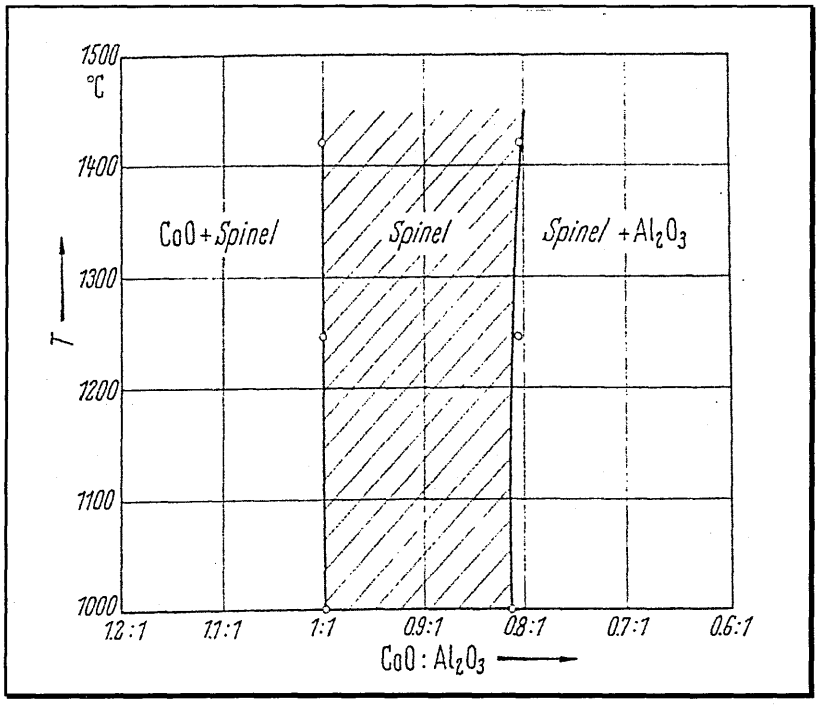

Figure 1.4.2 - Bonnenberg's phase diagram of CoO : Al_2O_3 at elevated temperatures.[37]

X-ray powder diffraction data published by the Joint Committee of Powder Diffraction Standards (JCPDS) suggests that Co_2AlO_4[39] and $CoAl_2O_4$[77] are very similar. The reflections from these materials, together with that of Co_3O_4, are shown in Figure 1.4.3. and demonstrate that by X-ray powder diffraction,

Co_3O_4 and Co_2AlO_4 are virtually indistinguishable and that $CoAl_2O_4$ may only be distinguished by the presence of a reflection at 49 $^0 2\theta$.

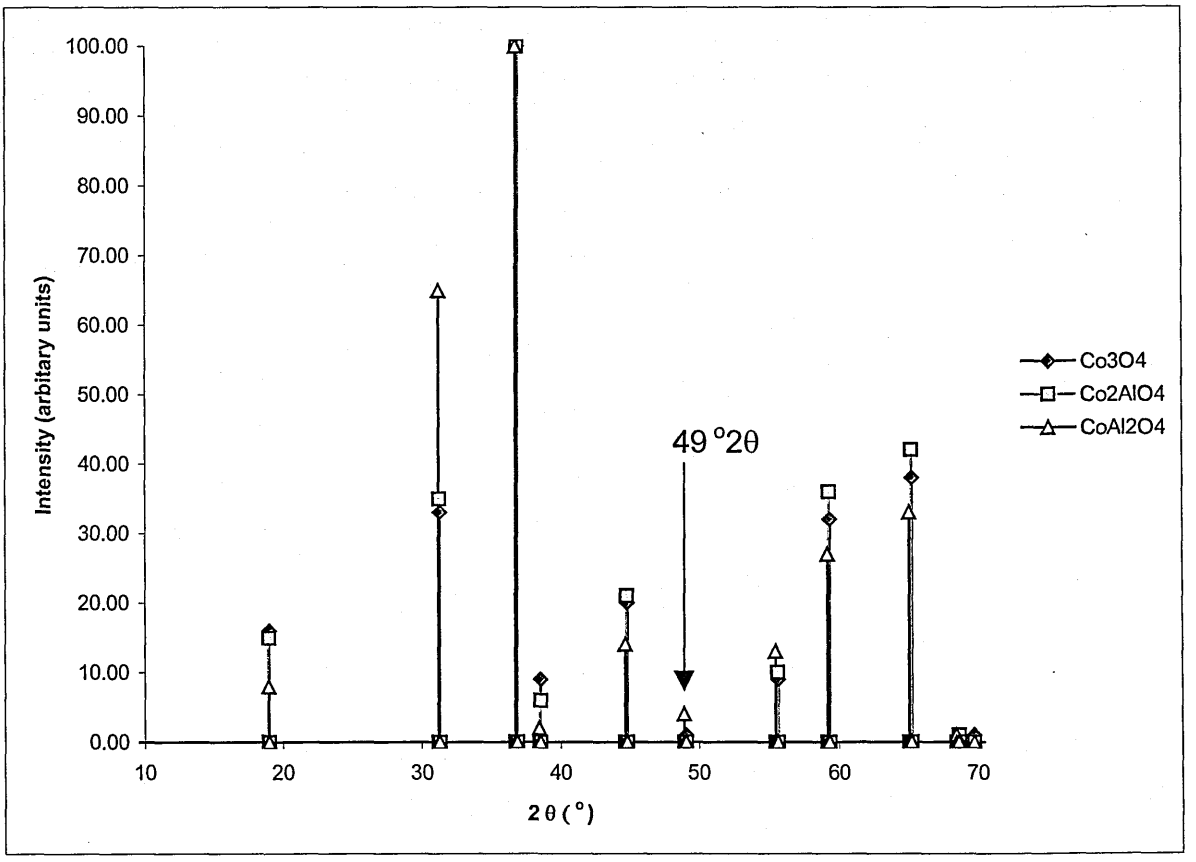

Figure 1.4.3 – Reflections recorded by X-ray powder diffraction for Co_3O_4, Co_2AlO_4 and $CoAl_2O_4$ published by the Joint Committee of Powder Diffraction Standards [40,39,41]

1.4.3 Aluminium-oxides and -oxyhydroxides

The aluminium-oxides and aluminium-oxyhydroxides form an extremely complex series of crystalline and amorphous phases which, although still the subject of some uncertainty, are of great scientific interest as catalyst supports, abrasives, engineering ceramics, fibres and sorbents.

The mineral known as bauxite, ($AlO_x(OH)_{3-2x}$) is found in large quantities and has different properties depending upon the climate of its location which leads to dehydration of the structure. One form of bauxite is γ-$Al(OH)_3$, known as gibbsite, which forms a series of different phases as dehydration occurs during heating. Some of these are described in Table 1.4.1 and their crystal structures are shown in Figure 1.4.4 to Figure 1.4.7.

γ-$Al(OH)_3$ is only stable at low temperatures and starts to form γ-AlO(OH), boehmite at *ca.* 100 °C. At *ca.* 150 °C the hydroxyl groups begin to be ejected and a series of gamma alumina, γ-Al_2O_3, phases are formed. These are present until *ca.* 1000 °C when there is a rearrangement of the oxygen lattice from a cubic close packed to a hexagonal close packed structure with the formation of the corundum, α-Al_2O_3, structure. A similar series exists in the dehydration of alpha aluminas where the oxygen lattice is hexagonal close packed throughout. These series are not inter convertible until high temperatures and the gamma phases form α-Al_2O_3 due to the major structural, and therefore energetic, rearrangement of the oxygen lattice (-20 $KJmol^{-1}$ from γ-Al_2O_3 to α-Al_2O_3)[42].

Formulae	Common name	Structure
γ-$Al(OH)_3$	Gibbsite, Aluminium -trihydrate, Hydrargillite	Cubic close packed (OH) within layers of edge sharing $Al(OH)_6$ octahedra stacked vertically via H-bonds. (See Figure 1.4.4.)
γ-AlO(OH)	Boehmite and Pseudoboehmite	Boehmite consists of planes of edge-sharing aluminium octahedra linked by hydrogen bonds. Pseudoboehmite is boehmite with small particle size and intercalated water, causing a more disordered structure. (See Figure 1.4.5.)
γ-Al_2O_3		Defect spinel with Al in $21^1/_3$ of the 16 octahedral and 8 tetrahedral sites.
α-$Al(OH)_3$	Bayerite	Corundum structure, hexagonal close packed (OH) with Al in $^2/_3$ of the octahedral sites.
α-AlO(OH)	Diaspore	Hexagonal close packed O(OH) with chains of octahedra stacked in layers with inter-connecting H-bonds and Al in the octahedral sites. (See Figure 1.4.6.)
α-Al_2O_3	Corundum	Hexagonal close packed O with Al in $^2/_3$ of the octahedral sites. (See Figure 1.4.5.)

Table 1.4.1 - The common phases of aluminium-oxides -hydroxides and -oxyhydroxides with associated structures[42].

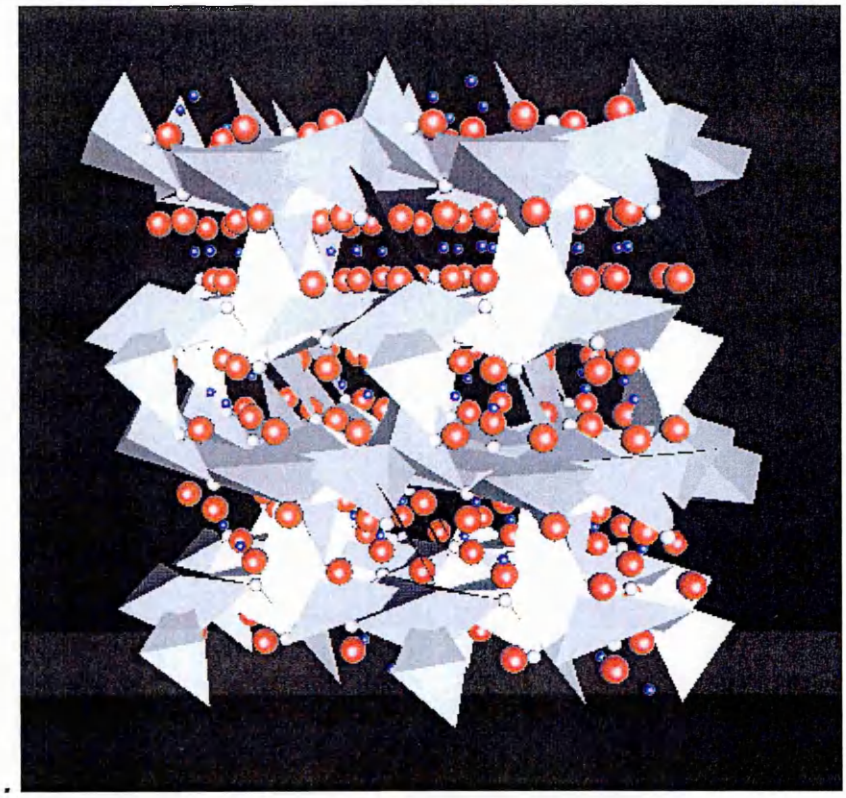

Figure ***1.4.4 - The crystal structure of gibbsite, showing cubic close packed (OH) within layers of edge sharing $Al(OH)_6$ octahedra stacked vertically and linked by hydrogen bonds.***[43]

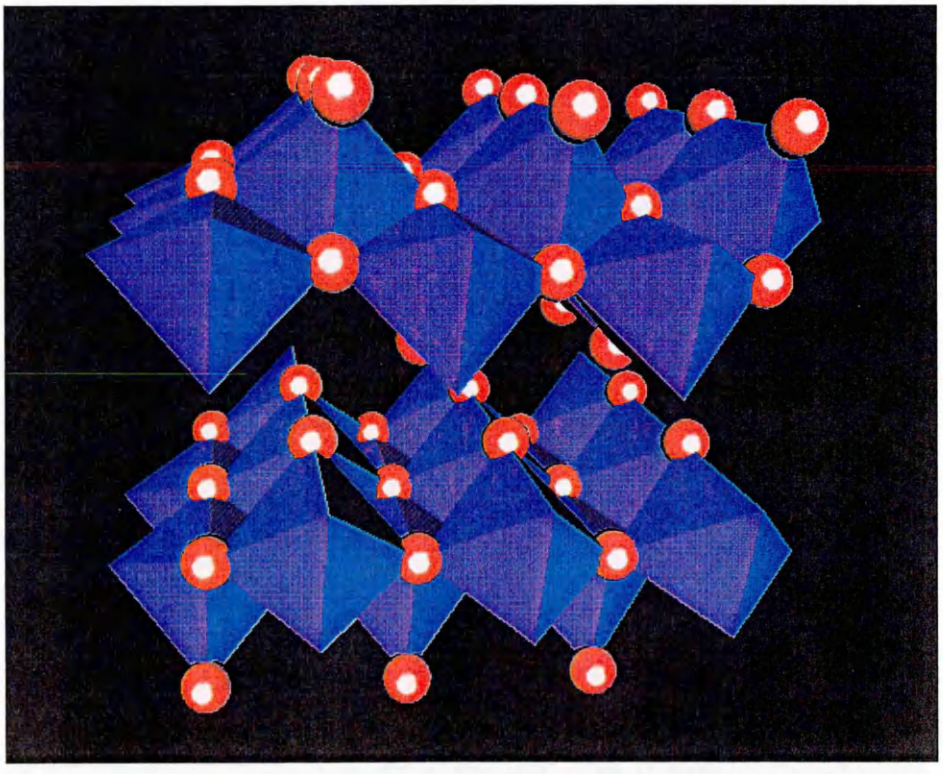

Figure ***1.4.5 - The crystal structure of boehmite, showing planes of edge-sharing aluminium octahedra linked by hydrogen bonds.***[44]

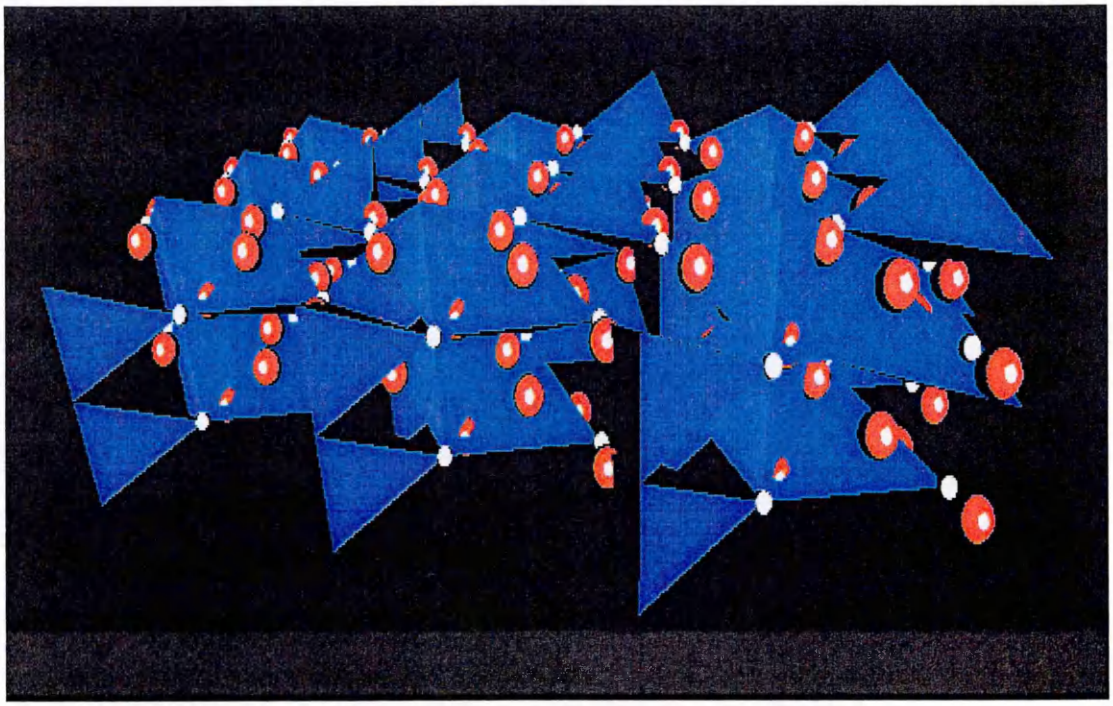

Figure ***1.4.6 - The crystal structure of diaspore,[45] showing hexagonal close packed O(OH) groups with chains of octahedra stacked in layers and linked by hydrogen bonds. Aluminium cations are in the octahedral sites.***

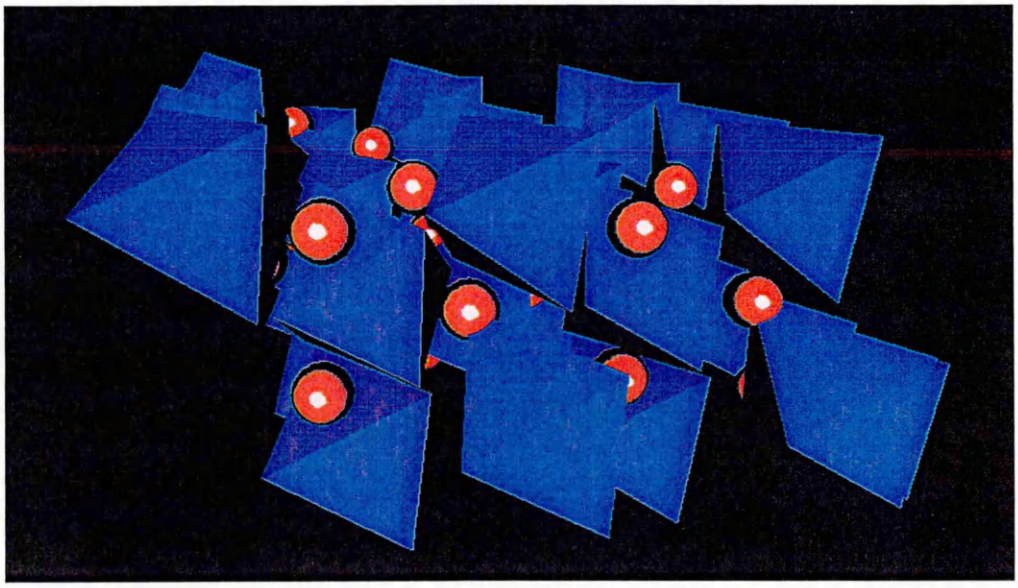

Figure ***1.4.7 - The crystal structure of corundum,[46] showing hexagonal close packed oxygen anions with aluminium cations in $^{2}/_{3}$ of the octahedral sites.***

1.4.4 Calcium stannate and calcium titanate

The perovskite oxides attract interest because of their use in thermally stable capacitors where the titanates in particular show ferroelectric and piezoelectric behavior, which renders them important for the production of compact capacitors and ceramic transducers. They are also of interest because of their potential for specific applications including superconductivity[47] and oxidation catalysis where they are industrially used as deep oxidation catalysts. More recently the catalytic properties have been tuned by subtle doping to yield good selectivity of partially reduced products, e.g. production of methanal from methanol[48].

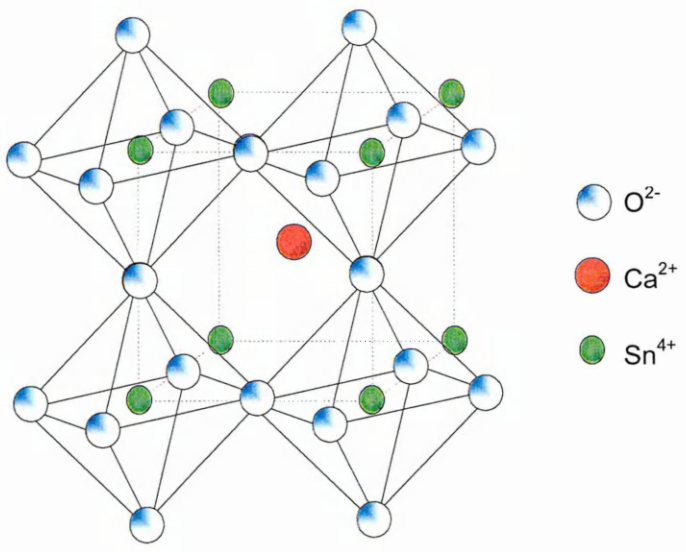

Figure 1.4.8 - Diagram showing the perovskite related structure of $CaSnO_3$ with a framework of corner linked SnO_2 octahedra and interspaced Ca^{2+} ions.

Perovskite, $CaTiO_3$, is based on a framework of corner linked TiO_2 octahedra with calcium occupying the holes between eight of these octahedra[49]. Calcium stannate, $CaSnO_3$, also has a perovskite-related structure[50] based

upon a framework of corner linked SnO_2 octahedra, a representation of which is shown in Figure 1.4.8.

1.4.5 Zinc ferrite

Zinc ferrite, $ZnFe_2O_4$, has been widely studied over recent years due to its versatile structure and wide range of physical properties[51,52,53,54]. It has a spinel-related crystal structure[55], usually considered to be of the *normal* type. The Zn^{2+} cations have a $3d^{10}$ outer shell electronic configuration and a strong preference for the tetrahedral A sites. The Fe^{3+} cations, which carry a magnetic moment due to their high spin $3d^5$ outer shell electronic configuration, remain in the octahedral B sites of the spinel lattice. Magnetic interactions therefore consist of super-exchange between Fe^{3+} in octahedral sites that are weak due to the near right-angled Fe^{3+} - O^{2-} - Fe^{3+} bond. The compound is therefore formulated $Zn^{tet}[Fe_2]^{oct}O_4$ and exhibits antiferromagnetic behaviour with a Néel temperature of approximately 10 K[56]. Recent work to form partially inverted zinc ferrites has been of great interest since the presence of Fe^{3+} cations in the tetrahedral sites and Zn^{2+} cations in the octahedral sites permits a very strong super-exchange interaction between octahedral and tetrahedral Fe^{3+} ions where the Fe^{3+} - O^{2-} - Fe^{3+} bond angle is near 125° [57]. Since zinc cations have such a strong preference for the A sites, the system must develop a non-equilibrium state in order to accommodate Fe in the A sites. This inversion has been achieved by several methods including the supercritical sol-gel (aero-gel) co-precipitation[58] and twin roller quenching methods[59].

Chapter 2

Theory of Experimental Techniques

2.1 X-ray powder diffraction (XRD)

The basis of X-ray powder diffraction has been understood since the early part of the last century and the technique is one of the most powerful methods for structural characterisation available to the physical scientist. The technique is well explained in the literature[32,60,61] and therefore only a brief explanation is described in this thesis.

2.1.1 Theory of XRD

When an X-ray beam strikes an atom the interaction between the X-radiation and the electrons in the atom results in a scattering of X-rays in all directions. If the diffracted X-rays are in phase, constructive interference can occur and if they are out of phase then destructive interference will occur. An incident X-ray beam will be diffracted by a crystal if Bragg's law[62] is obeyed.

Bragg's approach was to consider the crystals as being built in layers, or planes, such that each acts as a semi-transparent mirror. The planes allow a proportion of the X-ray beams to be reflected at the same angle as the angle of incidence (Figure 2.1.1) whilst the remaining flux is transmitted to the under-lying planes.

The incident beams 1 and 2 are reflected by planes A and B to form beams 1' and 2', the conditions under which these beams are in phase with each other is approached as follows.

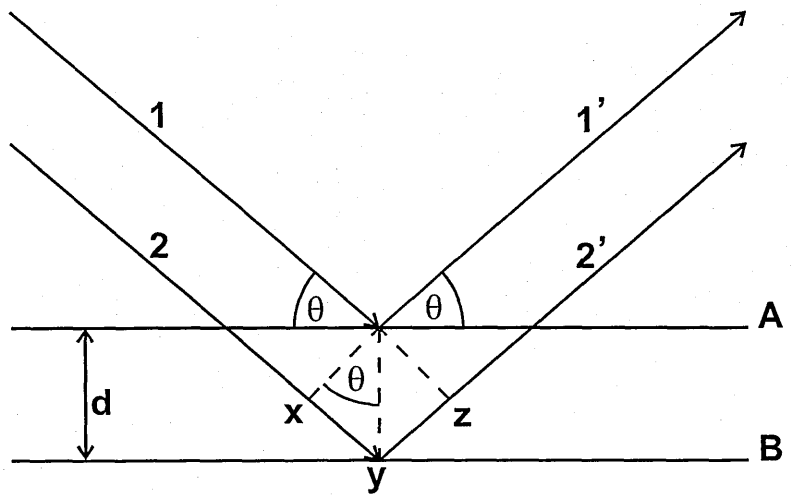

Figure 2.1.1 Schematic representation of derivation of Bragg's law.

Beam 2 2',shown in Figure 2.1.1 has to travel a further distance, xyz, as compared to beam 1 1'. For 1' and 2' to be in phase with each other, xyz must equal n, where n is an integer and is equivalent to the number of wavelengths. The perpendicular spacing, d, and angle of incidence, θ, called the Bragg angle, are related by :

$$xy = yz = d \sin \theta \qquad (2.1)$$

$$\Rightarrow \quad xyz = 2\, d \sin \theta \qquad (2.2)$$

$$\text{since} \quad xyz = n \lambda \qquad (2.3)$$

$$\Rightarrow \quad n\lambda = 2\, d \sin \theta \qquad (2.4)$$

When the above equation, (2.4) Bragg's law, is satisfied the reflected beams are in phase and thus constructively interfere. If the angle is not correct then usually interference of a destructive nature will occur. It can be seen that many solutions are possible i.e. n = 1,2,3.

2.1.2 The powder method

The basic principle of the powder method is shown in Figure 2.1.2. A monochromatic beam of X-rays strikes the powdered sample arranged randomly such that every orientation is possible. As a result, for every diffraction plane, there are some crystals correctly orientated at the Bragg angle and hence some diffraction occurs.

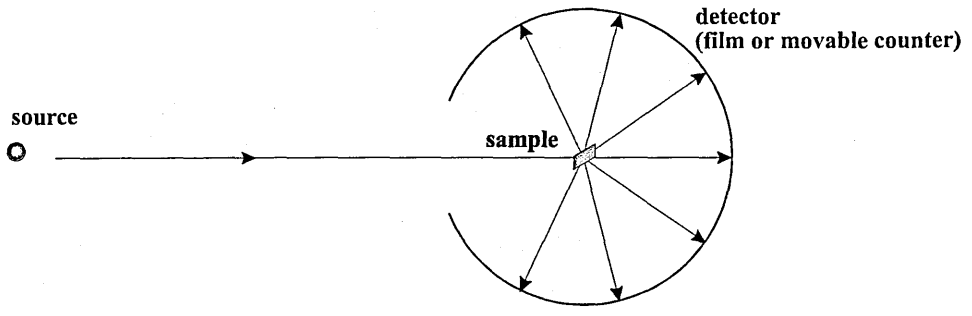

Figure 2.1.2 A schematic representation of the powder method.

The diffracted beam can be detected by one of two means, a photographic plate surrounding the sample, or a movable detector, connected to a computer. The original method, called the Debye-Scherrer method, is little used in modern X-ray diffraction practices. A modern diffractometer can collect accurate positional and intensity data both quickly and easily. This enables the phase composition to be determined in less than an hour, with the recorded pattern being matched against standard patterns.

2.1.3 Diffractometer

The collection of X-ray powder diffraction data is routinely carried out in a diffractometer, such as that shown in Figure 2.1.3.

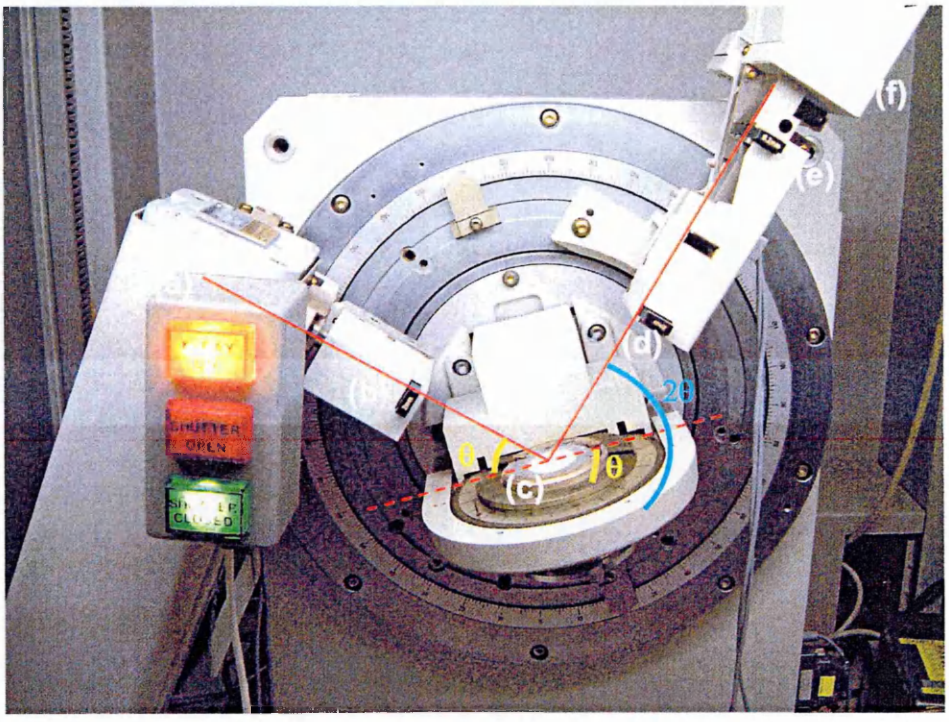

Figure 2.1.3. Photograph of the Siemens D5000 X-ray diffraction goniometer. Showing (a) X-ray source, (b) 1st collimation slit, (c) sample, (d and e) 2nd collimation slits, (f) detector.

X-rays are generated in an X-ray tube, where electrons are bombarded against a metal target, usually copper. This bombardment results in the evolution of X-rays, which are then collimated into a pencil like beam. The beam passes through the sample, which is rotating around a central axis, and is diffracted. This diffracted beam is then passed through a further set of collimation slits to remove X-ray scattering. The X-rays are then counted in a detector moving around the central axis at an angle of rotation twice that of the sample.

2.1.4 Unit cell sizes

The calculation of unit cell parameters is usually carried out using one of a variety of computer programs, an example of such a program is PowderCell[63]. Since the calculation of unit cell parameters is dependent upon the d-spacing, highly accurate data are required. As a result, X-ray powder diffraction patterns for determining unit cell parameters are measured over a long period of time (*ca.* 12 hours) with fine step sizes. Coupled to the higher resolution is an increased counting time to increase signal to noise ratio.

2.1.5 Peak intensities

There are many factors that affect the intensity of reflections recorded by X-ray powder diffraction. Some of these are described below;

Structure factor

The peak intensity is influenced by the position of the atom in the unit cell and the atom type. If an atom has a high atomic number then it will scatter X-rays better than an atom with a lower atomic number; e.g. Co scatters X-rays better than Al.

Multiplicity factor

For a cubic system where the a, b and c unit cell parameters are all equal, lattice planes such as (013), (031), (103) and (130), all have the same d-spacing. In an X-ray powder diffraction pattern the variable co-ordinate is the d-spacing, therefore reflections which give rise to the same d-spacing will be superimposed. As a result a more intense peak will be observed.

Preferred orientation

A preferred orientation can occur if a sample is not finely ground and therefore the assumption of the powder method, that crystallites are arranged randomly and that all orientations are equally possible, does not stand. This can either increase or decrease the intensity of reflections. Careful sample preparation is therefore important in order to avoid distortion of the diffraction pattern.

Temperature factor

Thermal variations of atoms cause a decrease in the observed peak intensity with an increase in background scatter. This effect is usually only important for experiments performed at high temperature.

2.1.6 Crystallite size measurement

It is possible to determine the crystallite size from X-ray powder diffraction patterns using the effects of line broadening on the diffraction pattern. The relationship between mean dimension of the crystallites in a powder, D, and the pure X-ray diffraction broadening, β, was first determined by Scherrer, and is discussed in detail by Klug and Alexander[64]. Scherrer related the mean dimension, D, to the pure diffraction broadening, β, by the equation;

$$D = \frac{K\lambda}{\beta \cos \theta} \qquad (2.5)$$

Where K is a constant approximately equal to unity, θ is the diffraction angle and λ is the wavelength of the X-radiation.

2.2 Mössbauer Spectroscopy

2.2.1 Theory of Mössbauer spectroscopy

Mössbauer spectroscopy is a technique that involves the resonant absorption and emission of γ-rays by nuclei. The phenomenon was first observed by Rudolf Mössbauer in ^{158}Ir in 1958, and has since been developed into a powerful technique available to the physical scientist.

Many detailed accounts of the theory and instrumentation of Mössbauer spectroscopy can be found in the literature[65,66,67].

In Mössbauer spectroscopy the γ-ray source consists of a solid matrix in which a radioactive isotope is embedded which then decays into the Mössbauer isotope in an excited state and subsequently relaxes with the emission of a γ-ray. For resonant absorption the energy of the γ-ray must not be influenced by nuclear recoil, to achieve this the Mössbauer nuclei are held in a rigid crystal lattice. If the energy of the nuclear recoil associated with the absorption and emission of γ-rays is small in comparison to the lowest quantised lattice vibration, recoil-free transitions suitable for a Mössbauer experiment can occur. In the case of ^{57}Fe the γ-ray energy is small (14.4 KeV), and thus recoil effects are small.

The energy of the transition between the excited and ground states of the Mössbauer nucleus is usually different in the source and the absorber. Therefore, rarely does the energy of the incident γ-ray correspond to the energy transition of the absorber Mössbauer nucleus.

The γ-ray energy is therefore modified using the Doppler effect and is achieved by vibration of the source at a velocity of millimetres per second.

Thus a Mössbauer spectrum consists of a plot of γ-ray counts against γ-ray energy.

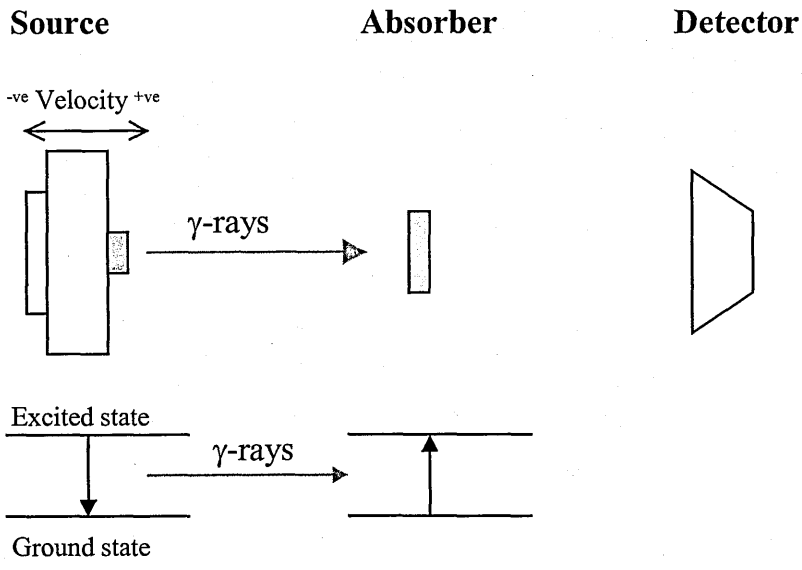

Figure 2.2.1 Schematic representation of a Mössbauer spectroscopy experiment.

A typical Mössbauer spectrum obtained from a sample in which the Mössbauer atoms are in the same cubic environment in both source and absorber is shown in Figure 2.2.2.

Differing environments about the nucleus in the absorber atom give rise to hyperfine interactions that give the Mössbauer parameters known as chemical isomer shift, quadrupole splitting and magnetic hyperfine splitting. These arise because of the electric monopole interaction, electric quadrupole interaction and magnetic dipole interaction respectively.

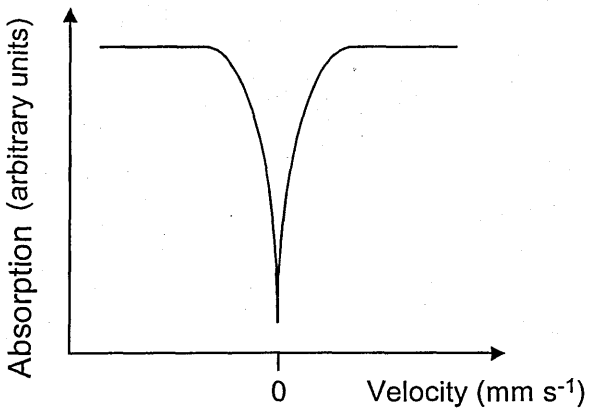

Figure 2.2.2 Typical Mössbauer spectrum obtained from a sample in which the Mössbauer atoms are in the same cubic environment in both source and absorber

2.2.2 Chemical isomer shift

To understand the origin of the isomer shift it is useful to consider a nucleus stripped of its electrons. In such a nucleus the energy of the transition between ground and excited states may be represented as E, in Figure 2.2.3(a).

If the nucleus is surrounded by electrons, a Coulombic attraction between the nuclear and the electronic charges occurs which modifies the nuclear energy levels. If in both the excited and ground states the size of the nucleus is the same, then the interaction of these states with the electrons will be the same. Hence the energy levels will be changed by the same amount, as will the energy of the transition E, in Figure 2.2.3(b). If, alternatively, the size of the nucleus in the two states is different, as usually arises, the energies of the ground and excited states will be modified to a different extent, consequently the energy of the transition will be modified to a new value E', Figure 2.2.3(c).

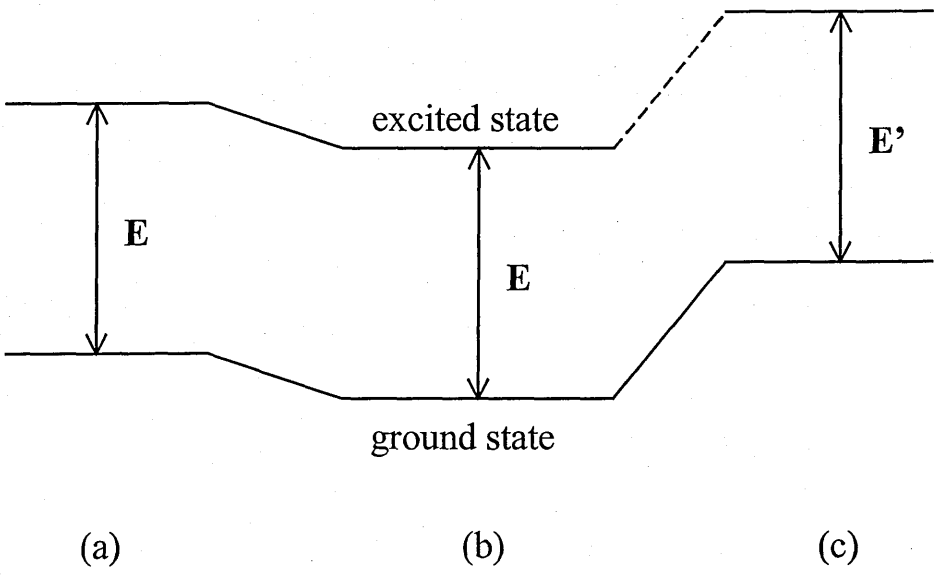

Figure 2.2.3 Nuclear energy level of (a) bare nucleus, and a nucleus where the excited and ground states are (b) the same size and (c) differing sizes.

The nuclear energy levels depend upon the electronic environment. Therefore if the source and absorber nuclei are in different electronic environments then the nuclear energy levels will be modified to differing degrees, Figure 2.2.4(a). The energy of the emitted γ-ray is then modified by the Doppler effect and the Mössbauer spectrum will exhibit a resonant absorption shifted from zero velocity, Figure 2.2.4(b). This is known as the isomer or chemical isomer shift, δ.

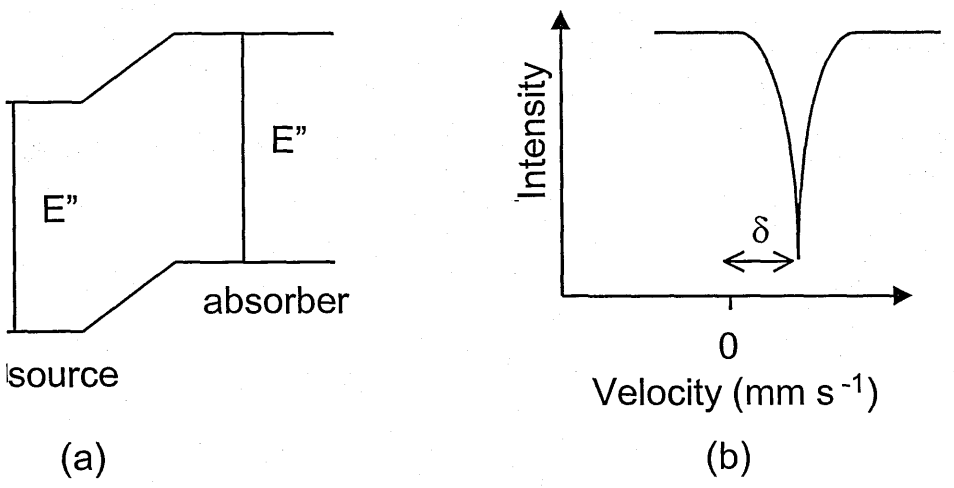

Figure 2.2.4 (a) Nuclear energy levels of source and absorber atoms in different electronic environments, (b) the resultant spectrum.

The chemical isomer shift can be related to the electronic properties by the equation

$$\delta = \text{constant}\frac{\Delta R}{R}(\Psi_o^2(o)_A - \Psi_s^2(s)_S) \qquad (2.6)$$

where $^{\Delta R}/_R$ is $(R_e - R_g)/R_g$ and R_e and R_g are the radii of the excited and ground state nuclei respectively. $\Psi_s^2(o)_A$ and $\Psi_s^2(o)_S$ are the s-electron densities at the absorber and source respectively. $\Psi_s^2(o)$ is dependent primarily on the population of the s-orbitals, but will also be influenced by the occupation of other types of orbitals. This is due to the outer electrons shielding the interaction of the s-electrons from the nucleus. For any particular source the value of $\Psi_s^2(o)_S$ will be constant, and therefore any change in the isomer shift will reflect changes in $\Psi_s^2(o)_A$. Hence information about the electronic environment of the absorber is obtained, which can then be used as a probe of oxidation state.

For ^{57}Fe Mössbauer spectroscopy the value of $^{\Delta R}/_{R}$ is negative. Hence higher s-electron densities at iron nuclei are reflected by a decrease in isomer shift. Another influence on the isomer shift in iron compounds is the effect of shielding. As d electron removal effectively increases the s electron density at the iron nuclei, iron (II) species with a d^6 configuration have a more positive isomer shift than iron (III) species with a d^5 configuration. In ^{57}Fe nuclei the magnitude of $^{\Delta R}/_{R}$ is sufficiently large for a range of isomer shifts to exist.

2.2.3 Quadrupole splitting

If a nucleus has a spin I greater than $^1/_2$ then it will have an asymmetric charge distribution, which gives rise to a nuclear quadrupole moment. It is then possible for the nuclear quadrupole moment to interact with an asymmetric electric field represented by an electric field gradient. This results in the partial or complete splitting of the nuclear energy levels. As more than one nuclear transition may occur, a multi-line Mössbauer spectrum is produced. For nuclear transitions the selection rule is $\Delta m = 0 \pm 1$. ^{57}Fe has excited and ground state spins of $^3/_2$ and $^1/_2$ respectively which, for this isotope, means that the presence of an electric field gradient gives rise to a two line spectrum, shown in Figure 2.2.5. The distance between the peaks is the quadrupole splitting, Δ.

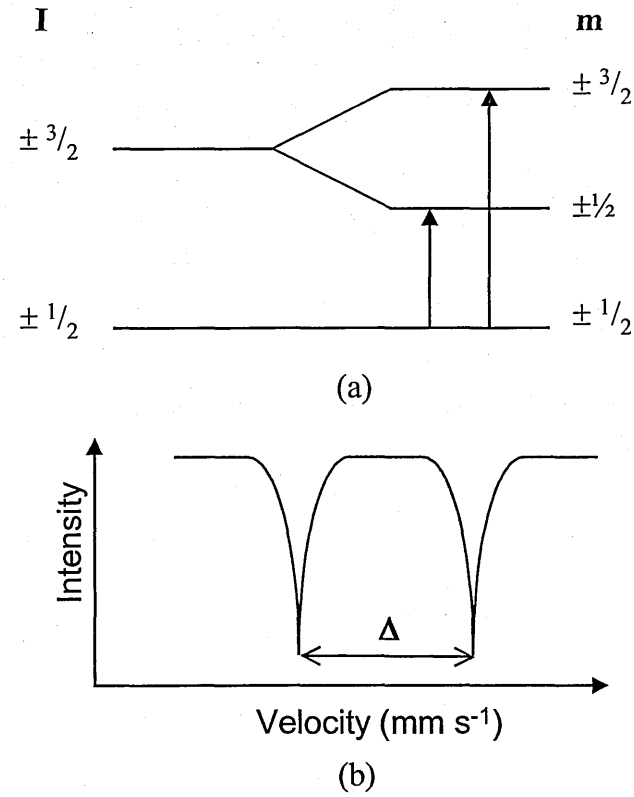

Figure 2.2.5 (a) Splitting of nuclear energy levels for ^{57}Fe nuclei in the presence of an electric field gradient and (b) resultant spectrum.

Several different components contribute to the electric field gradient. One is from the electronic environment about the nucleus, called the valence term. The valence term can be envisaged as arising from the valence electrons of the Mössbauer atom and originates from asymmetry in the electronic structure that derives from the unfilled or partially filled electron shells occupied by the valence electrons. The main contribution to the valence term is the asymmetric p- and d- electron populations, as the s-electron density is principally symmetric about the nuclear volume. A lattice contribution, arising from surrounding charged entities, also contributes to the electric field gradient. This arises from asymmetry in the arrangement of atoms around the

Mössbauer nuclei. Further contributions to the electric field gradient include the effects of molecular orbitals and any polarisation of the core electrons of the Mössbauer atom.

Hence, quadrupole splitting reflects the symmetry of the bonding environment and local structure in the vicinity of the Mössbauer atom. In high spin iron (III) compounds the iron nucleus is in a nearly symmetric d^5 configuration and consequently such compounds have a small quadrupole splitting. Contrastingly, high spin iron (II) compounds frequently show a large quadrupole splitting due to the asymmetric d^6 electronic environment.

Used in conjunction with chemical isomer shift data, the quadrupole splitting can be used to elucidate the oxidation states, electronic configurations and ligand arrays.

2.2.4 Magnetic Splitting

A nucleus of spin $I > 0$ has a magnetic moment that may interact with a magnetic field via a magnetic dipole interaction. Such a magnetic interaction induces splitting of the nuclear energy levels. Degeneracy of the nuclear states is removed by interaction of the nucleus with the magnetic field, and the levels subsequently split into $2I + 1$ sub-states. In ^{57}Fe the ground state with $I = ½$ splits into two sub-states, and the excited state with $I = {}^3/_2$ splits into four sub-states. For these spin states the selection rules $\Delta m = 0, \pm 1$, give rise to a symmetric six line Mössbauer spectrum. In such a spectrum the isomer shift is given as the centroid of the six peaks. The magnetic splitting of the ground and excited states for ^{57}Fe and resultant spectrum is illustrated in Figure 2.2.6.

The total magnetic field experienced by the nucleus is a vector sum of the magnetic hyperfine field and any external applied field. The magnetic hyperfine field arises from the spin of any unpaired electrons and is dependent upon oxidation- and spin-state of that atom. Hence, interpretation of the magnetically split Mössbauer spectrum can give information about electronic structure and magnetic properties in a system. It is also possible to modify the hyperfine field by application of an external factor, which distinguishes the hyperfine field from the other Mössbauer hyperfine interactions. Altering the applied field can change the appearance of the spectrum and aid interpretation. The occurrence of magnetically split ^{57}Fe Mössbauer spectra is common among ferro- and antiferro- magnetic materials. Paramagnetic materials cooled to below their Curie temperatures also exhibit a magnetically split Mössbauer spectrum.

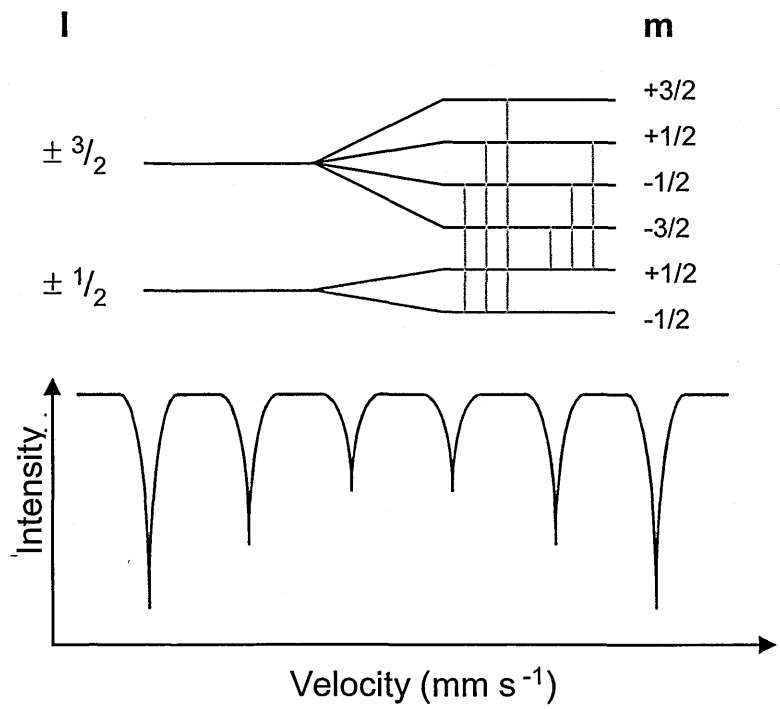

Figure 2.2.6 - (a) Splitting of nuclear energy levels by a magnetic field (b) and resultant spectrum.

2.3 Temperature programmed reduction (TPR)

2.3.1 Theory of TPR

Temperature programmed reduction (TPR)[68,69] is a thermal analysis technique used to probe the reducibility of solid compounds. Typically a dilute mixture of hydrogen is passed across a sample and the uptake of hydrogen is monitored as the temperature is raised linearly.

2.3.2 Instrumentation

The procedure involves passing a gas mixture through the reference arm of a katherometer detector before it is passed over the sample of interest. It is then passed through a drying tube and the measurement arm of the katherometer. Consumption of hydrogen and therefore sample reduction is detected as a voltage imbalance between the two arms of the katherometer.

The sample is mounted in a quartz tube and heated by a tube furnace at a fixed rate. The temperature is measured using a thermocouple. The temperature and katherometer signals are recorded using an analogue digital converter (ADC) coupled to a computer. A schematic diagram of the apparatus used in a TPR experiment is detailed in Figure 2.3.1.

The temperature programmed reduction data are displayed as a plot of hydrogen absorption as a function of temperature.

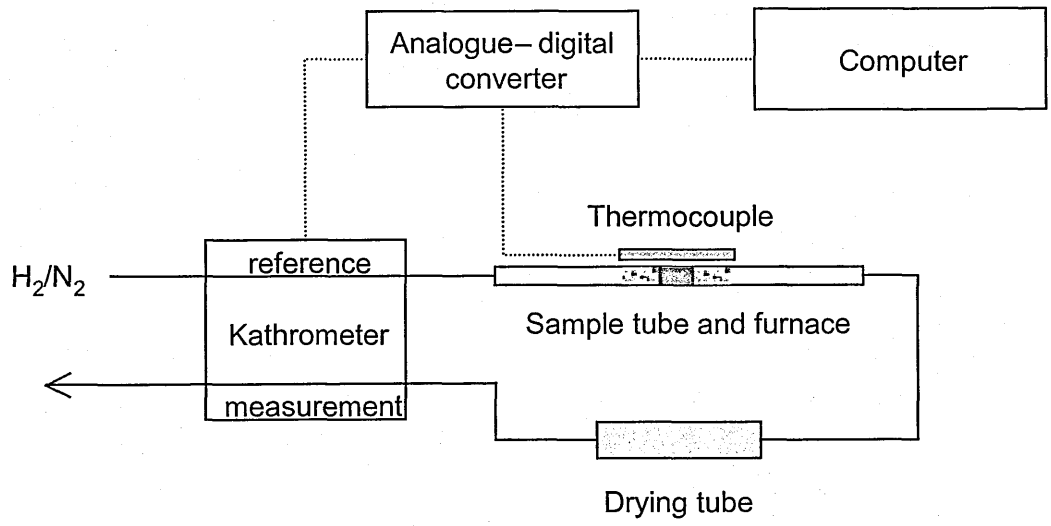

Figure 2.3.1 Schematic diagram showing the apparatus used for a TPR experiment.

Chapter 3

Experimental Methods and Instrumental Techniques

3.1 Experimental methods

3.1.1 Formation of cobalt aluminate, $CoAl_2O_4$ by calcination of cobalt- and aluminium -oxides, -hydroxides and -oxyhydroxides.

Stoichiometric mixtures of Co_3O_4 (Johnson Matthey M1275) and each of the aluminium-hydroxides -oxyhydroxides or -oxides listed in Table 3.1.1.1. were coarsely mixed and transferred into 500 ml zirconia milling vials. 150g of zirconia beads (1-2 mm diameter) and 100 ml of de-ionised water were added.

The vials were sealed and the contents milled using a Frisch Pulverisette 5 planetary mill with a constant wheel velocity of 100 rpm for periods of time relating to the result in Sections 4.2 and 4.3. The resultant slurry was vacuum filtered and dried in an oven at 80°C or under an infra red heat lamp.

The dried powders were lightly ground in a pestle and mortar, placed in unglazed alumina crucibles, and calcined in air using a programmable furnace with a typical ramp rate of 5 °C/min and then allowed to cool to ambient temperature.

Reagent	***Supplier***	***Crystalline phases*** *(see Chapter 4, Section 4.1)*
MO150	Alcan	Gibbsite (γ-$Al(OH)_3$)
SF11E	Alcan	Gibbsite (γ-$Al(OH)_3$)
AA101	Alcan	Mixture of Boehmite (γ-AlO(OH)) & Corundum (α-Al_2O_3)
Baco MA95	Alcan	Corundum (α-Al_2O_3)

Table 3.1.1.1 Summary of aluminium-oxide and- oxyhydroxide reagents used in milling reactions to form cobalt aluminate.

3.1.2 Formation of $CaMO_3$ (M=Ti/Sn)

A 30g equimolar mixture of CaO (Aldrich, 99.9%) and SnO_2 (Aldrich, 99.5%) was dry ball milled in a Frisch Pulverisette 5 planetary mill equipped with stainless steel 500 ml vials and ten 20 mm diameter stainless steel balls. The valves on the lid of each vial were left open, such that atmospheric oxygen was available throughout the milling process. The milling was performed at a constant wheel velocity of 200 rpm and samples removed at regular intervals. The same equimolar mixture of CaO and SnO_2 was also calcined at 1400 °C for 5 days to produce $CaSnO_3$ for comparison.

Similar procedures were used to mill CaO and the anatase (Aldrich 99.9%), and the rutile (formed by heating anatase at 1400°C for 2 days) modifications of TiO_2.

3.1.3 Formation of nano-structured zinc ferrite, $ZnFe_2O_4$

Polycrystalline zinc ferrite was synthesised by a solid state reaction from a mixture of α-Fe_2O_3 (Aldrich, 99.95%) and ZnO (Aldrich, 99.9%) with a Fe:Zn ratio of 2:1. The mixture was calcined in air at 1400 °C for 2 days.

A Frisch Pulverisette 5 planetary mill equipped with tungsten carbide-lined 500 ml vials and ten 20 mm diameter tungsten carbide balls was used to dry mill 30g of $ZnFe_2O_4$. The valves on the lid of each vial were left open such that atmospheric oxygen was available throughout the milling process. The milling was performed at a constant wheel velocity of 200 rpm and samples removed at regular intervals.

3.2 Characterisation methods

3.2.1 X-ray powder diffraction

X-ray powder diffraction patterns were recorded at 298K using a Siemens D5000 X-ray diffractometer with Ni-filtered Cu Kα (1.5406 Å) radiation. All patterns were identified using the Joint Committee on Powder Diffraction Standards (JCPDS) database.

3.2.2 In-situ X-ray powder diffraction

In-situ X-ray powder diffraction patterns were recorded at elevated temperatures at the Department of Chemistry, University of Cambridge. The diffraction patterns were recorded with Ni-filtered Cu Kα radiation (1.5406 Å) and a Phillips PW3710 goniometer. The sample was mounted on an electrically heated platinum bar enclosed within a water-cooled housing.

The samples were suspended in isopropan-2-ol that was applied to the platinum heating bar using a Pasteur pipette. The solvent was allowed to evaporate, forming a uniform coating on the surface of the heating element. The samples were heated to the required temperature and allowed to stabilise for 1-2 hours during the heating regime, and for 10 minutes during the cooling regime before each measurement was commenced.

3.2.3 Mössbauer spectroscopy

Mössbauer spectra were recorded at various temperatures with a microprocessor controlled constant acceleration spectrometer in transmission geometry. ^{57}Fe Mössbauer spectra were recorded using a 25 mCi ^{57}Co/Rh

source. ^{119}Sn Mössbauer spectra were recorded using a 5 mCi $Ca^{119}SnO_3$ source. The spectrometers were calibrated using a natural iron foil. All ^{57}Fe chemical isomer shift data are quoted relative to metallic iron and ^{119}Sn chemical isomer shifts are quoted relative to SnO_2. The effect of an external magnetic field upon the Mössbauer spectra was measured using a standard spectrometer in transmission geometry with a magnetic field of 0.7 Tesla applied perpendicular to the γ-ray beam. A closed-cycle helium cryostat and a nitrogen cryostat were used to record low temperature measurements. All the spectra were computer fitted to Lorentzian lines using the Mfit software.

3.2.4 Temperature programme reduction

Temperature programme reduction (TPR) profiles were recorded from 15-30 mg samples mounted in quartz tubing. A Carbolite tube furnace controlled by a Eurotherm 808 PID controller was used to heat the samples at a constant rate of 5 $^{\circ}Cmin^{-1}$. Gas flows (100 $mlmin^{-1}$) were controlled and detected, via a silica gel drying tube, using a modified Pye Unicam series 204 gas chromatograph with a katherometer detector. Temperature and katherometer analogue signals were digitised and recorded using a Pico Instruments analogue to digital converter linked to a computer.

3.2.5 Scanning electron microscopy

Scanning electron micrographs (SEM) were recorded from finely ground powder samples using a JEOL JSM-820 microscope with an accelerating voltage of 10 kV. The samples were coated with a thin layer of either gold or carbon, which was applied by plasma deposition.

Energy dispersive X-ray (EDX) microanalysis data were recorded from samples using a Kevex Sigma Gold analysis system with a Quantum detector.

3.2.6 Transmission electron microscopy

Transmission electron micrographs (TEM) were recorded from finely ground powder samples using either a JEOL 2000fx TEM/STEM or a Philips EM430 TEM microscope with a typical accelerating voltage of 200 kV. The samples were dispersed in isopropan-2-ol and applied to copper support grids with a carbon supporting film.

Energy dispersive X-ray (EDX) microanalysis data were recorded from samples using a Kevex Sigma Gold analysis system with a Quantum detector.

3.2.7 Differential scanning calorimetry and thermal gravimetric analysis

Differential scanning calorimetry (DSC) and thermal gravimetric analysis (TGA) were performed simultaneously using a Rheometric Scientific STA-1500 instrument. Samples of 5 to 10 mg weight were heated in dry air up to 1200 °C at a constant ramp rate of 5 °C/min and cooled at a constant ramp rate of 5 °C/min to ambient temperature.

Chapter 4

Formation of $CoAl_2O_4$

Results and Discussion

The work reported in this chapter concerns the synthesis of cobalt aluminate. Specifically the aims of the work have been to;

- Characterise the starting reagents and determine the effects of heat upon them.
- Investigate the effect of temperature on the formation of cobalt aluminate ($CoAl_2O_4$) from pre-milled mixtures of Co_3O_4 and different aluminium-containing starting materials.
- Investigate the effect of pre-bead milling of the reagents on the formation of cobalt aluminate.
- Determine the effect of the Co:Al ratio on the nature of spinel-related phases in the cobalt-aluminium-oxygen system.

4.1 Characterisation of starting materials

4.1.1 M1275

The X-ray powder diffraction pattern recorded from the fine black powder, M1275, is shown in Figure 4.1.1. The pattern coincided with that reported in the literature for Co_3O_4[41] which has a spinel-related structure. The absence of other reflections suggests that, within the limits of detection by X-ray powder diffraction, there were no crystalline impurities present such as the cobalt oxide containing only Co^{2+}, CoO, that forms when Co_3O_4 is heated[70] above *ca.* 600 °C.

Simultaneous differential scanning calorimetry (DSC) and thermal gravimetric analysis (TGA) data recorded from M1275 as the material was heated in air from 30 °C to 1200 °C and subsequently cooled at a constant rate of 5 °C/min

are shown in Figure 4.1.2. The results showed that, as the temperature was increased from *ca.* 890 °C to *ca.* 945 °C, there was a strong endotherm and the material lost *ca.* 6.8 % of total mass, closely matching the theoretical mass loss of oxygen, *ca.* 6.5%, that corresponds to the complete reduction of Co_3O_4 to CoO.

Between *ca.* 945 and 1200 °C there were no further features recorded by differential scanning calorimetry and thermal gravimetric analysis, suggesting that the material was stable in this temperature range. As the material was cooled from *ca.* 850 to *ca.* 770 °C, the mass of the material increased by *ca.* 3.9 % and there was a corresponding strong exotherm. The weight gained during cooling was less than that required for the complete conversion of CoO to Co_3O_4, but was consistent with conversion of *ca.* 57% of CoO to Co_3O_4.

The most likely reason for incomplete conversion to Co_3O_4 is that the particles of CoO form a surface crust of Co_3O_4, which hinders further diffusion of oxygen to the underlying CoO during the relatively short period that oxygen absorption was viable.

X-ray powder diffraction patterns recorded *in-situ* from M1275 at 30, 500, 900, 1000 and 1200 °C are shown in Figure 4.1.3. The material was heated at a rate of 5 °C/min and allowed to stabilise at each of the stated temperatures for 2 hours before the patterns were recorded. The X-ray powder diffraction patterns recorded at 1200, 1000, 800 and 30 °C during subsequent cooling of the material are shown in Figure 4.1.4. The crystalline phases identified from the X-ray powder diffraction patterns recorded at each of the stated temperatures are summarised in Table 4.1.1.1.

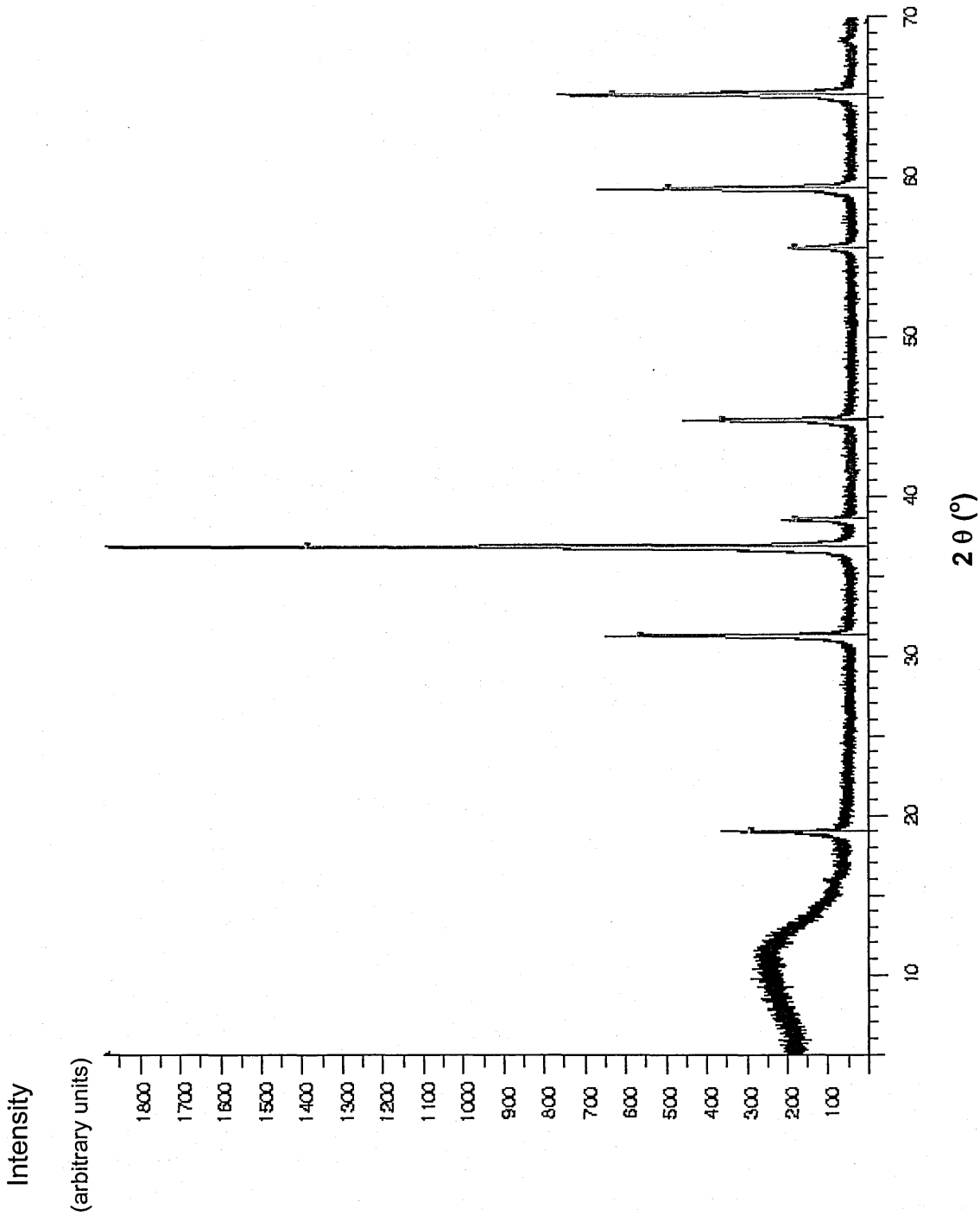

Figure 4.1.1. X-ray powder diffraction pattern recorded from M1275. Red bars beneath the pattern indicate the position of reflections reported in the literature as characteristic of Co_3O_4[41].

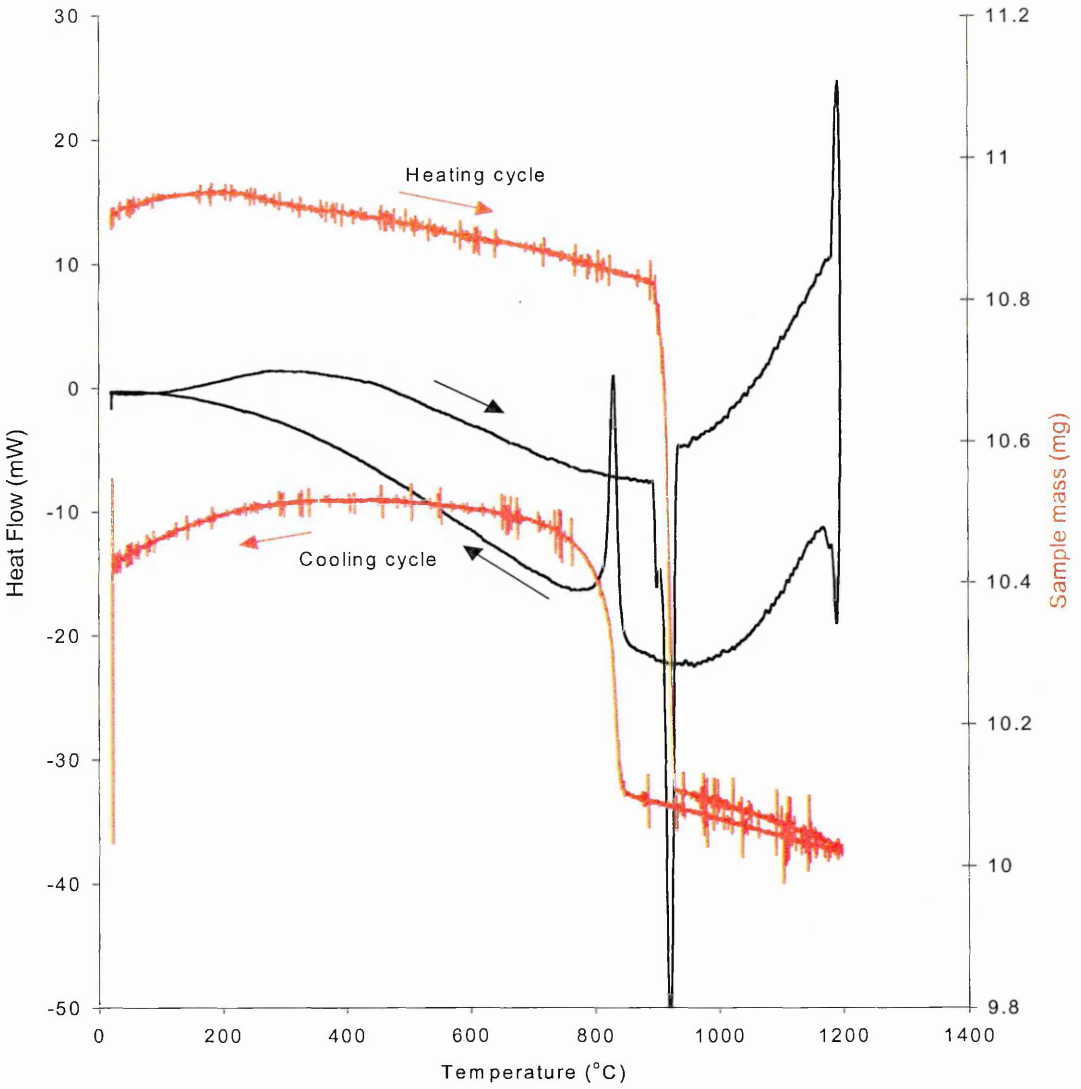

Figure 4.1.2 TGA (red) and DSC (black) data recorded from M1275 as the material was heated in air from 30 °C to 1200 °C and subsequently cooled to 30 °C.

	Temperature °C	Co_3O_4	CoO	Pt
Heating	30	√		√
	500	√		√
	900	√	√	√
	1000	√	√	√
	1200		√	√
Cooling	1000		√	√
	800	√		√
	30	√		√

Table 4.1.1.1. Summary of crystalline phases identified by X-ray powder diffraction patterns recorded in-situ as M1275 was heated from 30 °C to 1200 °C and subsequently cooled to 30 °C.

The X-ray powder diffraction patterns recorded *in-situ* during the heating regime (Figure 4.1.3, Table 4.1.1.1) at 30 °C and at 500 °C coincided with patterns characteristic of Co_3O_4 reported in the literature[41]. All the patterns contained additional reflections at 39.5°, 46° and 67.5° 2θ corresponding to the platinum[71] bar used to support and heat the sample.

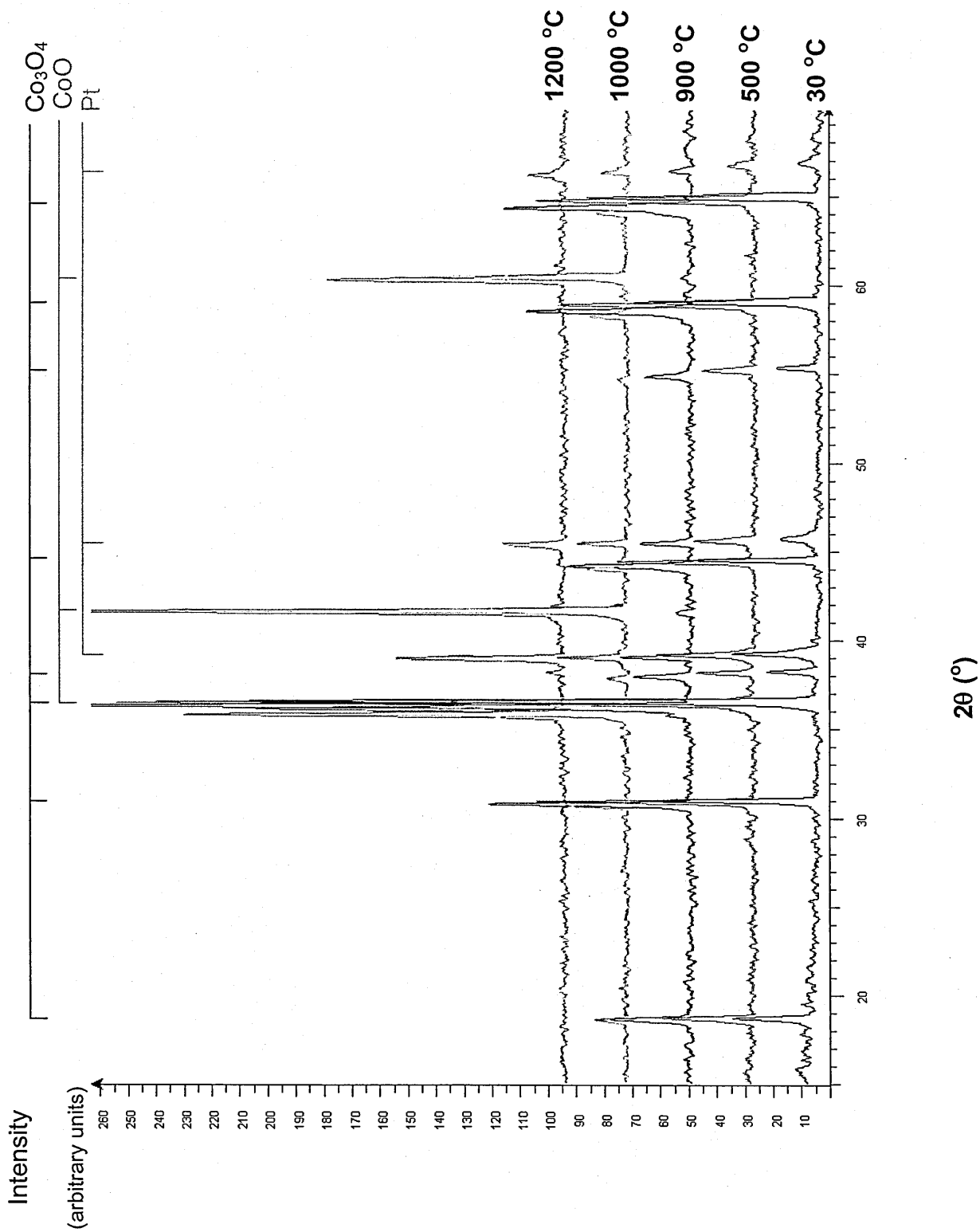

Figure 4.1.3. X-ray powder diffraction patterns recorded in-situ from M1275 as the material was heated from 30 °C to 1200 °C.

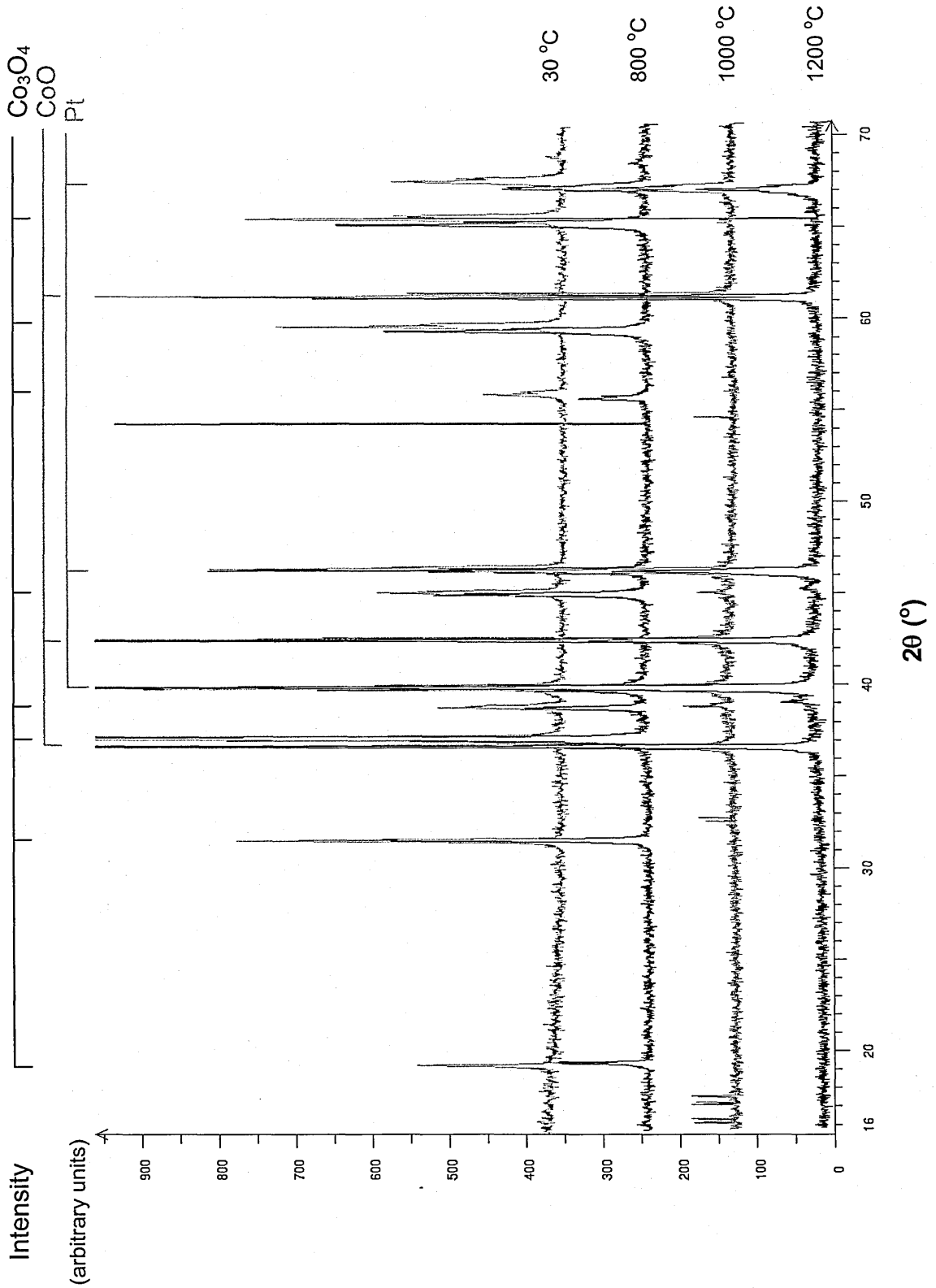

Figure 4.1.4. X-ray powder diffraction patterns recorded in-situ from M1275 as the material was cooled from 1200 °C to 30 °C.

The pattern recorded from the material heated at 900 °C showed reflections corresponding to Co_3O_4 and additional weak reflections at 42.5 and 62.5 °2θ that coincided with those reported in the literature[38] characteristic of CoO.

The X-ray powder diffraction pattern recorded at 1000 °C showed weak reflections from the spinel-related Co_3O_4 phase and a development of the pattern corresponding to CoO. Peaks characteristic of Co_3O_4 were not present in the pattern recorded at 1200 °C which showed only reflections corresponding to CoO. The results demonstrate the gradual conversion of Co_3O_4 to CoO between 500 and 900 °C and that the conversion is complete at 1200 °C.

The inconsistency between the temperature of conversion of Co_3O_4 to CoO as recorded by thermal gravimetric analysis and that recorded using X-ray powder diffraction may be associated with uneven heating when using the X-ray powder diffraction high temperature stage. This may have resulted in some Co_3O_4 being at a lower temperature and persisting even when the temperature of the stage exceeded the temperature where the bulk of the material was converted to CoO.

A general reversal of the effects due to heating were observed during subsequent cooling (Figure 4.1.4, Table 4.1.1.1). The pattern recorded after the material was cooled to 1000 °C was unchanged from that recorded at 1200 °C. The patterns recorded at 800 °C and 30 °C showed reflections corresponding to Co_3O_4 as the only crystalline phase. The complete conversion of CoO to Co_3O_4 during the cooling regime of the X-ray powder diffraction studies conflicted with the differential scanning calorimetry and thermal gravimetric analysis results where some CoO was present after

cooling to 30 °C. This may be associated with the slow rate of cooling during the X-ray powder diffraction studies and the thin layer of the sample on the X-ray diffractometer heating stage that allowed oxygen to permeate and react with CoO. It seems that this process was inhibited during the cooling cycle of the combined differential scanning calorimetry and thermal gravimetric analysis measurement because diffusion of oxygen is hindered during the relatively short period that oxygen absorption was viable.

In summary, the combined results from X-ray powder diffraction, but more accurately by differential scanning calorimetry and thermal gravimetric analysis, demonstrated that M1275 is composed of Co_3O_4 and is stable in air until *ca.* 890 °C, where it is slowly reduced to CoO. X-ray powder diffraction at 1200 °C shows that, within the limits of detection, CoO is the only crystalline phase formed when M1275 is heated in air.

Upon cooling the X-ray powder diffraction, and again more accurately by differential scanning calorimetry and thermal gravimetric analysis, results show that CoO is partially oxidised to form Co_3O_4 between *ca.* 850 and *ca.* 770 °C. These results conflict with data reported in the literature[72], which suggest that the transition between Co_3O_4 and CoO in air occurs above 600 °C but below 700 °C.

4.1.2 MO150

The X-ray powder diffraction pattern recorded from the fine white powder, MO150 (Figure 4.1.5), was characteristic of the aluminium oxyhydroxide of composition γ-$Al(OH)_3$, which is commonly known as gibbsite. The X-ray powder diffraction patterns recorded *in-situ* at 30, 200, 300, 400 and 850 °C in air are shown in Figure 4.1.6. The material was heated at a rate of 5 °C/min

and allowed to stabilise at each of the stated temperatures for 2 hours before the patterns were recorded. The crystalline phases identified from each X-ray powder diffraction pattern are summarised in Table 4.1.2.1.

Temperature °C	γ-Al(OH)$_3$	γ-AlO(OH)	Pt
30	√		√
200	√		√
300		√	√
400		√	√
850			√

Table 4.1.2.1. Summary of the crystalline phases identified by X-ray powder diffraction recorded in-situ as MO150 was heated between 30 °C and 850 °C.

Reflections from the platinum sample support were present throughout the experiment at *ca.* 39.5, 46 and 67.5 °2θ. Reflections from γ-Al(OH)$_3$, such as those at *ca.* 18° and 43.5 °2θ, persisted in the pattern recorded at 200 °C but at 300 °C and 400 °C the reflections characteristic of γ-Al(OH)$_3$ disappeared and were replaced by weaker reflections at *ca.* 28 and 38 °2θ, characteristic of γ-AlO(OH)[73] which is commonly known as boehmite. The pattern recorded from the material heated at 850 °C had broad reflections at *ca.* 37 °2θ that indicated the development of a semi-amorphous material, probably γ-Al_2O_3. Differential scanning calorimetry (DSC) and thermal gravimetric analysis (TGA) data recorded simultaneously as the material was heated from 30 °C to

1200 °C at a rate of 5 °C/min are shown in Figure 4.1.7. These results showed that the material was relatively stable until *ca.* 230 °C. Between *ca.* 230 °C and *ca.* 315 °C there was a strong endotherm with a corresponding mass loss of *ca.* 26 % of the original sample mass. Given the X-ray powder diffraction data, this was attributed to dehydroxylation of the material as it formed γ-AlO(OH). Further dehydroxylation was suggested by a gradual mass loss and an associated broad weak endotherm between *ca.* 420 °C and *ca.* 560 °C. Since X-ray powder diffraction failed to identify the formation of any new crystalline phases between these temperatures, the mass loss (*ca.* 0.15 % at 560 °C) was attributed to loss of intercalated water from γ-AlO(OH) without major changes to the structure as is reported[42] to occur when pseudoboehmite, which is boehmite containing intercalated water, is converted to boehmite.

The total mass lost, *ca.* 35%, after the material was heated to 1200 °C coincided with the calculated mass loss *(ca.* 34.6 %) for the conversion of $Al(OH)_3$ to Al_2O_3.

The X-ray powder diffraction pattern recorded from MO150, after heating in air at 1200 °C is shown in Figure 4.1.8. This showed complete transformation to α-Al_2O_3 as expected[74].

In summary the results showed that MO150, initially γ-$Al(OH)_3$, dehydrates to form γ-AlO(OH), possibly in the form of pseudoboehmite between *ca.* 200 °C and *ca.* 300 °C. At temperatures between 400 °C and 850 °C, γ-AlO(OH) forms amorphous intermediates, before eventually forming α-Al_2O_3 when heated at 1200 °C.

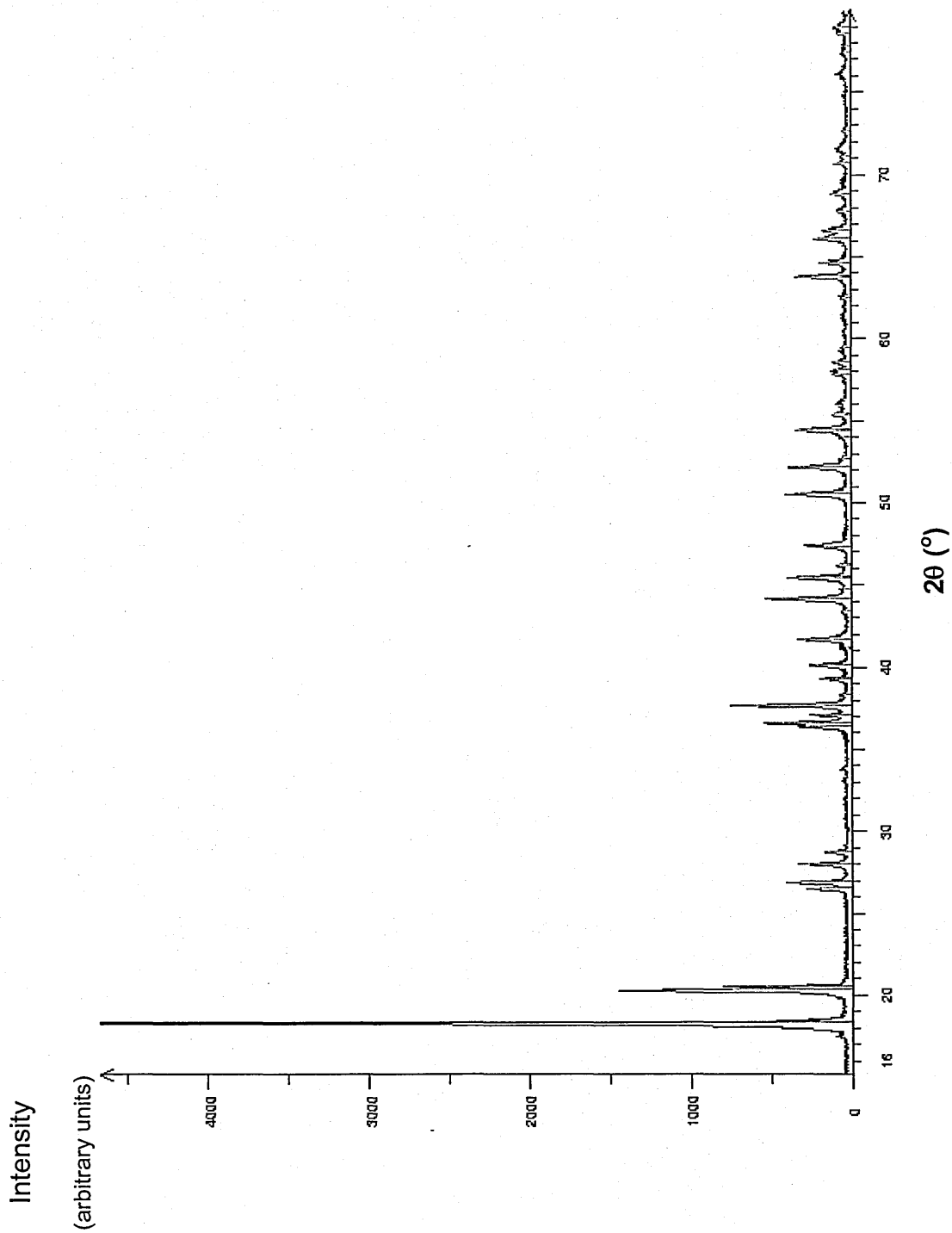

Figure 4.1.5. X-ray powder diffraction pattern recorded from MO150. Red bars beneath the pattern indicate the position of reflections reported in the literature as characteristic of γ-Al(OH)$_3$[76].

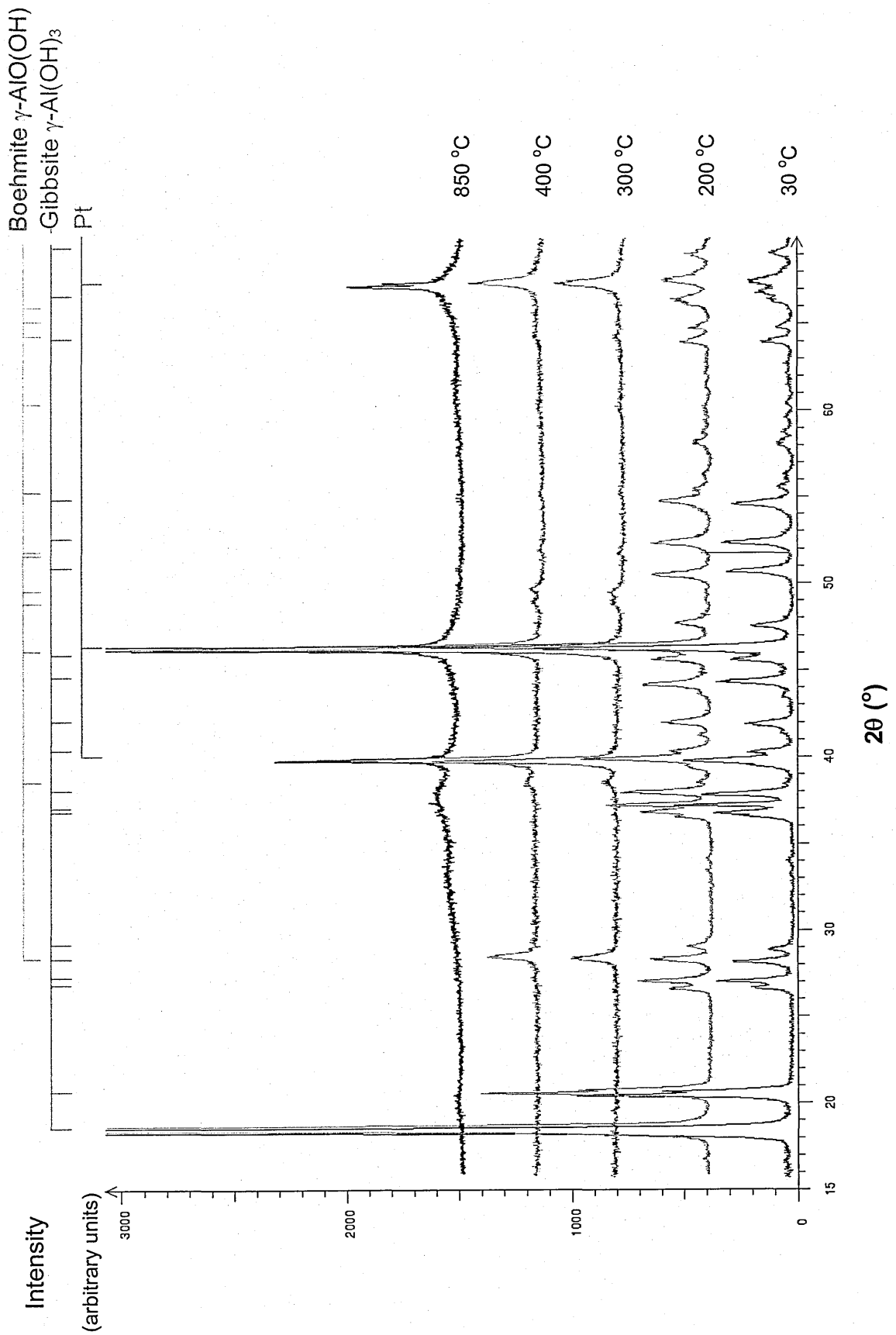

Figure 4.1.6. ***X-ray powder diffraction patterns recorded in-situ from MO150 as the material was heated from 30 °C to 850 °C in air.***

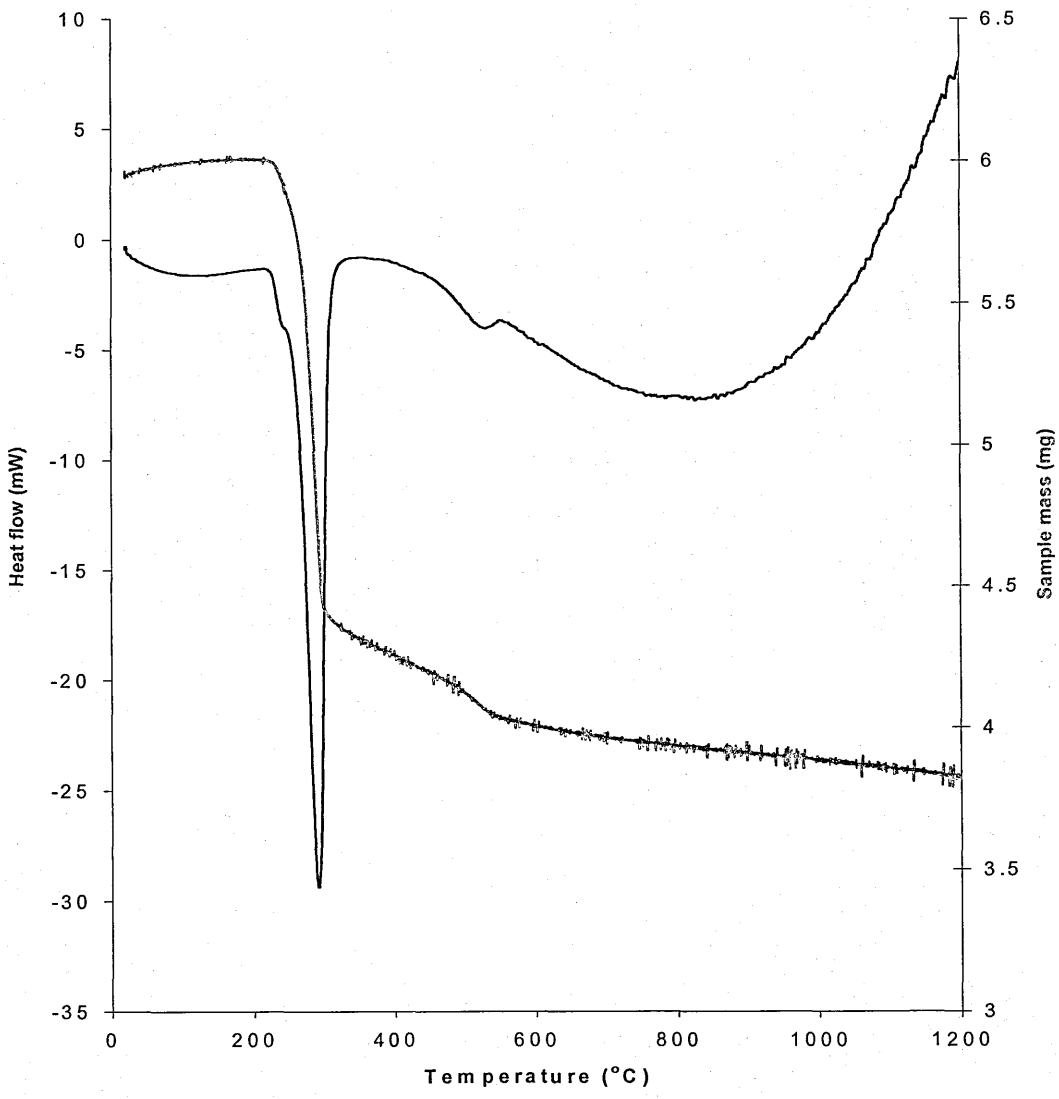

Figure 4.1.7 *TGA (red) and DSC (black) data recorded from MO150 as the material was heated between 30 °C and 1200 °C in air.*

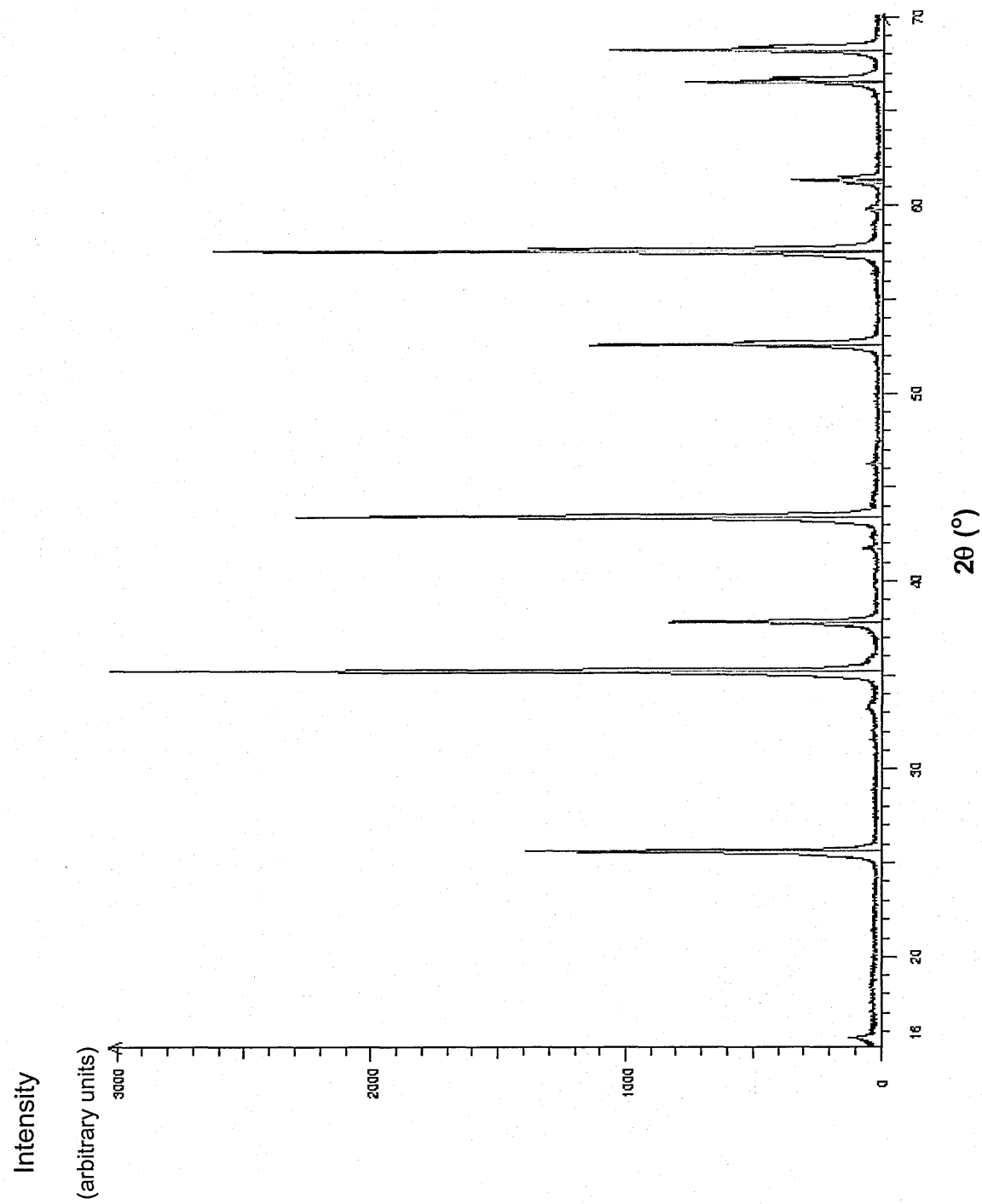

Figure 4.1.8 X-ray powder diffraction pattern recorded from MO150 after the material was heated in air at 1200 °C. Red bars beneath the pattern indicate the position of reflections reported in the literature for α-Al_2O_3[75]

4.1.3 SF11E

The X-ray powder diffraction pattern recorded from the fine white powder SF11E is shown in Figure 4.1.9. The pattern coincides with that reported in the literature for γ-$Al(OH)_3$[76]. The reflections are broader than those in the X-ray powder diffraction pattern recorded from MO150 (Figure 4.1.5) which was also shown to be γ-$Al(OH)_3$. Given the fine nature of the powder the results suggest that SF11E is of a smaller crystallite size.

Differential scanning calorimetry (DSC) and thermal gravimetric analysis (TGA) data, recorded simultaneously as the material was heated from 30 °C to 1200 °C at a rate of 5 °C/min in air are shown in Figure 4.1.10. The data are similar to those recorded from γ-$Al(OH)_3$ in the sample of MO15O (Figure 4.1.7). Between *ca.* 230 °C and 300 °C there was a strong endotherm and the material lost *ca.* 29 % of the original sample mass corresponding to dehydroxylation of γ-$Al(OH)_3$ to γ-AlO(OH) as previously discussed in Section 4.1.2. No evidence for the loss of intercalated water from γ-AlO(OH) was observed in the thermal gravimetric analysis data recorded from SF11E.

The X-ray powder diffraction pattern recorded from SF11E after the material was heated at 1200 °C in air is shown in Figure 4.1.11. The pattern coincides with that reported in the literature for α-Al_2O_3[75] and showed that within the limits of detection of X-ray powder diffraction, α-Al_2O_3 was the only crystalline phase present at 1200 °C.

In summary the results show that SF11E, initially γ-$Al(OH)_3$ of finer particle size than MO150, undergoes similar dehydration and phase transitions to those observed for MO150, and at 1200 °C forms α-Al_2O_3.

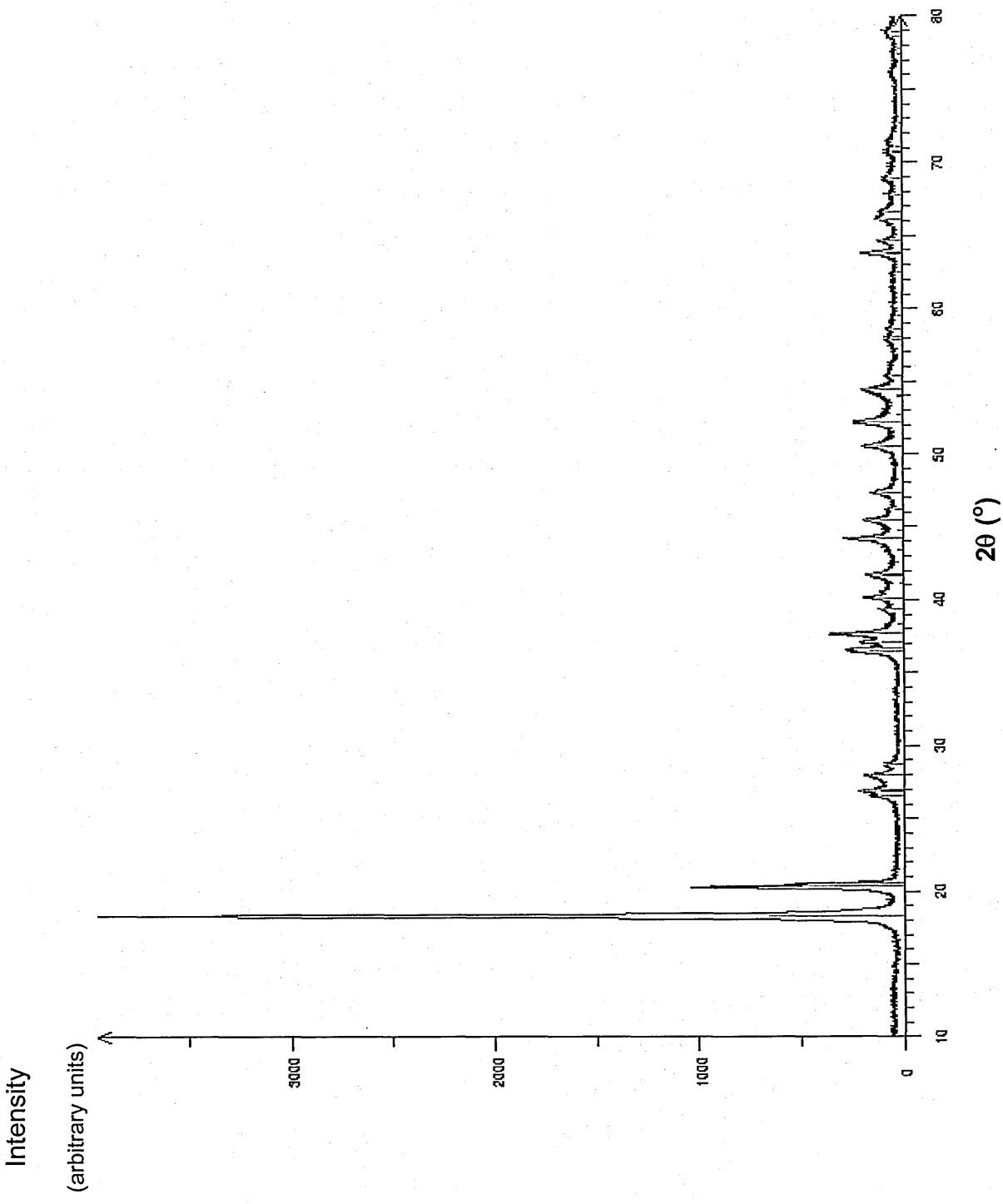

Figure 4.1.9. X-ray powder diffraction pattern recorded from SF11E. Red bars beneath the pattern indicate the position of reflections reported in the literature for γ-$Al(OH)_3$[76].

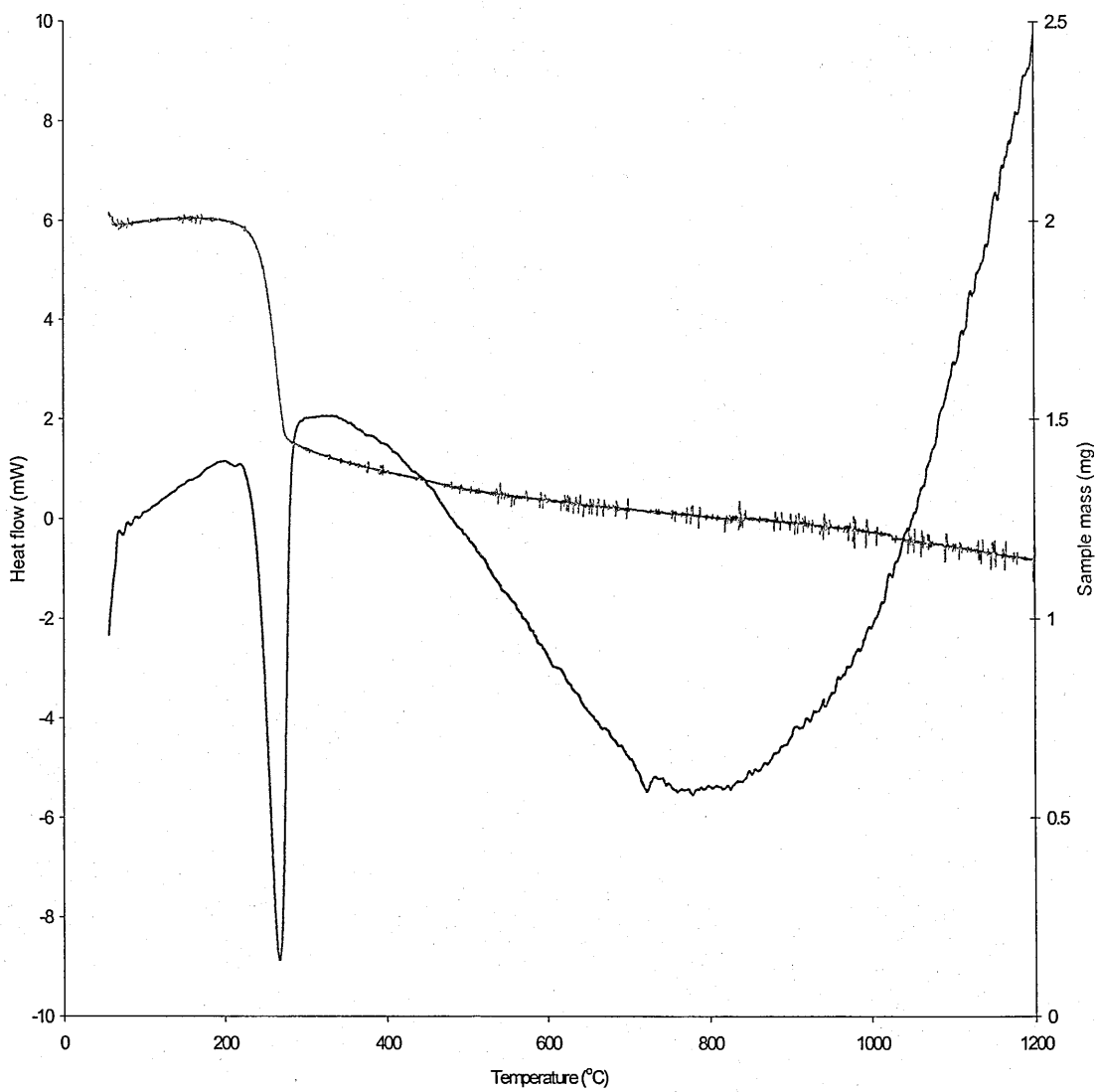

Figure 4.1.10 TGA (red) and DSC (blue) data recorded from SF11E as the material was heated between 30 °C and 1200 °C in air.

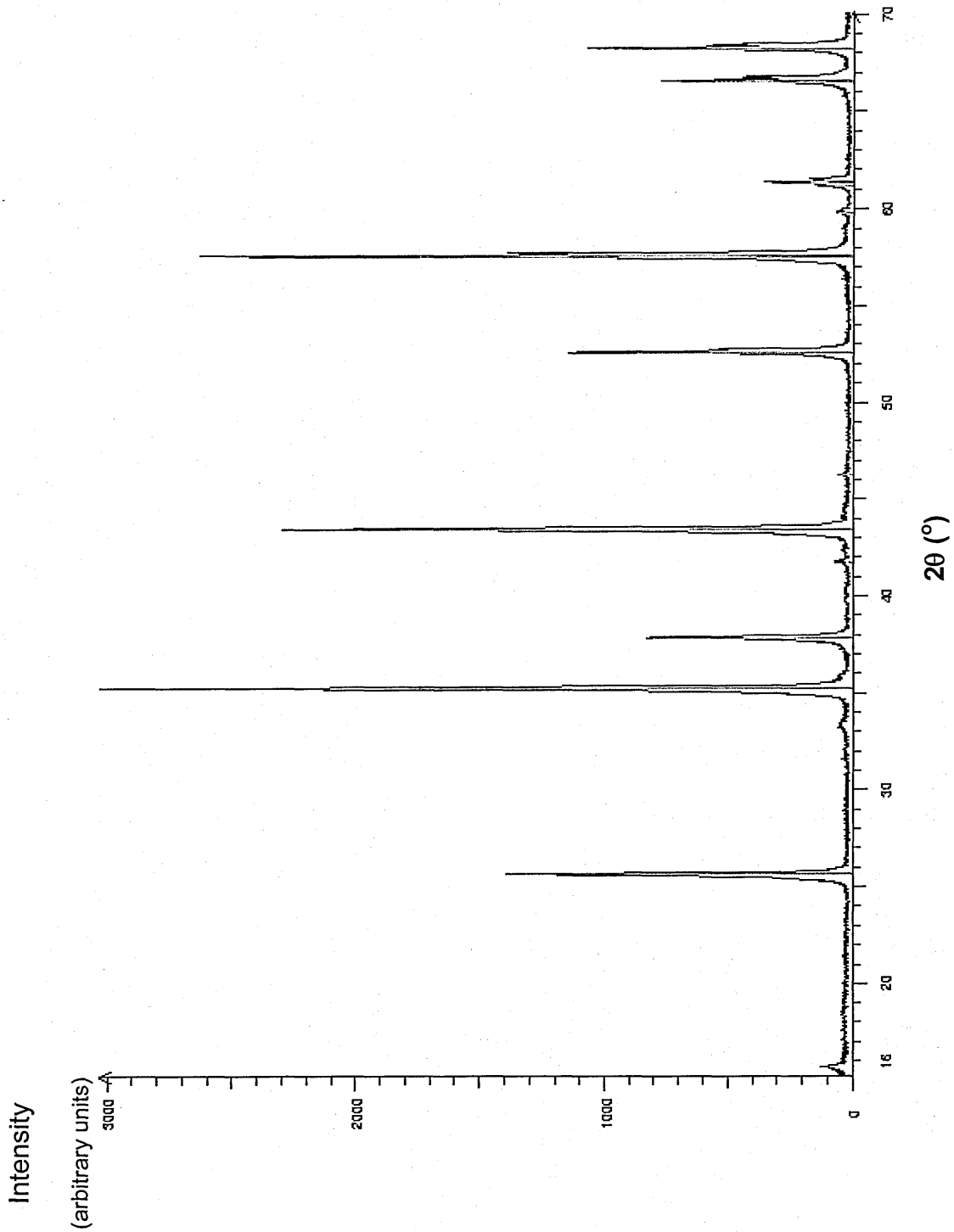

Figure 4.1.11 X-ray powder diffraction pattern recorded from SF11E after the material had been heated in air at 1200 °C. Red bars beneath the pattern indicate the position of reflections reported in the literature for α-Al_2O_3[75]

4.1.4 AA101

The X-ray powder diffraction pattern recorded from AA101, a fine white powder, is shown in Figure 4.1.12. The broad lined pattern suggests that the material was poorly crystalline or of small particle size. However, by reference to patterns reported in the literature it was possible to identify the presence of γ-AlO(OH)[73] and α-Al_2O_3[75] in AA101.

The X-ray powder diffraction pattern recorded from AA101 after heating to 1200 °C for 6 hours is shown in Figure 4.1.13. The pattern coincides with that reported in the literature for α-Al_2O_3[75] and showed that, within the limits of detection by X-ray powder diffraction, α-Al_2O_3 is the only crystalline phase present at 1200 °C.

Differential scanning calorimetry (DSC) and thermal gravimetric analysis (TGA) data, recorded simultaneously as the material was heated from 30 °C to 1200 °C at a rate of 5 °C/min, are shown in Figure 4.1.14. These results showed a broad weak endotherm with a steady and modest mass loss between ca. 50 °C and *ca.* 250 °C. The heat flow decreased as the material approached *ca.* 325 °C where the rate of mass loss also began to decrease. The mass lost after the material was heated to 1200 °C totalled *ca.* 18% of the original sample mass. The mass loss expected if the initial material had consisted of desiccated γ-AlO(OH) and was completely transformed to α-Al_2O_3 would have been *ca.* 15 wt%. Hence, in summary, AA101 appears to be a mixture of γ-AlO(OH) and α-Al_2O_3, which is converted to α-Al_2O_3 at 1200 °C.

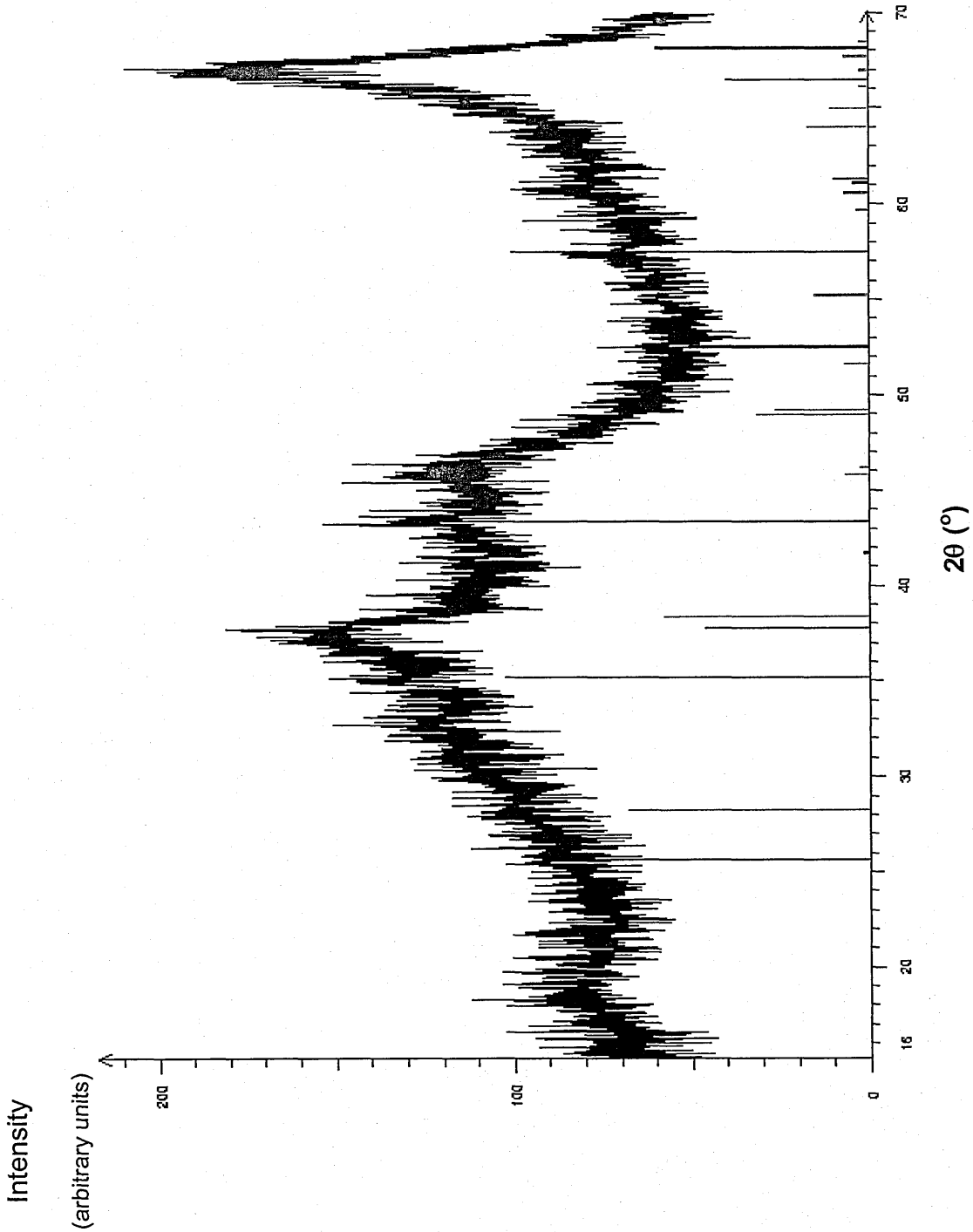

Figure 4.1.12. X-ray powder diffraction pattern recorded from AA101. Red bars beneath the pattern, indicate the position of reflections reported in the literature for γ-AlO(OH)[73] and blue bars indicate the position of reflections reported in the literature for α-Al_2O_3[75].

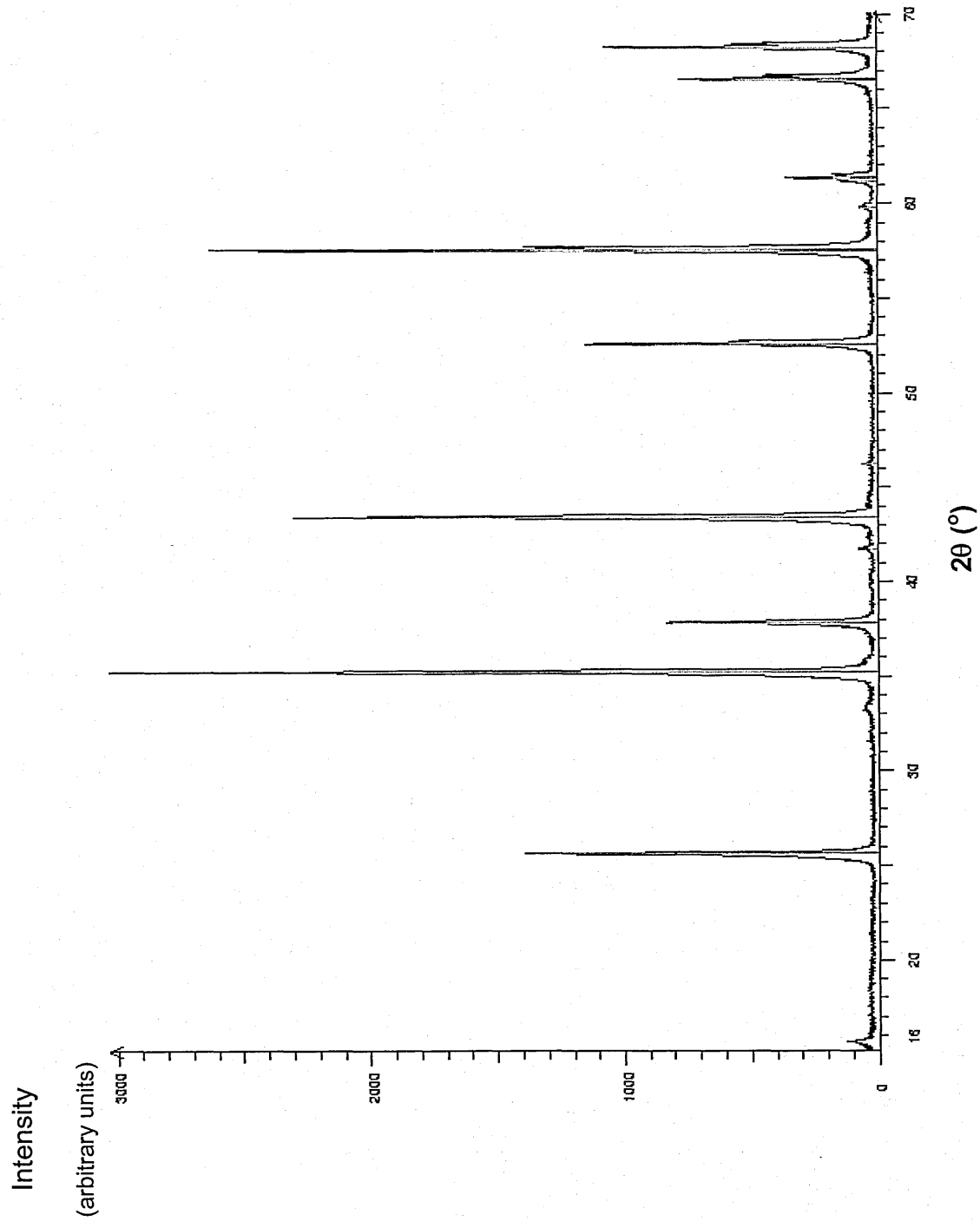

Figure 4.1.13 X-ray powder diffraction pattern recorded from AA101 after the material had been heated in air at 1200 °C. Red bars beneath the pattern indicate the position of reflections reported in the literature for α-Al_2O_3[75]

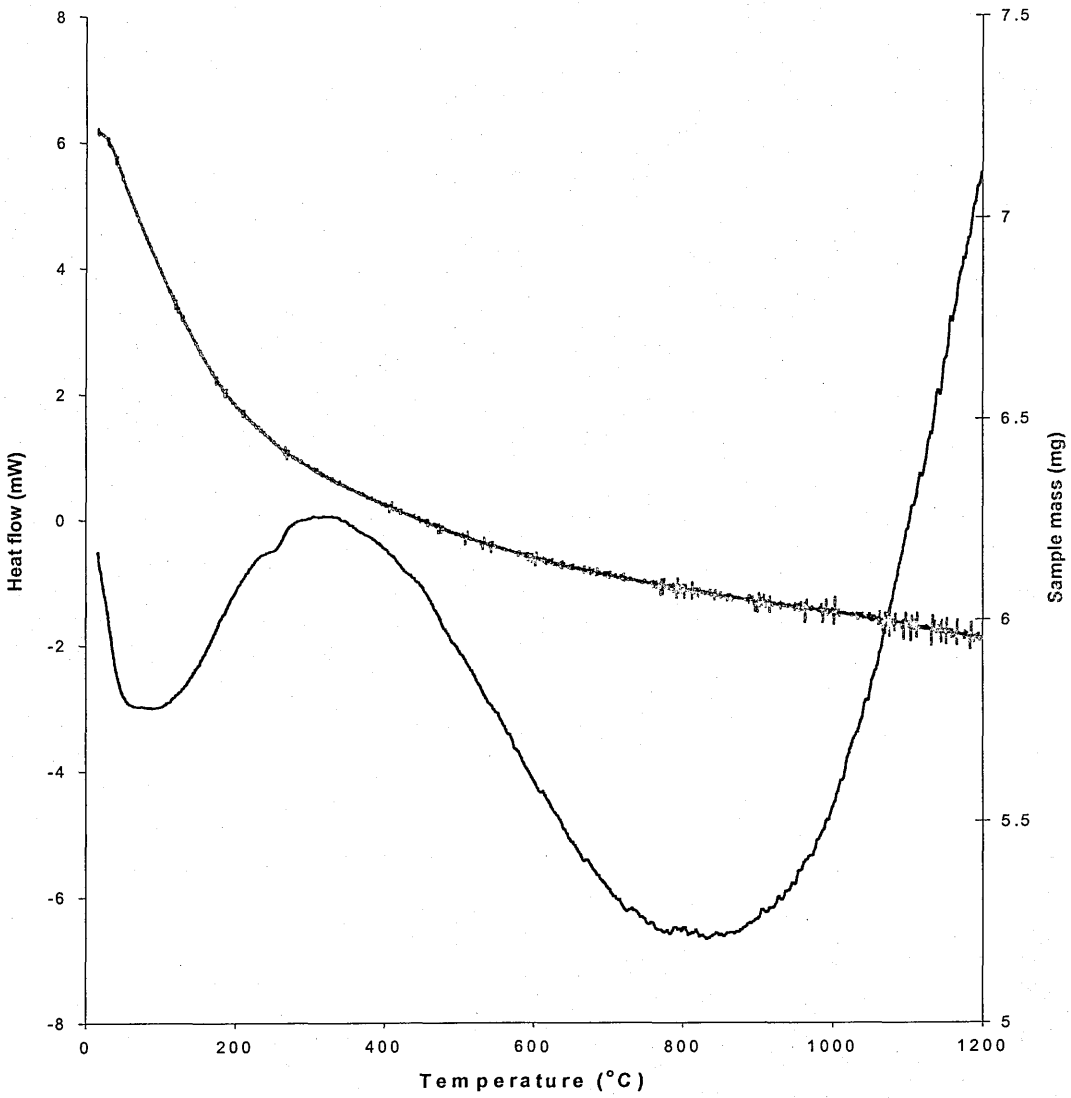

Figure 4.1.14 TGA (red) and DSC (black) data recorded from AA101 as the material was heated from 30 °C to 1200 °C in air.

4.1.5 Baco MA95

The X-ray powder diffraction pattern recorded from the fine white powder Baco MA95 is shown in Figure 4.1.15. and has reflections that match those reported in the literature for α-Al_2O_3[75]. Within the limits of detection of X-ray powder diffraction, no other crystalline phases were observed.

Differential scanning calorimetry (DSC) and thermal gravimetric analysis (TGA) data, recorded simultaneously as the material was heated from 30 °C to 1200 °C at a rate of 5 °C/min, are shown in Figure 4.1.16. The thermal gravimetric analysis showed that only *ca.* 1 % of the original mass was lost during the thermal analysis process, primarily between 200 °C and 230 °C and presumably reflects the loss of absorbed water. There were no significant features displayed by differential scanning calorimetry and the material appeared to be stable throughout the heating regime. These results are consistent with Baco MA95 being composed of α-Al_2O_3.

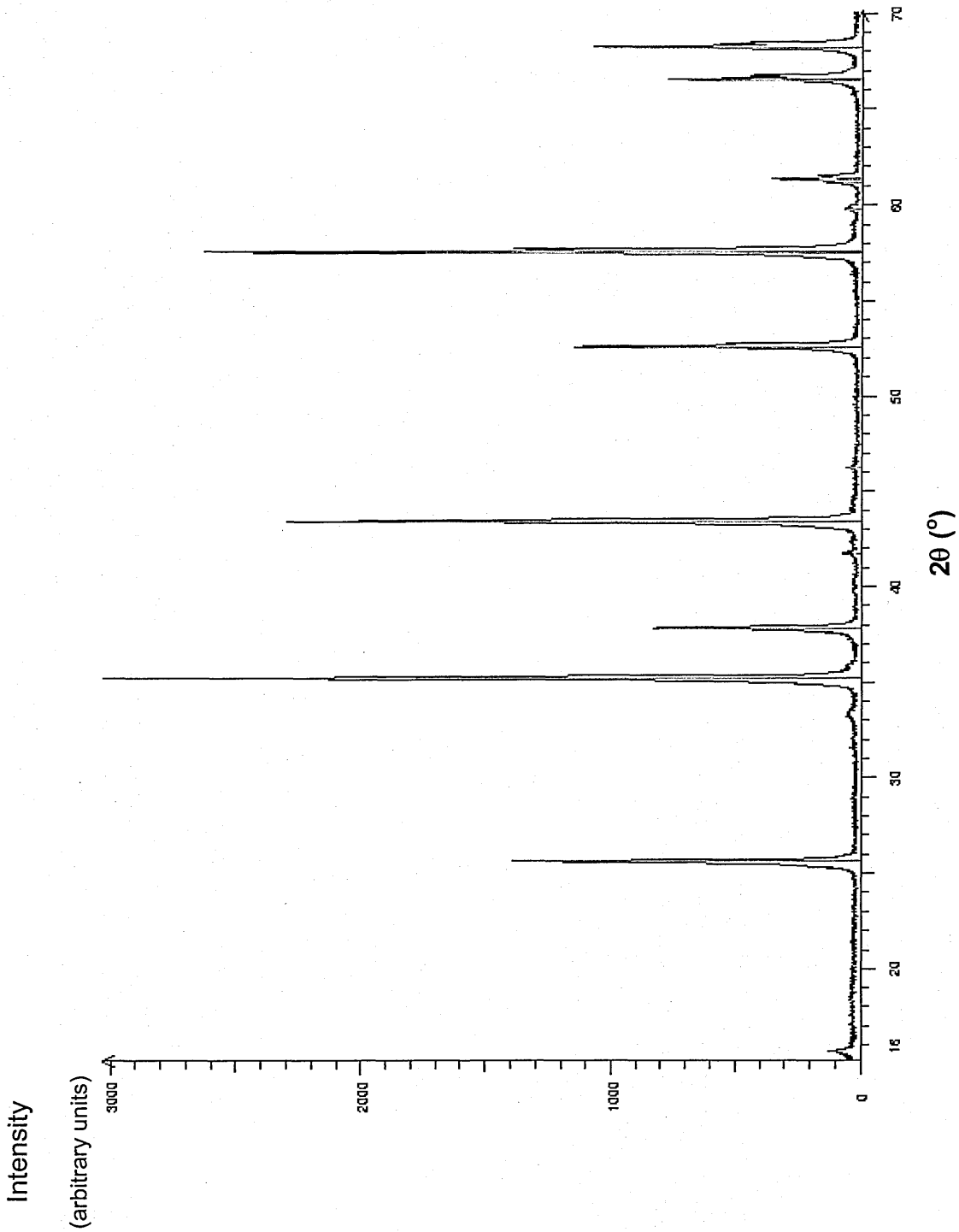

Figure 4.1.15. X-ray powder diffraction pattern recorded from Baco MA95. Red bars beneath the pattern indicate the position of reflections reported in the literature for α-Al_2O_3[75].

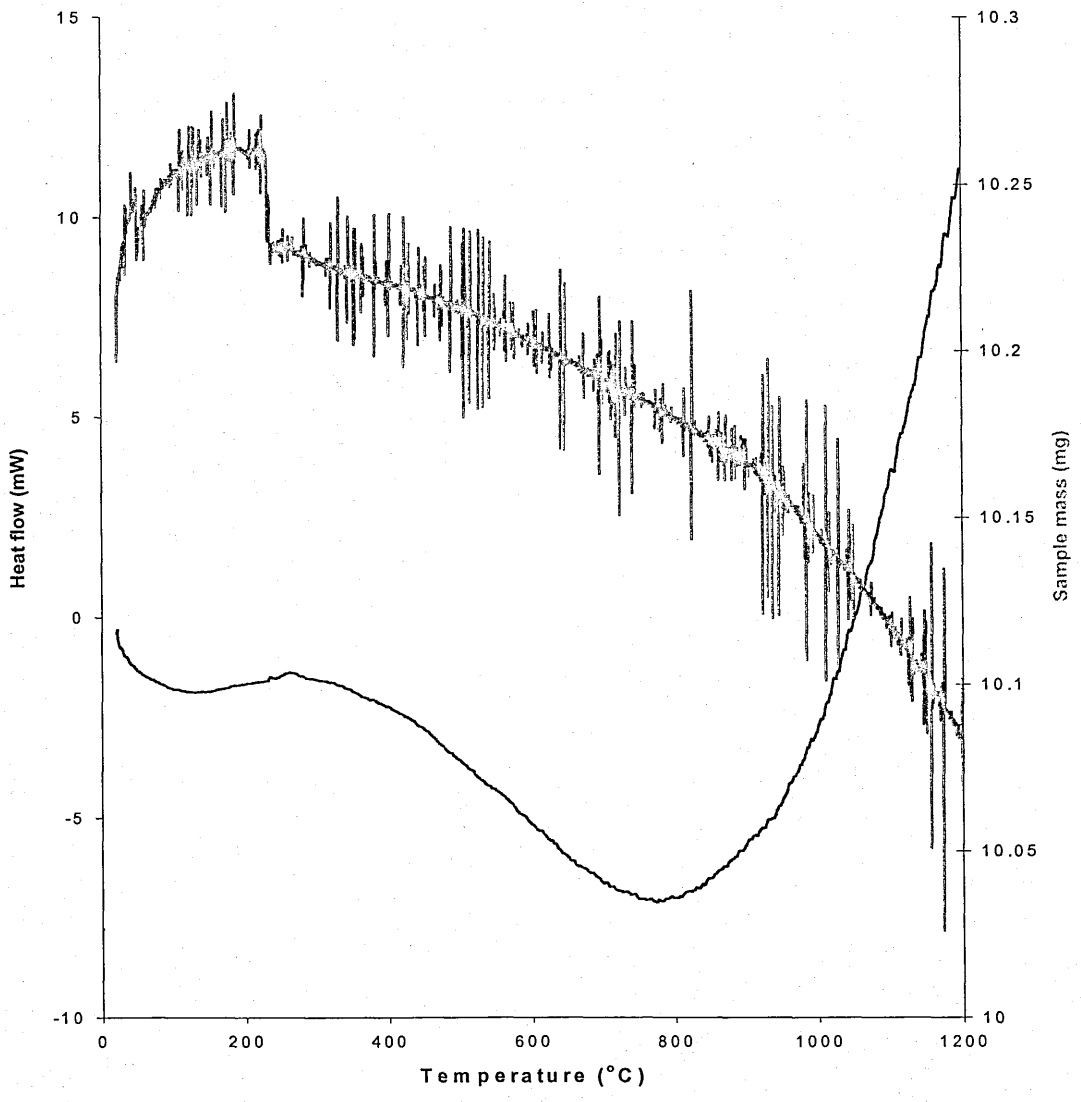

Figure 4.1.16 ***TGA(red) and DSC (black) data recorded from Baco MA95 as the material was heated from 30 °C to 1200 °C in air.***

In summary, the work reported in Section 4.1 showed that;

- M1275 is Co_3O_4.
- M1275 reduces to form CoO above *ca.* 890 °C in air.
- M1275 oxidises to form Co_3O_4 between *ca.* 850 and *ca.* 770 °C during cooling in air.
- CoO requires a ready supply of oxygen to permeate throughout the material in order for oxidation to occur during cooling.
- CoO is stable in air below *ca.* 770°C.

- MO150 is gibbsite (γ-$Al(OH)_3$).
- MO150 forms boehmite (γ-AlO(OH)) between *ca.* 200 and *ca.* 300 °C.
- MO150 forms amorphous phases between *ca.* 400 and *ca.* 800 °C.
- MO150 forms corundum (α-Al_2O_3) when heated at *ca.* 1200 °C and is stable upon cooling.

- SF11E is gibbsite (γ-$Al(OH)_3$).
- SF11E has a smaller crystallite size than MO150.
- SF11E forms boehmite (γ-AlO(OH)) between *ca.* 200 and *ca.* 300 °C.
- SF11E forms amorphous phases between *ca.* 400 and *ca.* 800 °C.
- SF11E forms corundum (α-Al_2O_3) when heated at *ca.* 1200 °C and is stable upon cooling.

- AA101 is poorly crystalline.
- AA101 is a mixture of boehmite (γ-AlO(OH)) and corundum (α-Al_2O_3).
- AA101 forms corundum (α-Al_2O_3) when heated at *ca.* 1200 °C and is stable upon cooling.

- Baco MA95 is crystalline corundum (α-Al_2O_3).
- Baco MA95 is thermally stable.

4.2 The formation of cobalt aluminate ($CoAl_2O_4$) by calcination

4.2.1 Mixture of M1275 (Co_3O_4) and MO150 (γ-$Al(OH)_3$)

The X-ray powder diffraction patterns recorded from a 1 mol : 6 mol mixture of M1275 and MO150 after the mixture has been pre-milled as described in Section 3.1.1 and heated to temperatures between 30 °C and 1400 °C for 1 hour and then rapidly cooled, are shown in Figure 4.2.1. The crystalline phases identified from each X-ray powder diffraction pattern are summarised in Table 4.2.1.1.

Temperature °C	γ-$Al(OH)_3$	α-Al_2O_3	Co_3O_4	CoO	$CoAl_2O_4$
30	√		√		
500	√		√		
700	√		√		
800			√		
900			√	√	
1000			√	√	√
1100		√	√	√	√
1200		√			√
1300		√			√
1400					√
1400 (held for 48 hours)					√

Table 4.2.1.1 Summary of crystalline phases identified by X-ray powder diffraction from a mixture of M1275 (Co_3O_4) and MO150 (γ-$Al(OH)_3$) heated between 30 °C and 1400 °C for 1 hour and in the final case, at 1400 °C for 48 hours.

As the material was heated at temperatures below 1000 °C, the reagents appear to form the same phases as those observed when the reagents were heated independently (see Sections 4.1.1 and 4.1.2). The X-ray powder diffraction pattern recorded from the unheated material showed reflections at *ca.* 18 °2θ, that coincided with those reported in the literature as being characteristic of γ-$Al(OH)_3$,[76] and, at *ca.* 38.5 °2θ, characteristic of Co_3O_4. These reflections persisted when the material was heated to 500 °C and 700 °C. Upon further heating between 800 °C and 1000 °C, the reflections from γ-$Al(OH)_3$ disappeared, presumably as amorphous aluminium oxide phases formed.

The unheated material also showed reflections at *ca.* 38.5 °2θ characteristic of Co_3O_4. These reflections persisted after heating at temperatures up to 1000 °C. At 900 °C peaks at 42.5 °2θ, typical of CoO were observed.

At 1000 °C and above, the cobalt-containing species and the aluminium-containing species begin to interact as demonstrated in the patterns recorded at 1000 °C where a peak *ca.* 49 °2θ was observed, characteristic of $CoAl_2O_4$[77]. The intensity of this peak increased as the temperature was raised.

A proportion of the cobalt oxide persisted as CoO until 1100 °C and similarly a proportion of the aluminium oxide formed corundum, which persisted to 1300 °C.

The corundum-related peaks reached a maximum intensity at 1200 °C and then reduced in intensity as the temperature increased and the α-Al_2O_3 was consumed in the reaction to form $CoAl_2O_4$. This observation demonstrates the reaction between corundum and cobalt oxides to form $CoAl_2O_4$ between 1200 and 1300 °C. However a possible alternative mechanism would involve the

availability of cobalt oxide during the rearrangement of the oxygen lattice of aluminium oxide from a cubic-close packed gamma phase, to a hexagonal-close packed alpha phase. It seems feasible that, if cobalt oxides are available as this rearrangement occurs, then there may be a lower energy mechanism by which a proportion of the cobalt- and aluminium-oxides may inter-diffuse thus forming the mixed metal spinel that manifests itself as $CoAl_2O_4$ at 1000 °C. Should the temperature range where this inter-diffusion of cobalt and aluminium oxides occur be relatively small, and the rate at which it occurs be sufficiently slow, then it is possible that only a small proportion of the aluminium oxide can react in this manner and that the remainder forms α-Al_2O_3 which then subsequently reacts directly with CoO. If this mechanism does occur, then it seems clear that very intimately mixed cobalt- and aluminium-oxides would react much more readily at lower temperature than those less intimately mixed. Presumably, pre-milling would be advantageous to achieving this intimate mixing.

The observation of reflections at *ca.* 49 °2θ matching those reported in the literature characteristic of $CoAl_2O_4$[77] were apparent in the X-ray powder diffraction pattern recorded from the material heated at 1000 °C and the enhanced intensity of the $CoAl_2O_4$ reflections as the material was heated further are consistent with this proposed mechanism.

The X-ray powder diffraction pattern recorded from a mixture of M1275 and MO150 heated at 1400 °C for 48 hours, which is shown in Figure 4.2.2, showed only reflections that coincided with those reported in the literature for $CoAl_2O_4$.[77]

These results were endorsed by the X-ray powder diffraction patterns recorded *in-situ* from a mixture of M1275 and MO150 as the mixture was heated in air between 30 °C and 1200 °C which are shown in Figure 4.2.3. The material was heated at a rate of 5 °C/min and allowed to stabilise at each of the stated temperatures for 2 hours before the patterns were recorded. The patterns recorded during subsequent cooling of the material are shown in Figure 4.2.4. The crystalline phases identified from each of the X-ray powder diffraction patterns are summarised in Figure 4.1.2.

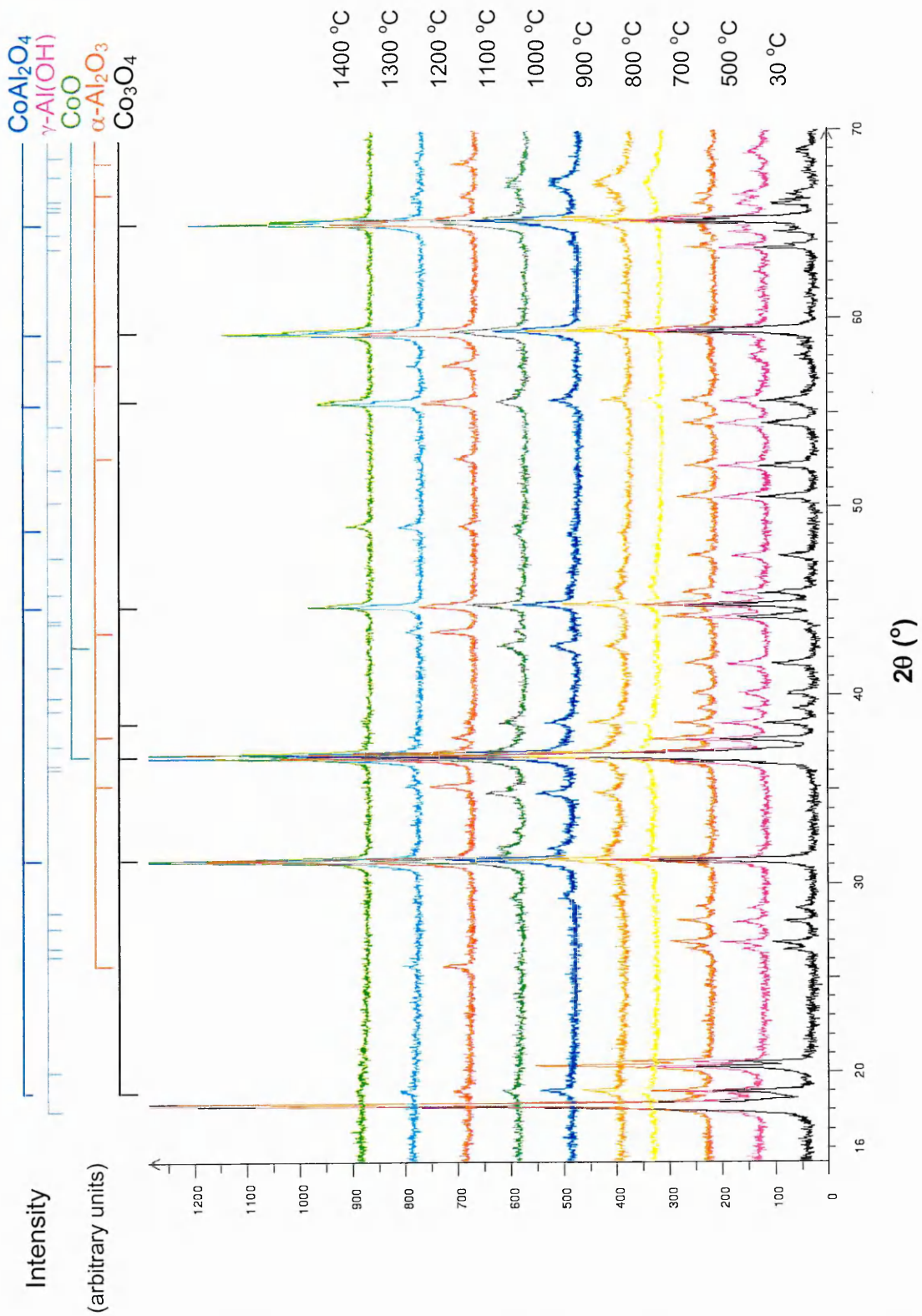

Figure 4.2.1 X-ray powder diffraction patterns recorded from a mixture of M1275 (Co_3O_4) and MO150 (γ-$Al(OH)_3$) after the material was heated to temperatures up to 1400 °C for 1 hour.

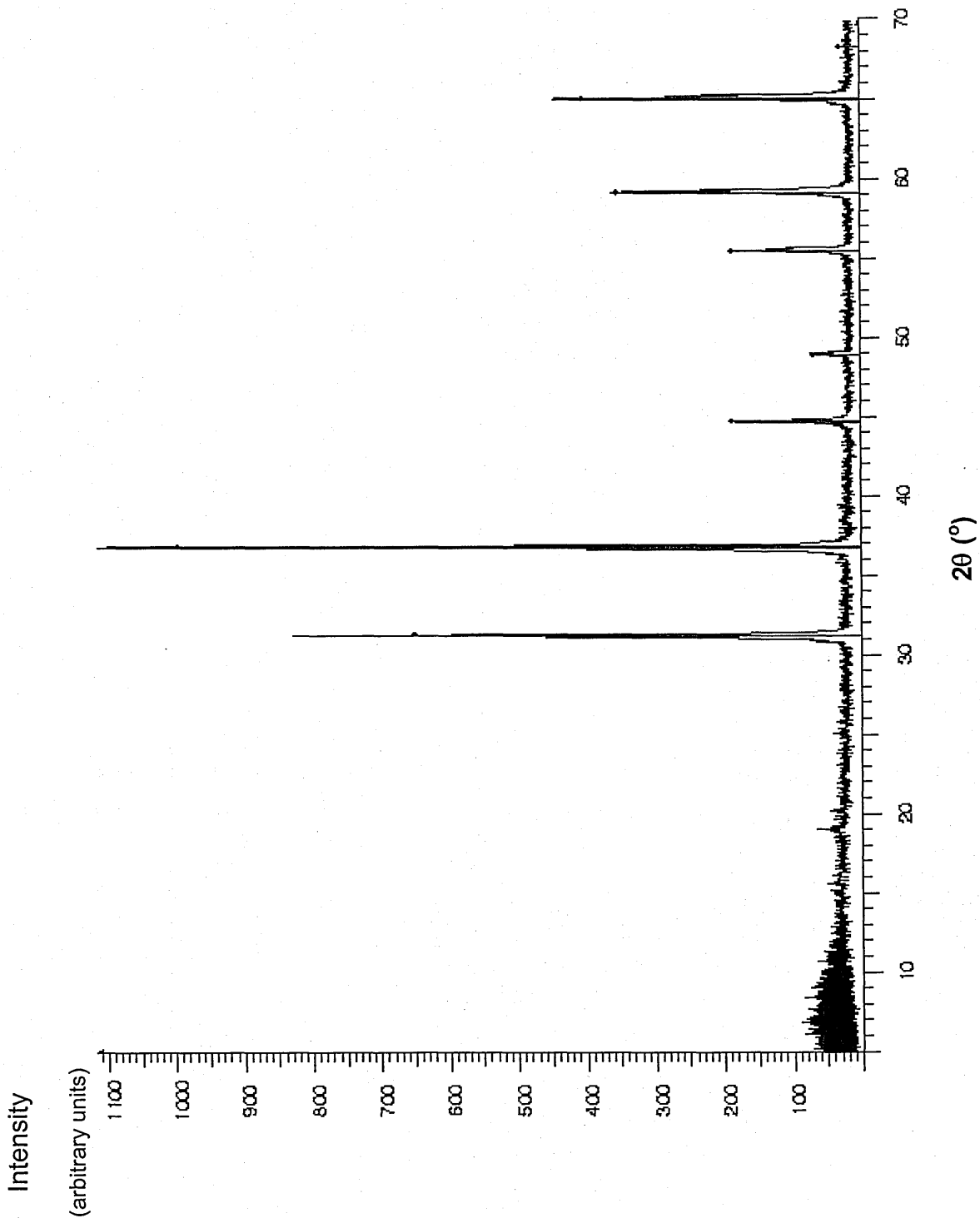

Figure 4.2.2. X-ray powder diffraction pattern recorded from a mixture of M1275 (Co_3O_4) and MO150 (γ-$Al(OH)_3$) after the material was heated at 1400 °C for 48 hours. Blue bars beneath the pattern indicate the position of reflections reported in the literature as characteristic of $CoAl_2O_4$[77].

	Temp °C	γ-$Al(OH)_3$	α-Al_2O_3	$CoAl_2O_4$	CoO	Co_3O_4	Pt
Heating	30	√				√	√
	850					√	√
	950				√	trace	√
	1000				√		√
	1050		√	√	√		√
	1100		√	√	√		√
	1150		√	√	√		√
	1200			√	√		√
Cooling	1200			√	√		√
	1000			√	√		√
	800			√	trace	√	√
	30			√	trace	√	√

Table 4.2.1.2. Summary of the crystalline phases identified from X-ray powder diffraction patterns recorded in-situ from a mixture of M1275 (Co_3O_4) and MO150 (γ-$Al(OH)_3$) as the material was heated from 30 °C to 1200 °C and upon subsequent cooling to 30 °C.

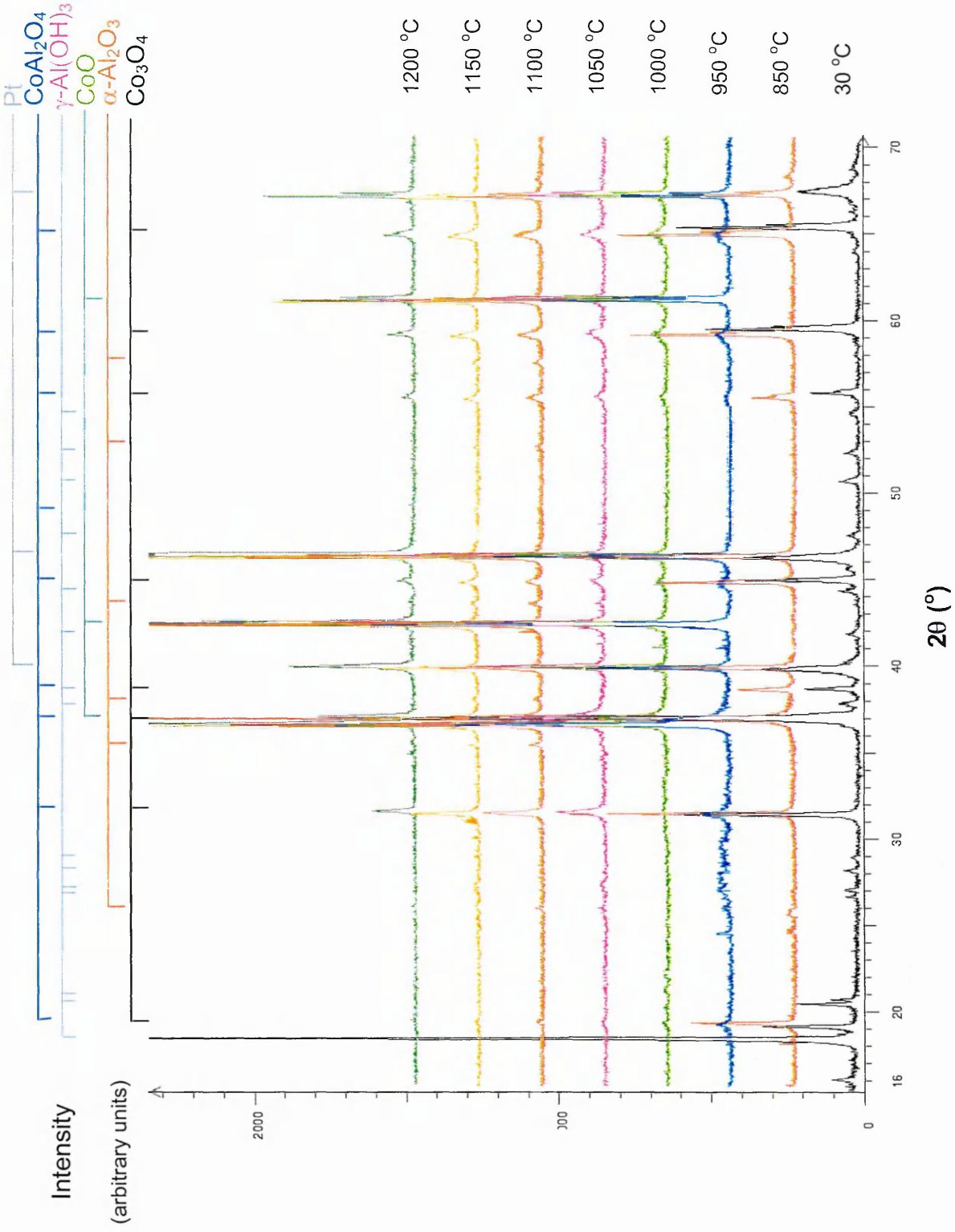

Figure 4.2.3. X-ray powder diffraction patterns recorded in-situ from a mixture of M1275 (Co_3O_4) and MO150 (γ-$Al(OH)_3$) as the material was heated between 30 °C and 1200 °C.

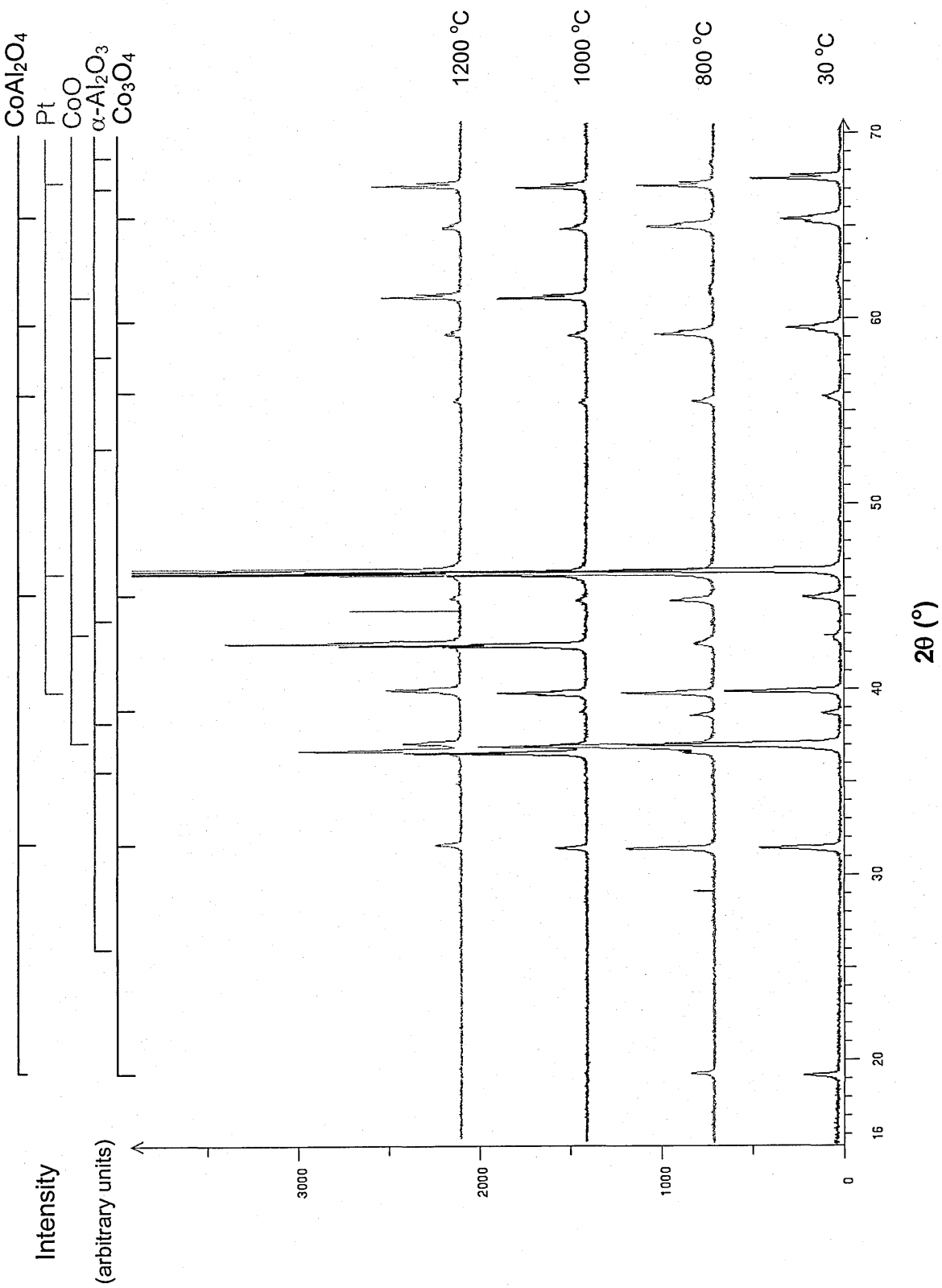

Figure 4.2.4. X-ray powder diffraction patterns recorded in-situ from a mixture of M1275 (Co_3O_4) and MO150 (γ-$Al(OH)_3$) as the material cooled from 1200 °C to 30 °C.

The X-ray powder diffraction patterns recorded *in-situ* from a mixture of M1275 and MO150 initially showed reflections at *ca.* 19 °2θ, which coincide with those reported in the literature for Co_3O_4[41], and were present at temperatures between 30 °C and 950 °C. At 950 °C the intensity of these reflections decreased and reflections *at ca.* 61.5 °2θ, which correspond with those reported in the literature for CoO[78], became apparent suggesting the reduction of Co_3O_4 to form CoO. Reflections at *ca.* 18 °2θ, that coincide with those reported for γ-$Al(OH)_3$[76], disappeared after the mixture was heated at 850 °C and very weak reflections at *ca.* 43.5 °2θ, corresponding to those reported in the literature for α-Al_2O_3[75], were visible between 1050 °C and 1150 °C.

Reflections at *ca.* 32 °2θ, associated with $CoAl_2O_4$ appeared at 1050 °C and remained present in the patterns recorded as the material was further heated and subsequently cooled. Reflections from CoO remained in the patterns recorded between 950 °C and 1200 °C and upon cooling to 30 °C, however the intensity of these reflections was very weak at 800 °C and 30 °C during the cooling regime, corresponding to partial oxidation of CoO to Co_3O_4 during cooling.

These results, together with the data recorded in Table 4.2.1.1, are consistent with the partial reaction of cobalt oxide species with either α-Al_2O_3, and/or its precursors during the transition from γ-$Al(OH)_3$. Since M1275 and MO150 were mixed in stoichiometric proportions to form $CoAl_2O_4$, the presence of excess Co_3O_4 after the material cooled showed the reaction had not reached completion. The particle size of MO150 is relatively large and the intimacy of mixing is low, incomplete reaction is therefore consistent with the results

recorded in Section 4.1, where Co_3O_4 was shown to reduce to CoO at high temperature and to then partially oxidise during subsequent cooling, re-forming Co_3O_4 if atmospheric oxygen is readily available.

The form in which the corresponding excess of aluminium oxide exists is not entirely clear from the X-ray powder diffraction patterns. However, since the MO150 is initially comprised of large particles, >100 μm diameter (discussed in greater detail in section 4.3), it is possible that a reaction occurs with cobalt oxide species at the surface, producing $CoAl_2O_4$. A surface coating of $CoAl_2O_4$ might mask in the X-ray powder diffraction pattern, the presence of a central α-Al_2O_3 core. This would account for the aluminium oxide not being detected by X-ray powder diffraction.

4.2.2 Mixture of M1275 (Co_3O_4) and AA101 (γ-AlO(OH) and α-Al_2O_3)

The X-ray powder diffraction patterns recorded from the pre-milled 1 mol : 6 mol mixture of M1275 and AA101 (Section 3.1.1) after the material was heated to temperatures between 25 °C and 1400 °C for 1 hour are shown in Figure 4.2.5. The crystalline phases identified from the X-ray powder diffraction patterns are summarised in Table 4.2.2.1.

Although the X-ray powder diffraction pattern recorded from the AA101 reagent (Figure 4.1.12) showed a broad reflection at *ca.* 67 °2θ and peaks of weak intensity at *ca.* 37 °2θ, 43 °2θ and 46 °2θ, which might be associated with γ-AlO(OH) and α-Al_2O_3, the patterns in Figure 4.2.5 failed to show any specific reflections from aluminium-containing phases until the mixture was heated at 1000 °C and weak reflections at *ca.* 25.5 and 43.5 °2θ, characteristic of α-Al_2O_3[75] appeared. The intensity of these reflections

increased at 1100 °C, and then disappeared completely after heating at 1200 °C.

This suggests that at least a significant proportion of the aluminium species react to form corundum in the same manner as observed when the material was heated in the absence of cobalt species (Section 4.1.4) and then reacts with cobalt oxide to form $CoAl_2O_4$.

The temperature at which the corundum is observed to form and subsequently be consumed are lower than those observed in Section 4.2.1 for MO150. This may be due to the smaller particle size of AA101 as compared to MO150 that results in an increased rate of reaction between the cobalt- and the aluminium-containing phases.

The intensity of reflections ca. 38.5 °2θ, characteristic of Co_3O_4, decreased after the material was heated above 1000 °C. This corresponded with the formation of $CoAl_2O_4$ as evidenced by the characteristic reflection of $CoAl_2O_4$ at *ca.* 49 °2θ which appeared after heating at 1000 °C and which increased in intensity as the material was heated further. Above 1000 °C the extent of reaction increased until single phase $CoAl_2O_4$ was formed when the material was heated at temperatures exceeding 1200 °C.

The X-ray powder diffraction pattern recorded from a mixture of M1275 and AA101 after the material was heated at 1400 °C for 48 hours is shown in Figure 4.2.6 and coincides with that reported in the literature for $CoAl_2O_4$[77].

In summary, these results show that significant quantities of AA101 formed α-Al_2O_3 at 1000 °C. The α-Al_2O_3 phase was not present after the mixture was heated at 1200°C, demonstrating that $CoAl_2O_4$ formation from these reagents occurs by direct reaction between α-Al_2O_3 and cobalt-containing species.

Temperature of heating °C	α-Al_2O_3	Co_3O_4	$CoAl_2O_4$
25		√	
500		√	
700		√	
800		√	
900		√	
1000	√	√	√
1100	√	√	√
1200		√	√
1300			√
1400			√
1400 (held for 48 hours)			√

Table 4.2.2.1. Summary of crystalline phases identified by X-ray powder diffraction recorded from a mixture of M1275 (Co_3O_4) and AA101 (primarily γ-AlO(OH)) heated to temperatures up to 1400 °C for 1 hour and, in the final case, at 1400 °C for 48 hours.

The occurrence of alternative mechanisms involving the reaction between precursors of α-Al_2O_3 and cobalt-containing species or the reaction with cobalt-containing species and aluminium oxides during the transition from cubic-close packed gamma to hexagonal-close packed alpha phases are not apparent from these results.

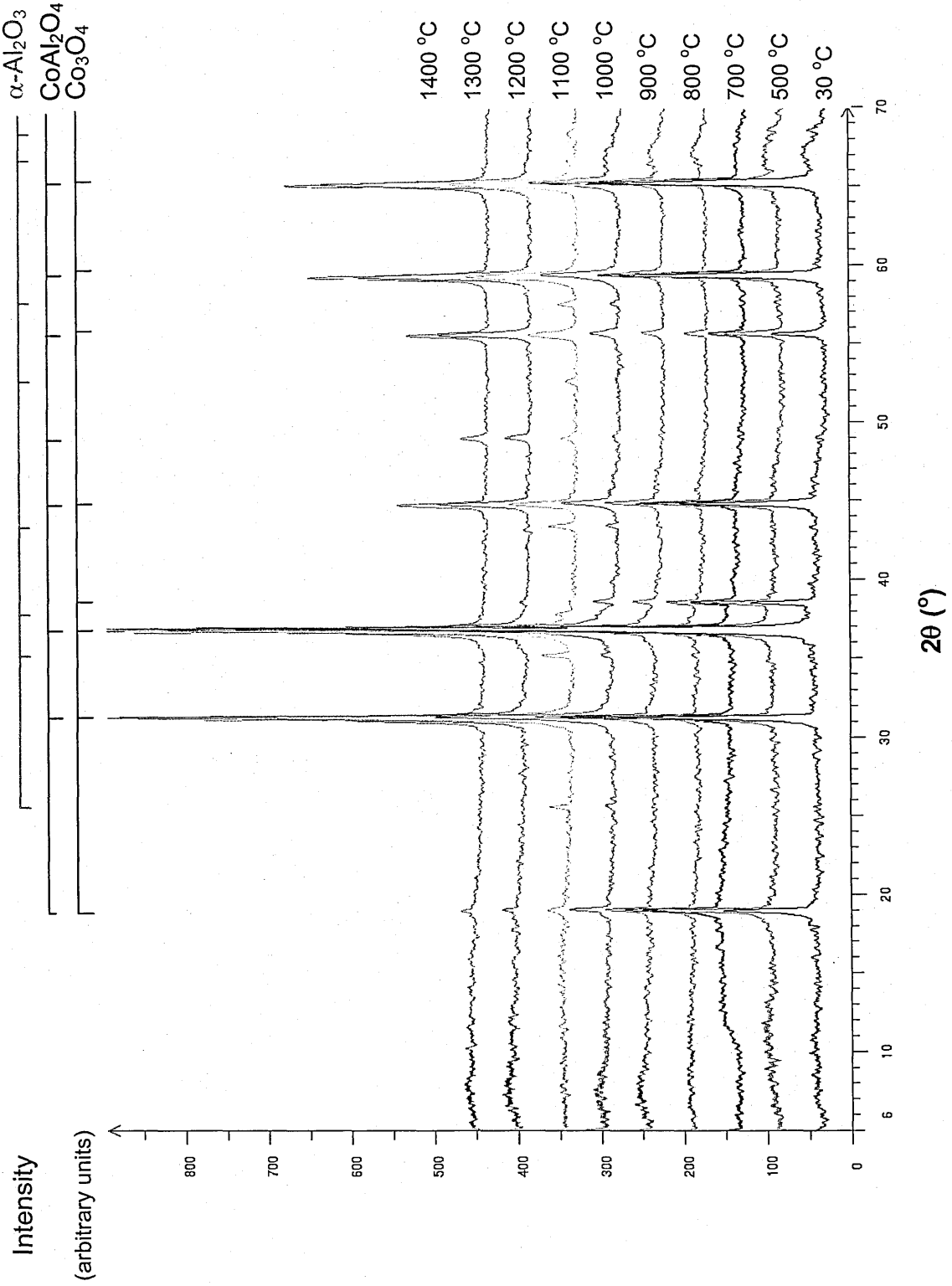

Figure 4.2.5. X-ray powder diffraction patterns recorded from a mixture of M1275 (Co_3O_4) and AA101 (primarily γ-AlO(OH)) heated to temperatures of up to 1400 °C for 1 hour.

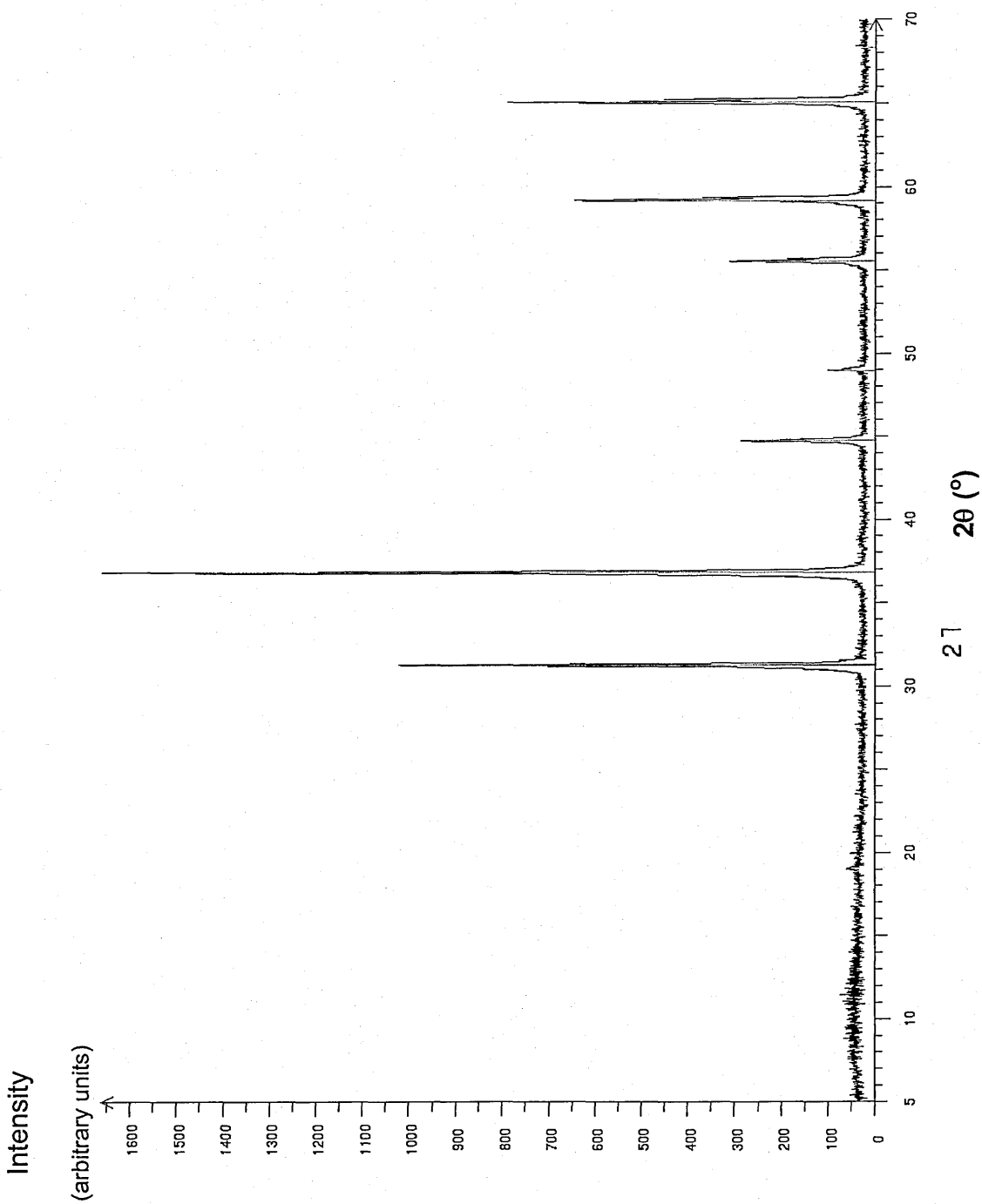

Figure 4.2.6. X-ray powder diffraction pattern recorded from a mixture of M1275 (Co_3O_4) and AA101 (primarily γ-AlO(OH)) heated to 1400 °C for 48 hours. Red bars indicate the position of reflections reported in the literature as characteristic of $CoAl_2O_4$[77].

4.2.3 Mixture of M1275 (Co_3O_4) and Baco MA95 (α-Al_2O_3)

The X-ray powder diffraction patterns recorded from a pre-milled 1 mol : 3 mol mixture of M1275 and Baco MA95 (Section 3.1.1) after heating to temperatures up to 1400 °C for 1 hour are shown in Figure 4.2.7. The crystalline phases identified from the X-ray powder diffraction patterns are summarised in

Table 4.2.3.1.

The X-ray powder diffraction patterns show that reflections at *ca.* 25.5 and 43.5 °2θ, coinciding with those reported in the literature[75] for α-Al_2O_3 and at *ca.* 38.5 °2θ corresponding to Co_3O_4 were present in those materials heated between 30 °C and 1100 °C. The intensity of reflections from α-Al_2O_3 and Co_3O_4 decreased significantly above 1100 °C and was concurrent with the appearance at ca. 49 °2θ of reflections from $CoAl_2O_4$.

The X-ray powder diffraction pattern recorded from a mixture of M1275 and Baco MA95 after the material was heated at 1400 °C for 48 hours is shown in Figure 4.2.8. This pattern showed reflections that coincide with those reported in the literature[77] for $CoAl_2O_4$.

In summary, these results demonstrate the direct reaction between α-Al_2O_3 and Co_3O_4 to form $CoAl_2O_4$ in materials heated at 1100 °C for 1 hour and show that the extent of reaction increased with temperature.

The absence of α-Al_2O_3 from the pattern recorded at 1200 °C suggests that the reaction between α-Al_2O_3 and Co_3O_4 is more rapid than that observed when Co_3O_4 reacts with γ-$Al(OH)_3$ as reported in Section 4.2.1.

Temperature °C	α-Al_2O_3	Co_3O_4	$CoAl_2O_4$
30	√	√	
500	√	√	
700	√	√	
800	√	√	
900	√	√	
1000	√	√	
1100	√	√	√
1200			√
1300			√
1400			√
1400 (held for 48 hours)			√

Table 4.2.3.1. Summary of crystalline phases identified from X-ray powder diffraction patterns recorded from a mixture of M1275 (Co_3O_4) and Baco MA95 (α-Al_2O_3) heated to 1400 °C for 1 hour and, in the final case, at 1400 °C for 48 hours.

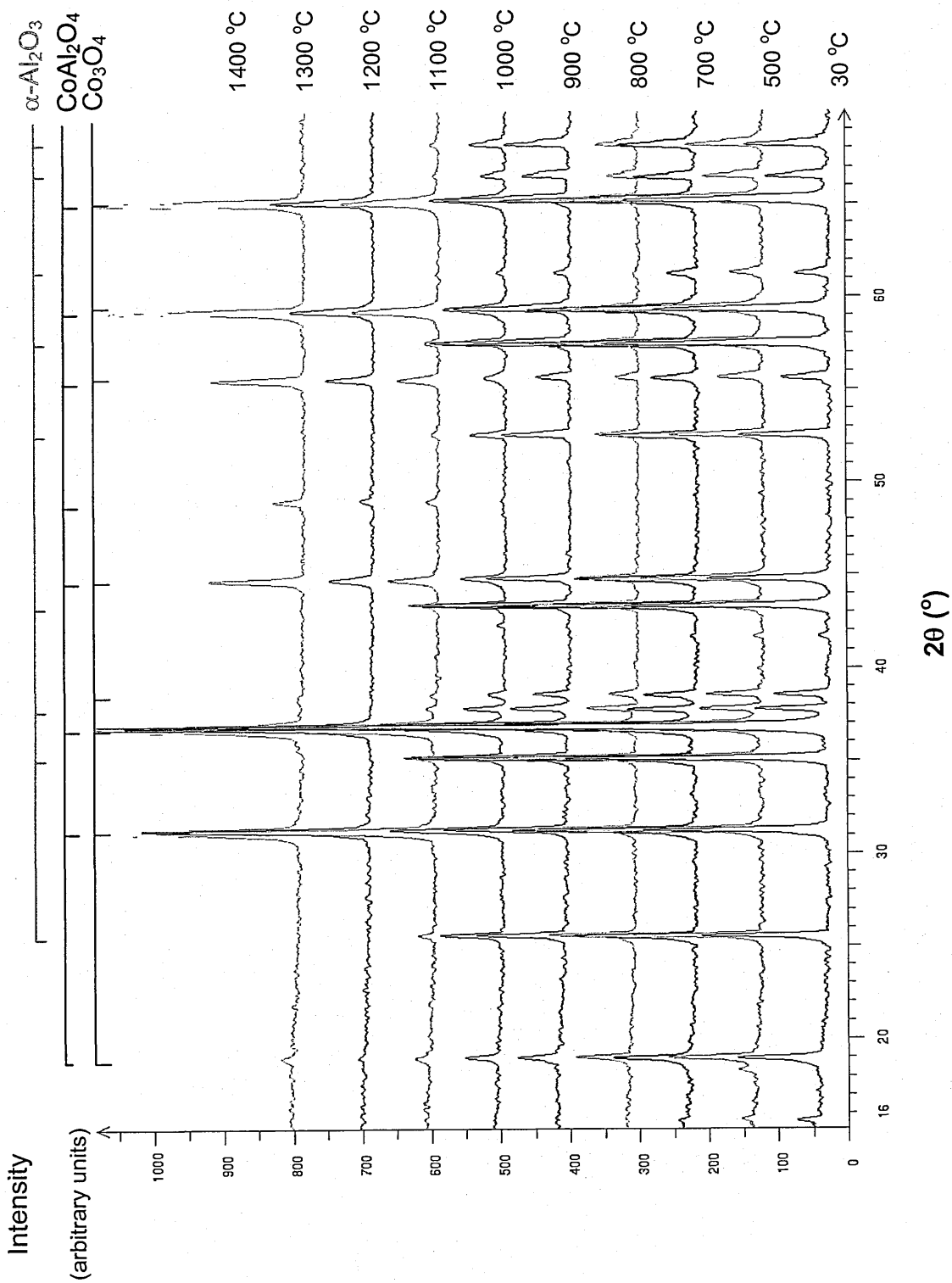

Figure 4.2.7. X-ray powder diffraction patterns recorded from a mixture of M1275 (Co_3O_4) and Baco MA95 (α-Al_2O_3) heated to temperatures up to 1400 °C for 1 hour.

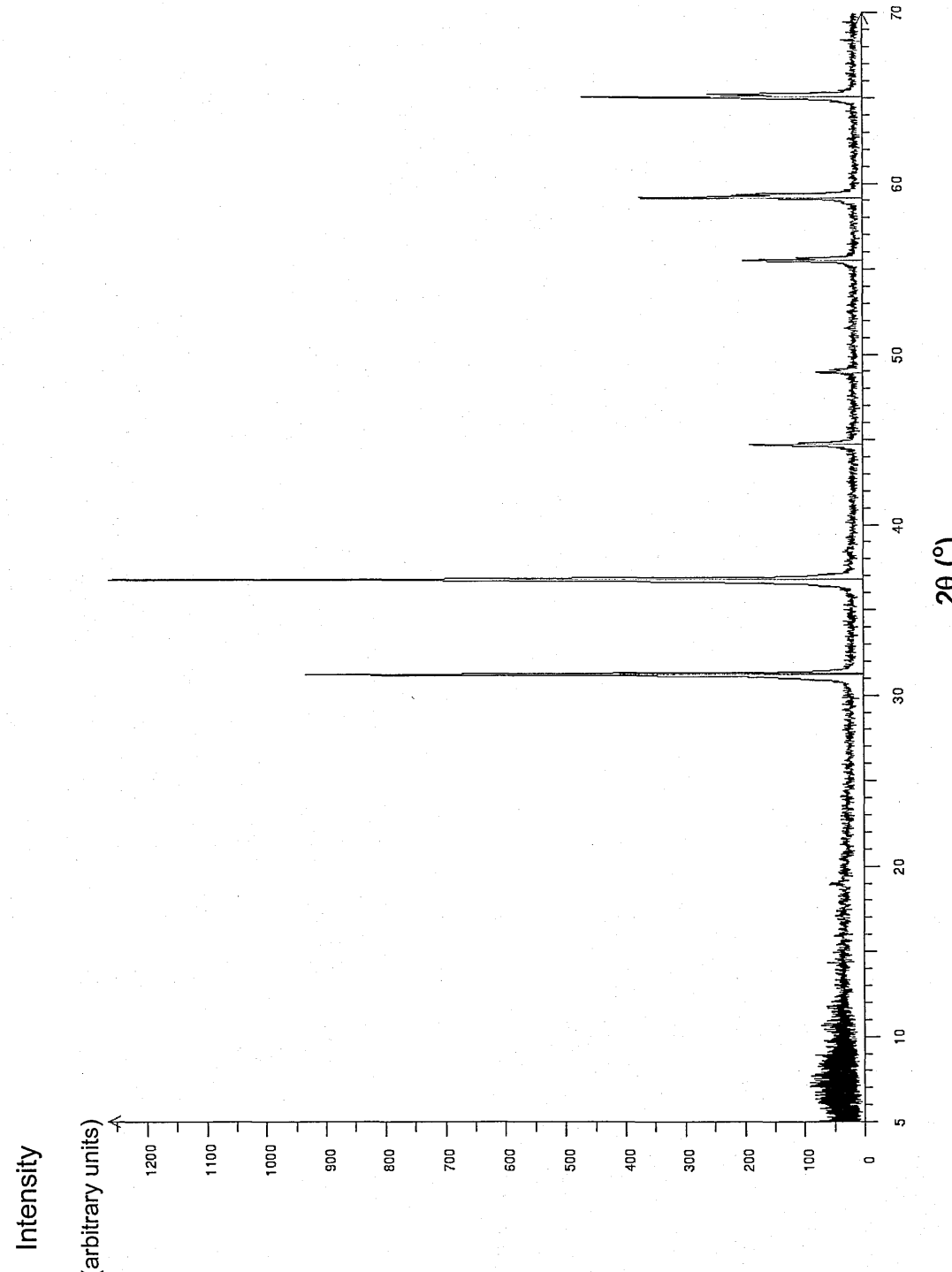

Figure 4.2.8. X-ray powder diffraction pattern recorded from a mixture of M1275 (Co_3O_4) and Baco MA95 (α-Al_2O_3) heated at 1400 °C for 48 hours. Red bars indicate the position of reflections reported in the literature for $CoAl_2O_4$[77].

In summary, the work reported in Section 4.2 showed that;

- Al_2O_3 with a corundum structure is formed at 1100 °C when MO150 (γ-$Al(OH)_3$) is heated in the presence of M1275 (Co_3O_4).
- The aluminium- and cobalt-containing species react to form $CoAl_2O_4$ at temperatures exceeding 1000 °C.
- Two parallel mechanisms may occur;
    (a) CoO and γ-Al_2O_3 react to form $CoAl_2O_4$ during the cubic-close packed to hexagonal-close packed lattice rearrangement of the aluminium oxide.
    (b) γ-Al_2O_3 forms corundum (α-Al_2O_3) which proceeds to react directly with CoO to form $CoAl_2O_4$.
- During the reaction of Co_3O_4 (M1275) and γ-$Al(OH)_3$ (MO150), excess corundum may exist as a central core within an outer layer of $CoAl_2O_4$ if the initial particle size of γ-$Al(OH)_3$ particles is sufficiently large and the temperature/time insufficient for complete reaction.
- Heating at 1400 °C for 1 hour is sufficient for the complete reaction of M1275 (Co_3O_4) and either MO150 (γ-$Al(OH)_3$), AA101 (γ-AlO(OH)/α-Al_2O_3) or Baco MA95 (α-Al_2O_3) to form $CoAl_2O_4$.
- The direct reaction of cobalt-containing species and corundum (α-Al_2O_3) is demonstrated by the formation of $CoAl_2O_4$ from M1275 (Co_3O_4) and Baco MA95 (α-Al_2O_3).

4.3 Effect of pre-milling processes on cobalt aluminate ($CoAl_2O_4$) formation

4.3.1 Effect of bead milling on M1275 (Co_3O_4)

Scanning electron micrographs of non-milled M1275 (Co_3O_4) are shown in Figure 4.3.1. and Figure 4.3.2. These show that non-milled M1275 consisted of evenly sized agglomerates of less than 5μm diameter with a primary particle size, that is the size of the particles from which the agglomerates are formed, of less than 0.1μm. Micrographs of M1275 after bead milling according to the procedure described in Section 3.1.1, for periods of 1 hour and 5 hours are shown in Figure 4.3.3. to Figure 4.3.4. and showed that the primary particle size is not appreciably affected by bead milling.

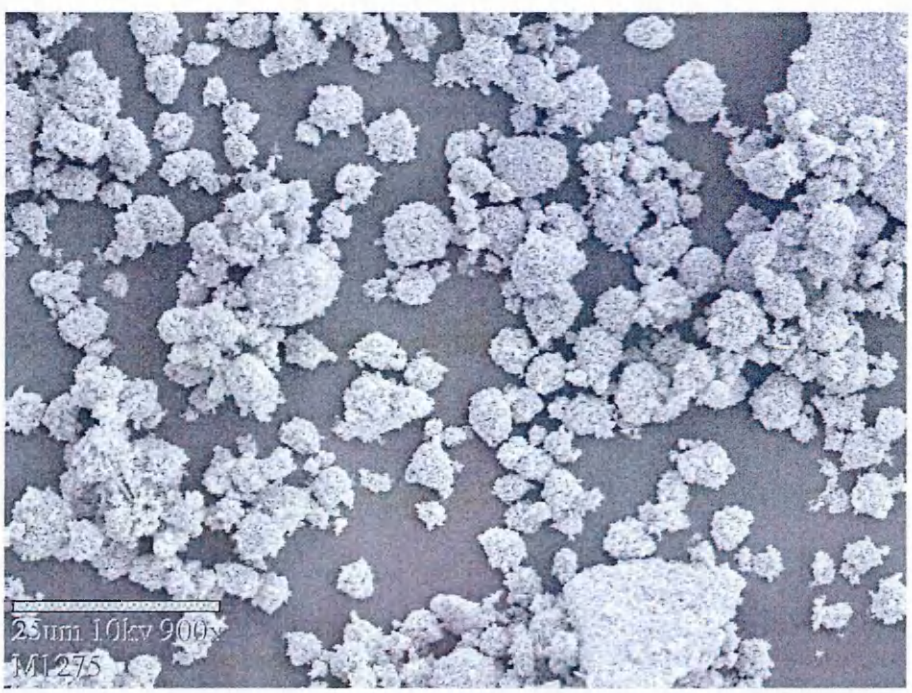

Figure 4.3.1. Scanning electron micrograph of M1275 (Co_3O_4), (x900).

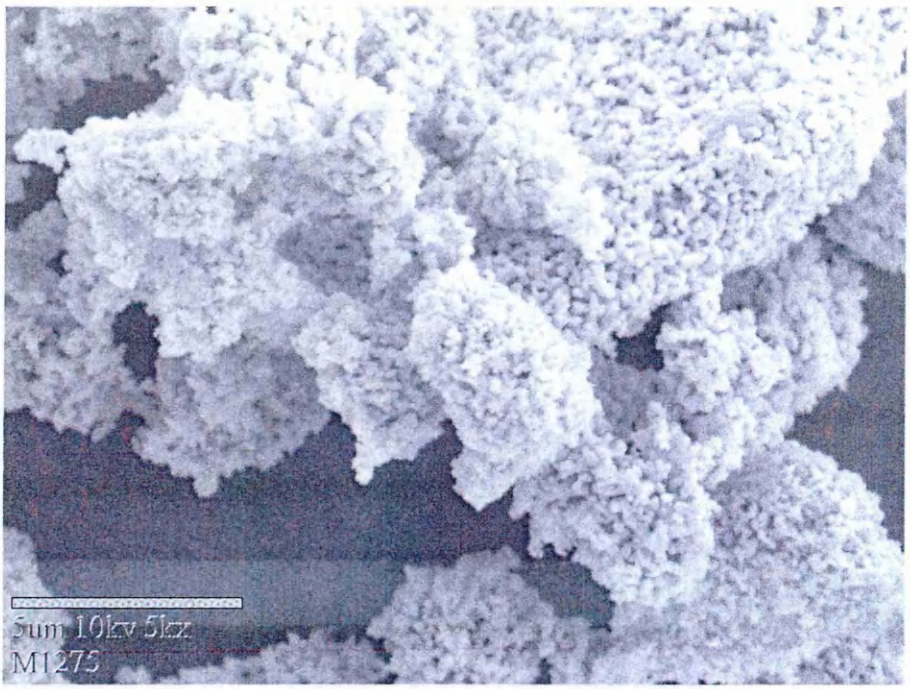

Figure 4.3.2. Scanning electron micrograph of M1275 (Co_3O_4), (x5000).

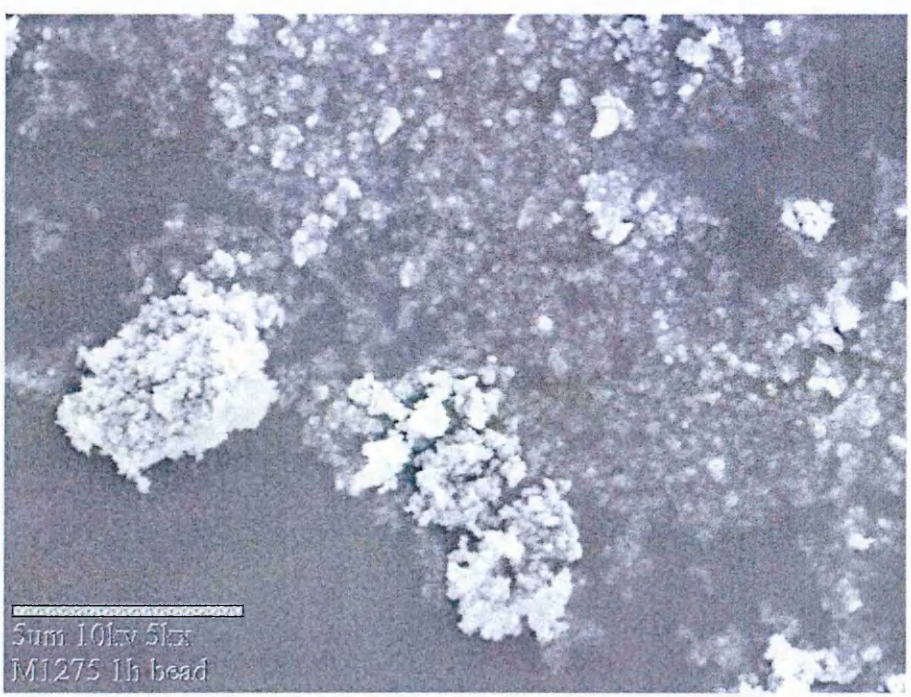

Figure 4.3.3. Scanning electron micrograph of M1275 (Co_3O_4) bead milled for 1 hour, (x5000).

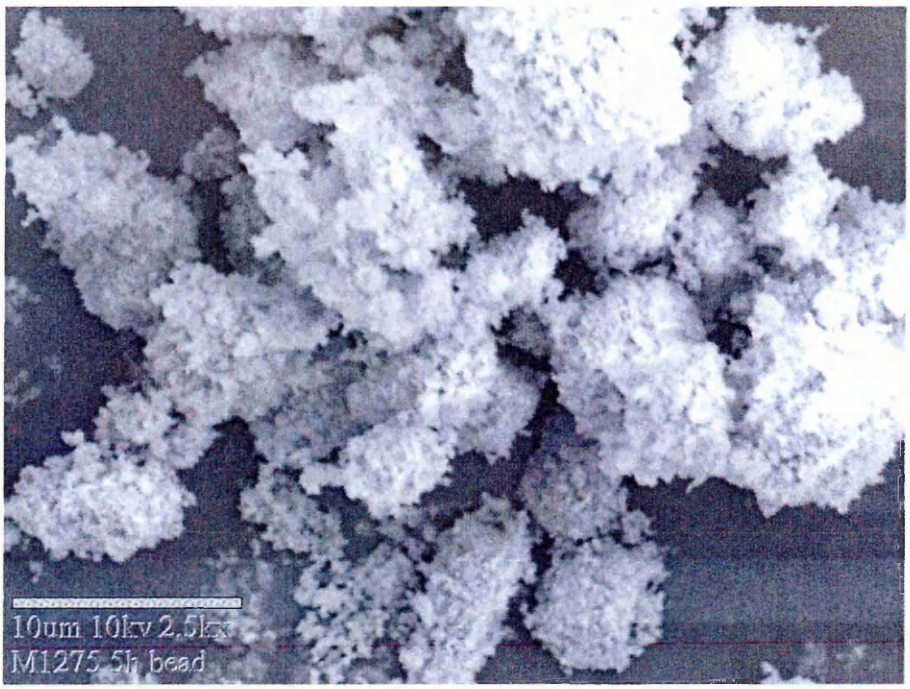

Figure 4.3.4. Scanning electron micrograph of M1275 (Co_3O_4) bead milled for 5 hours, (x2500).

4.3.2 Effect of bead milling on MO150 (γ-$Al(OH)_3$) and SF11E (γ-$Al(OH)_3$)

MO150 and SF11E are both composed of γ-$Al(OH)_3$ as demonstrated in Section 4.1. Scanning electron micrographs of non-milled MO150 and following bead milling for 1 hour and 5 hours are shown in Figure 4.3.5 to Figure 4.3.7. The micrographs show non-milled MO150 to consist of large singular particles between *ca.* 25 and 100 μm diameter that, upon bead milling for 1 hour and 5 hours, reduced significantly in size, such that small fragments, less than *ca.* 1 μm diameter of the original particle adhered together and also to the surface of the parent particles.

In contrast to MO150, SF11E had a significantly smaller original particle size (< 1 μm), shown in Figure 4.3.8 and Figure 4.3.9, and was more finely dispersed than M1275 (Figure 4.3.4) which had particles of comparable size. Furthermore, and in contrast to the results recorded from MO150, milling had little effect on the final particle size of SF11E (Figure 4.3.10)

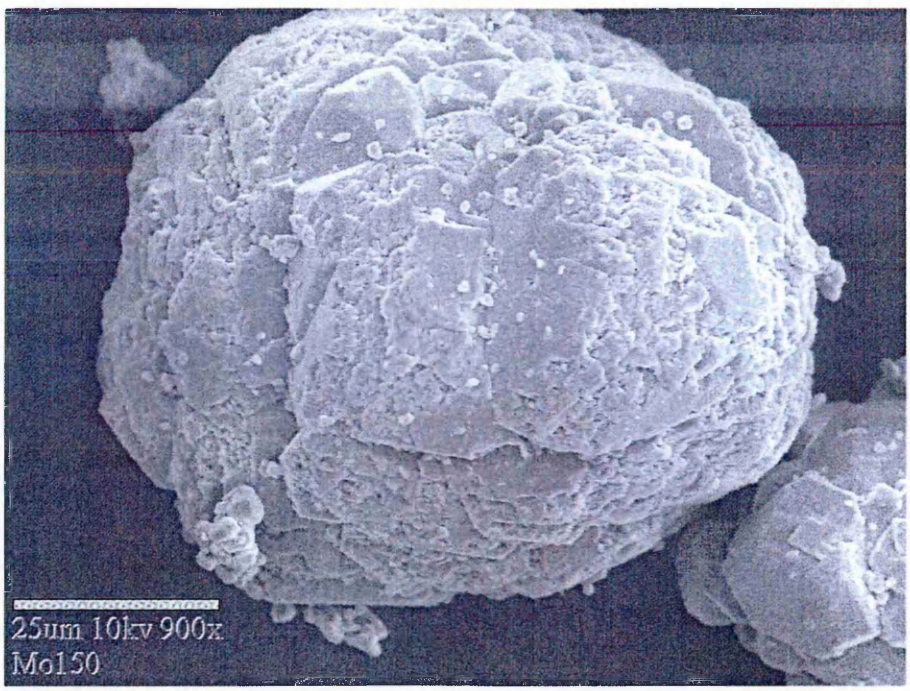

Figure 4.3.5. Scanning electron micrograph of MO150 (γ-Al(OH)$_3$), (x900)

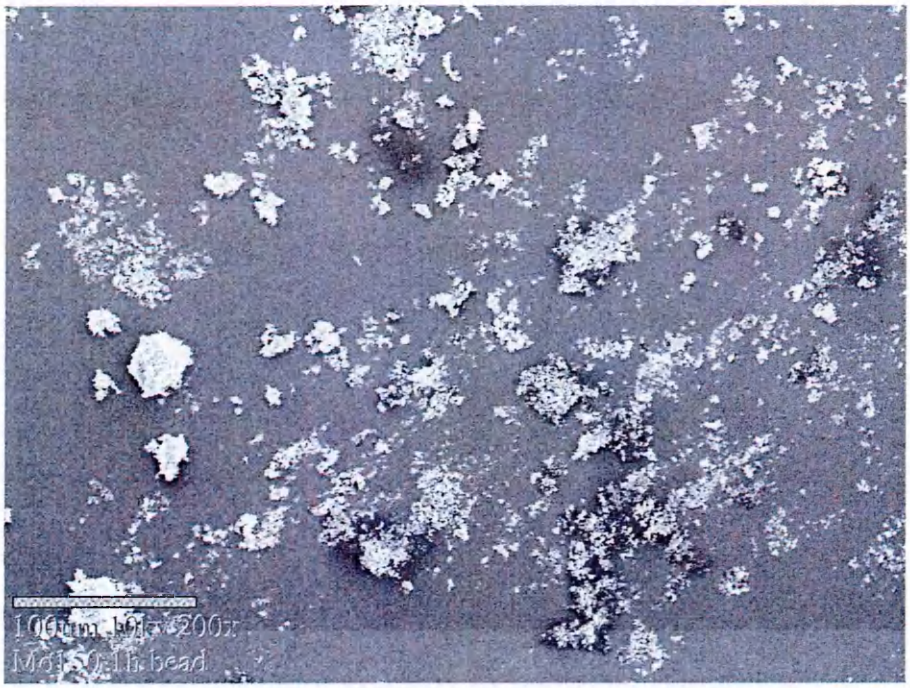

Figure 4.3.6. Scanning electron micrograph of MO150 (γ-Al(OH)$_3$), bead milled for 1 hour, (x200).

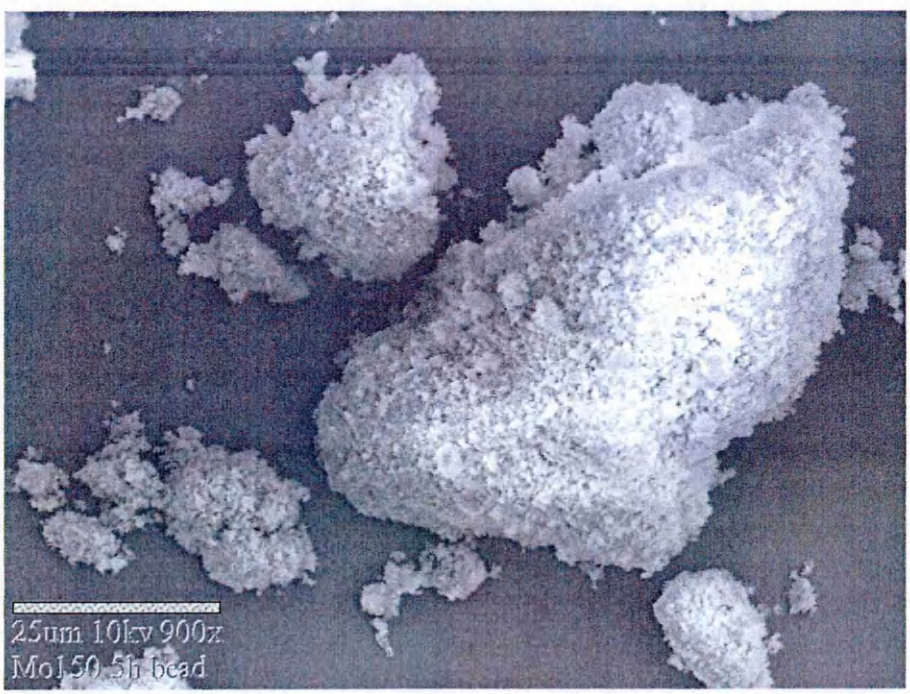

Figure 4.3.7. Scanning electron micrograph of MO150 (γ-Al(OH)$_3$), bead milled for 5 hours, (x900)

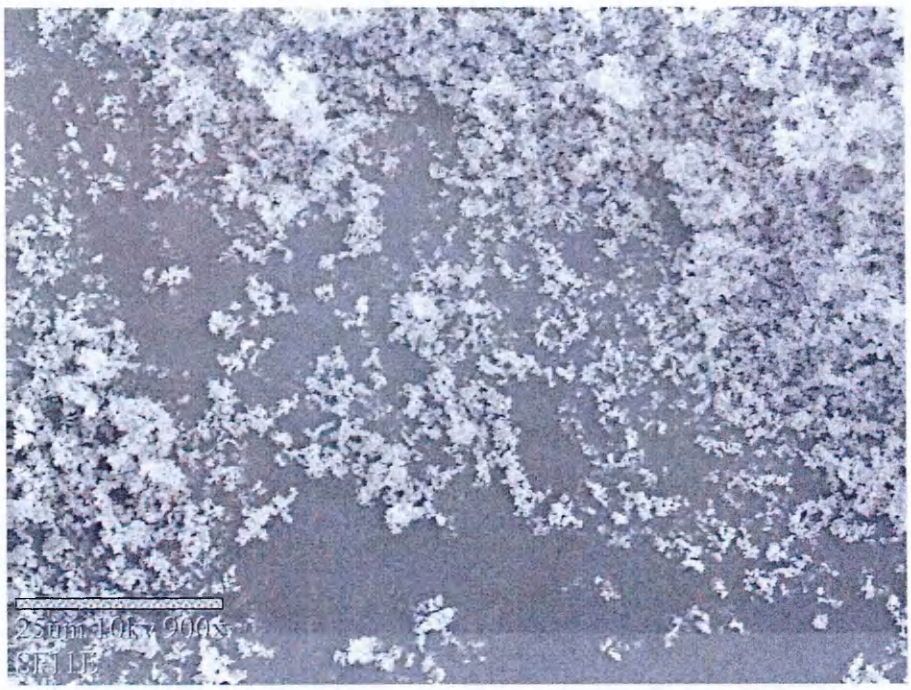

Figure 4.3.8 Scanning electron micrograph of SF11E (γ-Al(OH)$_3$), (x900)

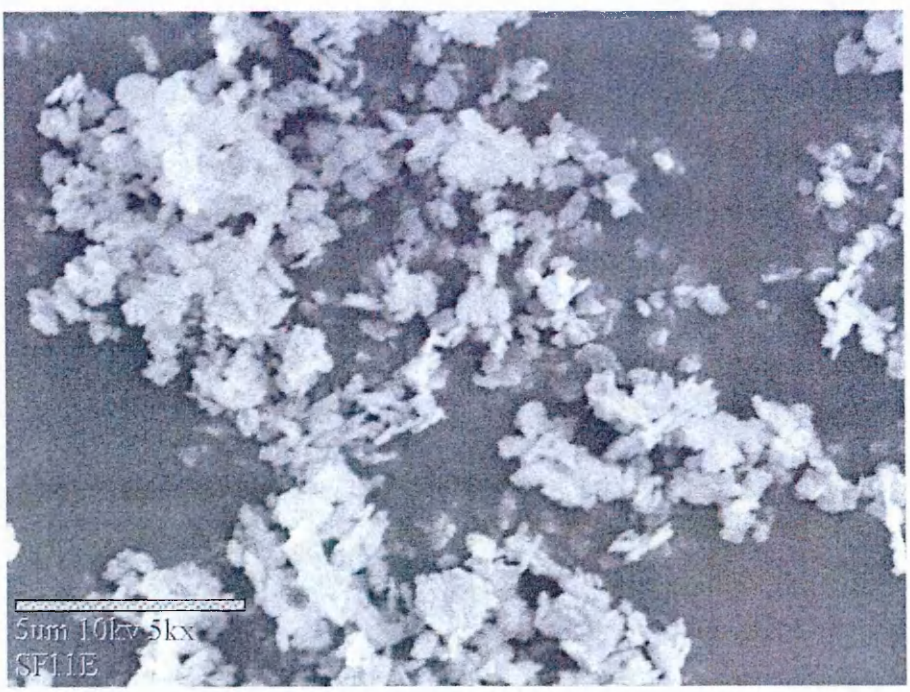

Figure 4.3.9. Scanning electron micrograph of SF11E (γ-Al(OH)$_3$), (x5000)

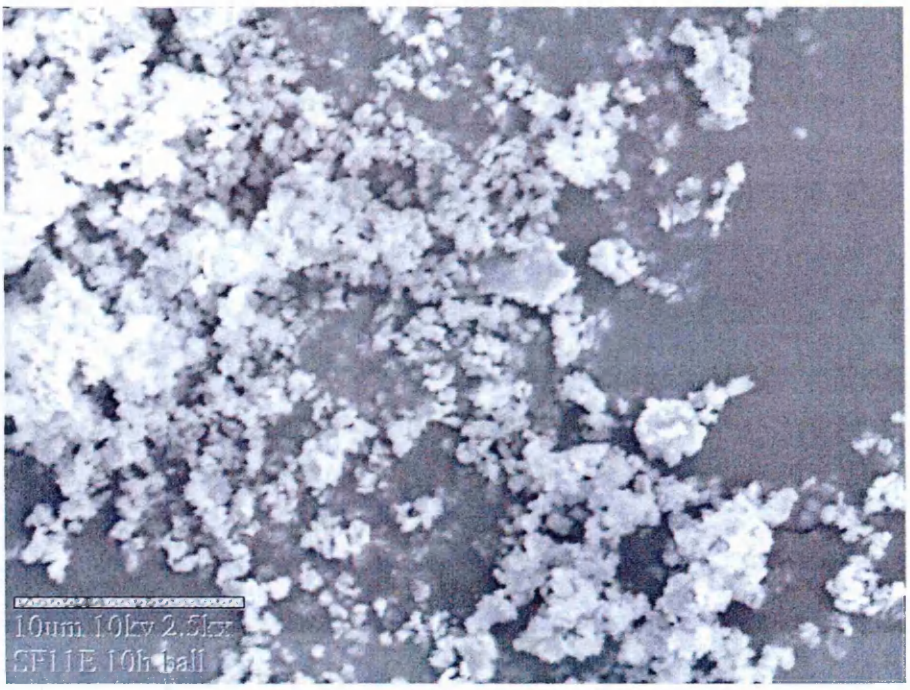

Figure 4.3.10. Scanning electron micrograph of SF11E (γ-Al(OH)$_3$), bead milled for 10 hours (x900)

4.3.3 Effect of bead milling on a mixture of M1275 (Co_3O_4) and MO150 (γ-Al(OH)$_3$)

Scanning electron micrographs from a 1 mol : 6 mol mixture of M1275 (Co_3O_4) and MO150 (γ-Al(OH)$_3$) bead milled together for various periods of time as described in Section 3.1.1, are shown in Figure 4.3.11. to Figure 4.3.15. A comparison of the scanning electron micrographs recorded from the mixture of M1275 (Co_3O_4) and MO150 (γ-Al(OH)$_3$) before milling, Figure 4.3.11, and those recorded individually from the M1275 and MO150 reagents, shown in sections 4.3.1 and 4.3.2, enables the different reagents to be identified. Energy dispersive X-ray (EDX) analysis plots, such as that shown in Figure 4.3.16 confirmed visual identification of cobalt and aluminium oxide particles shown in scanning electron micrographs.

Figure 4.3.11. shows that the non-milled material, as expected, consisted of separate Co_3O_4 and γ-$Al(OH)_3$ particles. After 15 minutes of bead milling, (Figure 4.3.12) the Co_3O_4 agglomerates appear to fragment and disperse, whilst the much larger γ-$Al(OH)_3$ particles were largely unchanged. After 30 minutes of bead milling, (Figure 4.3.13) the particles of γ-$Al(OH)_3$ appear to be coated with Co_3O_4. Further milling for 1 hour (Figure 4.3.14) and 5 hours (Figure 4.3.15) appeared to have little further effect on the distribution of the two components and on particle size.

Samples from the mixture of M1275 and MO150 were removed after milling for 15 minutes, 30 minutes, 1 hour and 5 hours. These samples, together with a sample of the unmilled mixture, were heated in air at 1250 °C for 30 minutes. X-ray powder diffraction patterns recorded from these products (Figure 4.3.17.) show that calcination of the non-milled sample produced $CoAl_2O_4$ with small quantities of the aluminium oxides, γ-AlO(OH) and α-Al_2O_3. The samples that were milled showed peaks in the X-ray powder diffraction patterns that were characteristic of $CoAl_2O_4$ and were nearly identical, although the peak at *ca.* 49 °2θ, indicative of $CoAl_2O_4$, became more pronounced as milling time increased. There were no reflections that indicated the presence of α-Al_2O_3, γ-AlO(OH) in any of the patterns recorded from milled materials.

Given that X-ray powder diffraction is only sensitive to the presence of crystalline phases present in quantities greater than *ca.* 5%, temperature programme reduction in a flowing hydrogen/nitrogen mixture, was used to further characterise the samples.

Figure 4.3.11. Scanning electron micrograph from a mixture of M1275 (Co_3O_4) and MO150 (γ-$Al(OH)_3$), un-milled, (x200).

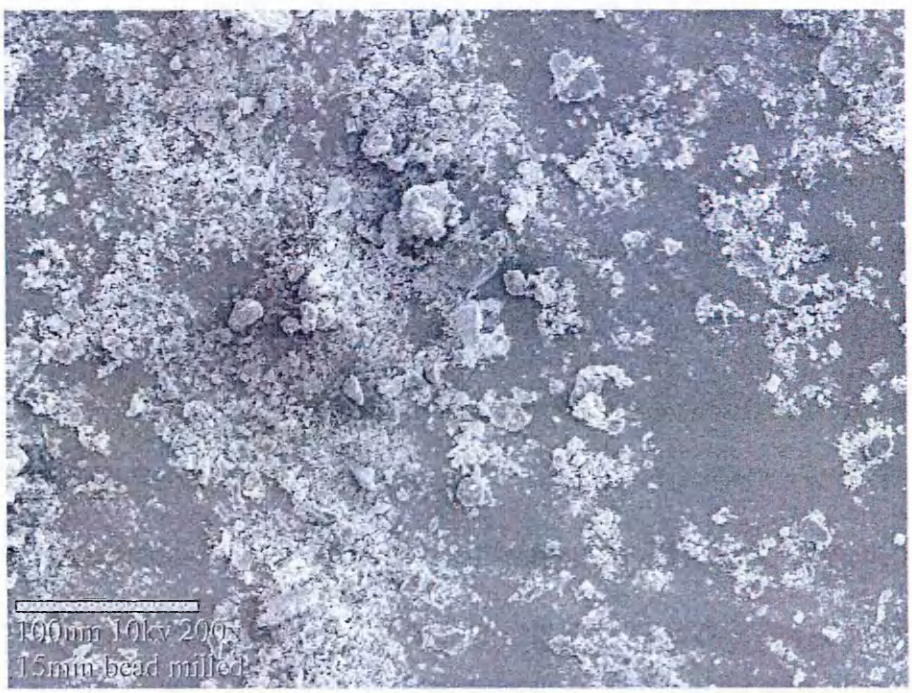

Figure 4.3.12. Scanning electron micrograph from a mixture of M1275 (Co_3O_4) and MO150 (γ-$Al(OH)_3$), bead milled together for 15 minutes, (x200).

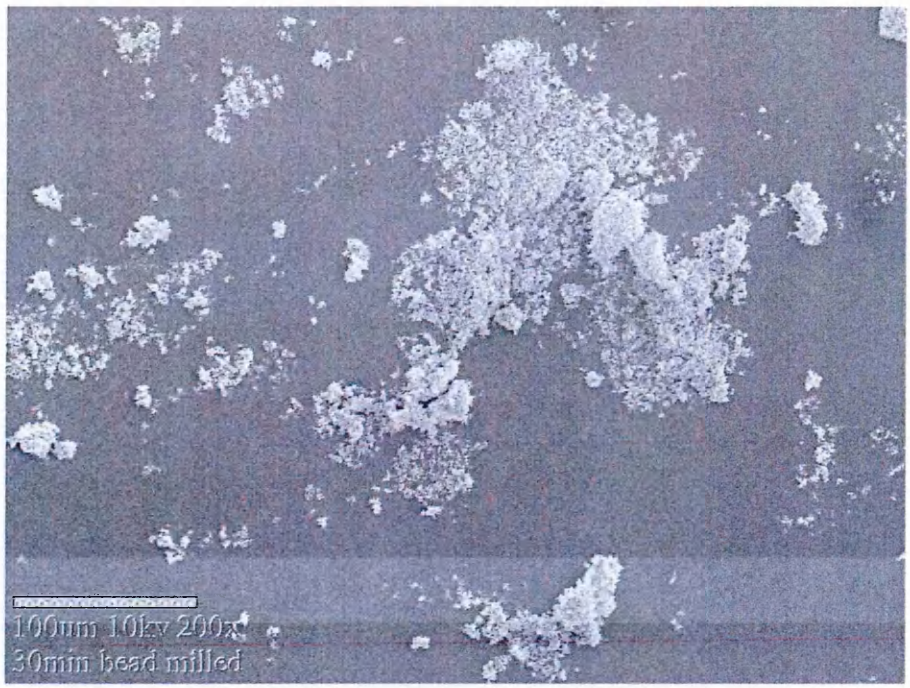

Figure 4.3.13. Scanning electron micrograph from a mixture of M1275 (Co_3O_4) and MO150 (γ-$Al(OH)_3$), bead milled together for 30 minutes, (x200).

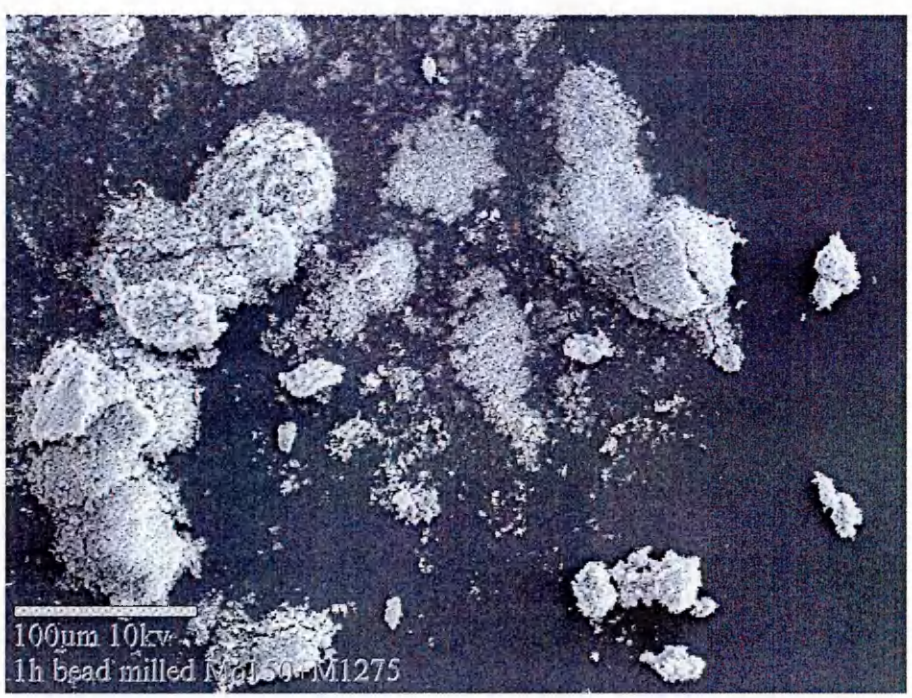

Figure 4.3.14. Scanning electron micrograph from a mixture of M1275 (Co_3O_4) and MO150 (γ-$Al(OH)_3$), bead milled together for 1 hour, (x200).

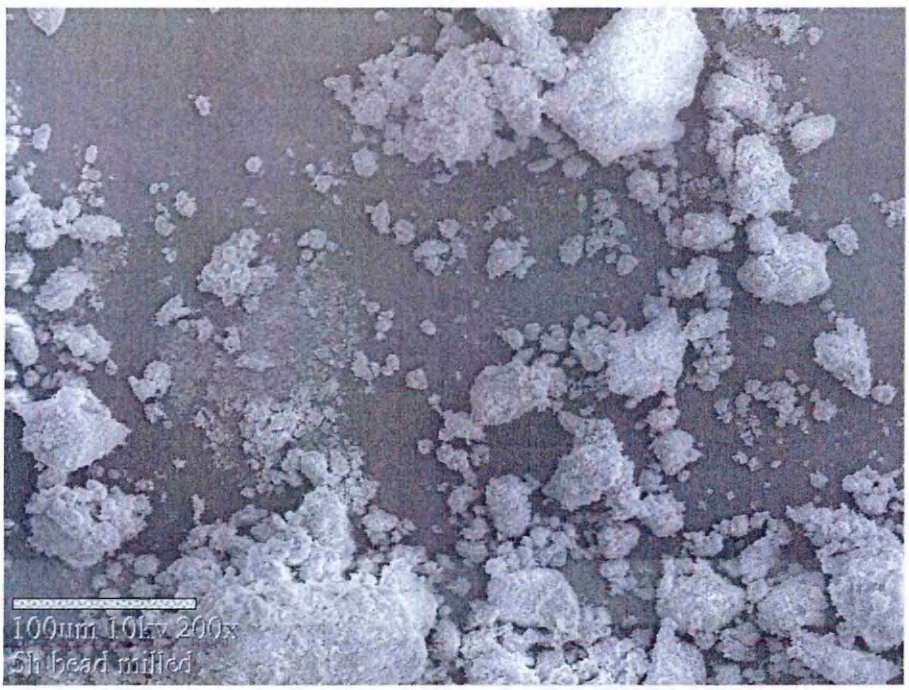

Figure 4.3.15. Scanning electron micrograph from a mixture of M1275 (Co_3O_4) and MO150 (γ-$Al(OH)_3$), bead milled together for 5 hours, (x200).

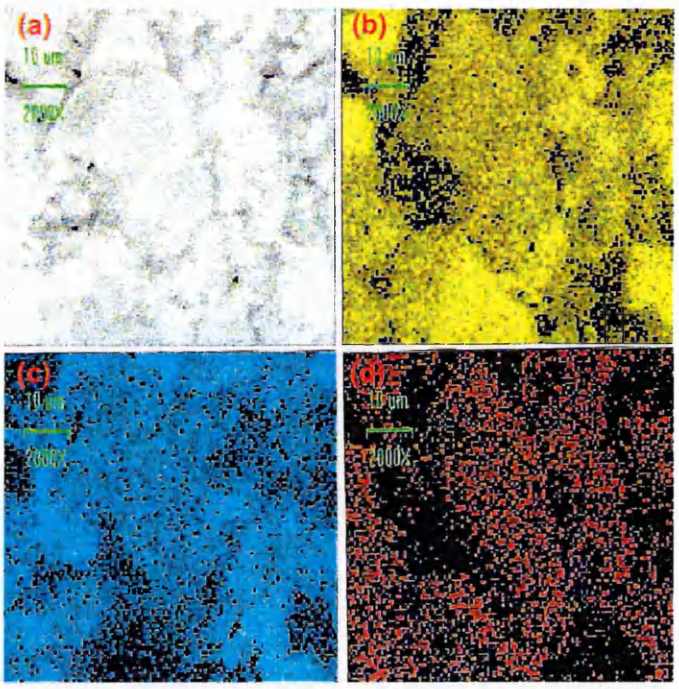

Figure 4.3.16 Scanning electron microscope image (a) of a mixture of M1275 (Co_3O_4) and MO150 (γ-$Al(OH)_3$, and EDX analysis of the mixture showing distribution of (b) aluminium, (c) cobalt, and (d) oxygen.

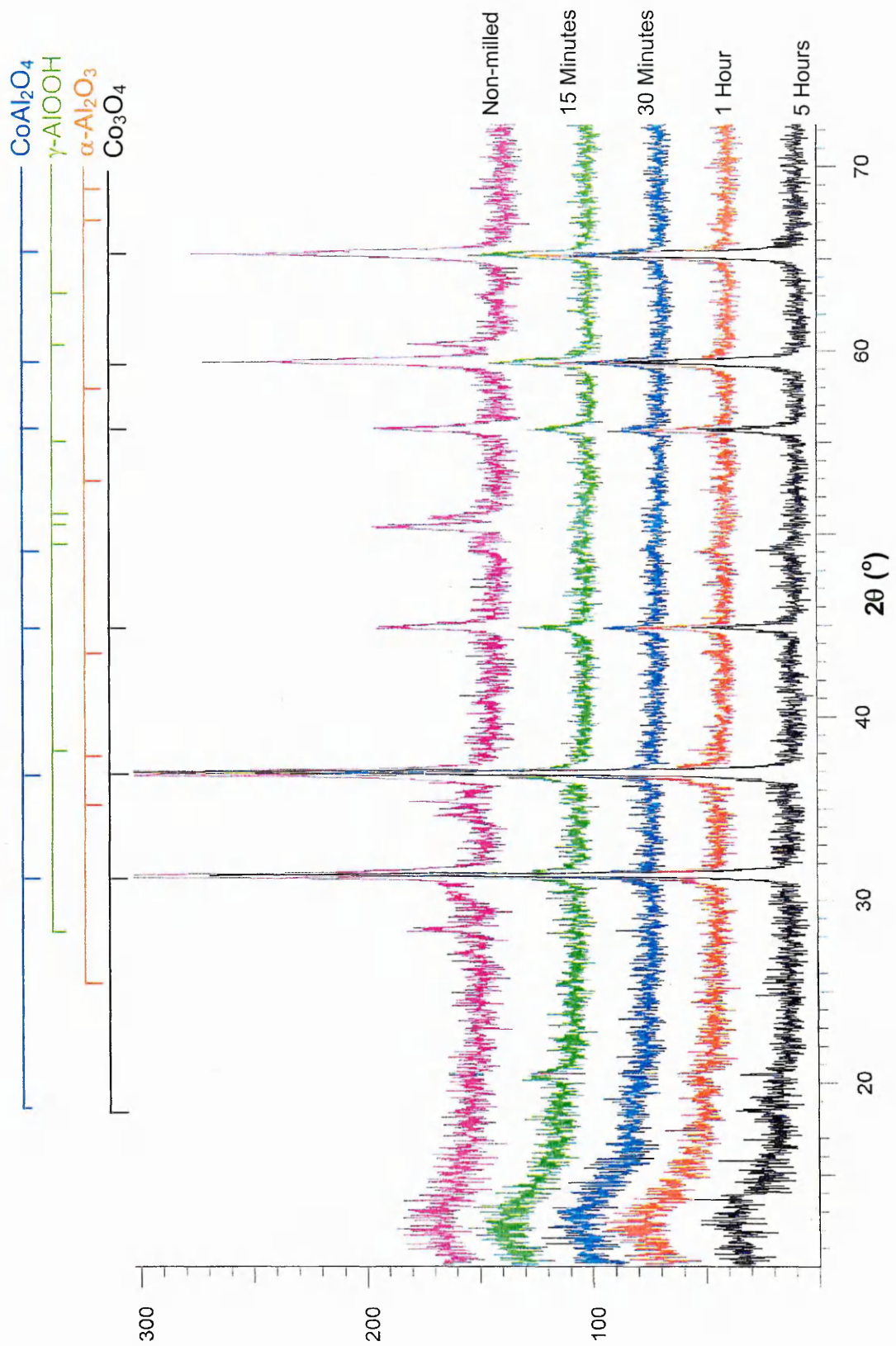

Figure 4.3.17. X-ray powder diffraction patterns recorded from a mixture of M1275 (Co_3O_4) and MO150 (γ-$Al(OH)_3$) bead milled for periods up to 5 hours and then heated to 1250 °C for 30 minutes hour.

Temperature programme reduction measures the consumption of hydrogen as it is passed over an oxide as a function of increasing temperature. Temperature programme reduction profiles of Co_3O_4 (M1275) and CoO (produced by heating M1275 at 1400 °C for 5 days and rapidly cooling) are shown in Figure 4.3.18. The temperature programme reduction profile recorded from Co_3O_4 shows absorption of hydrogen at *ca.* 310 °C and that recorded from CoO shows absorption of hydrogen at *ca.* 360 °C. Neither of these phases absorbs hydrogen at temperatures exceeding 400 °C.

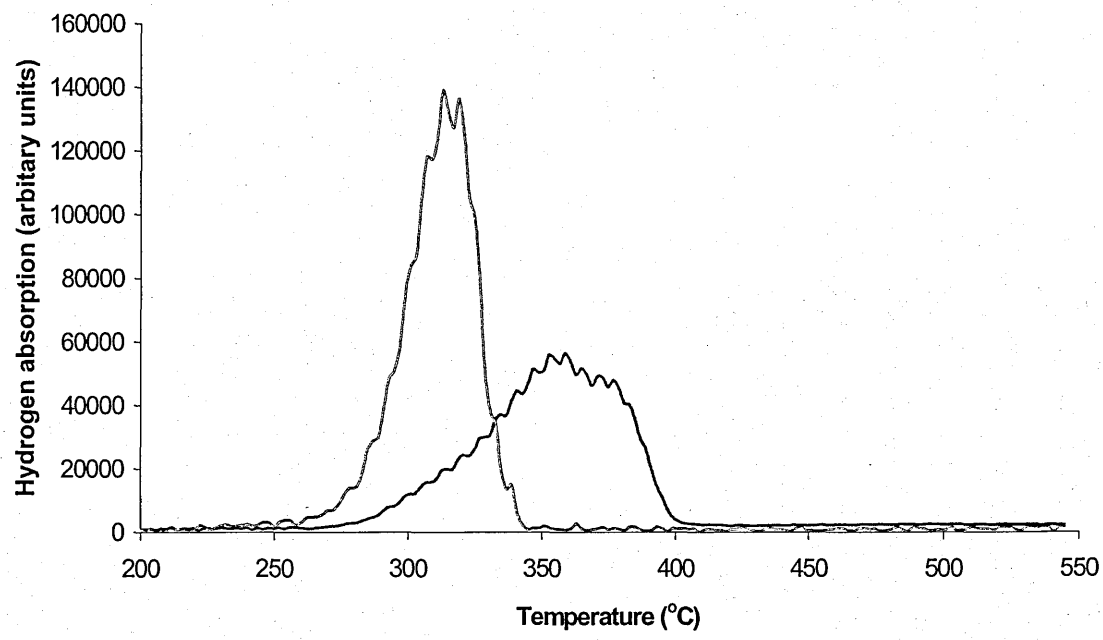

Figure 4.3.18 Temperature programme reduction profiles recorded from CoO (Blue) and Co_3O_4 (Red).

A 1:6 mixture of Co_3O_4 (M1275) and γ-$Al(OH)_3$ (MO150) was subsequently prepared. One sample was retained un-milled, the remainder was bead

milled and samples taken after milling for 15 minutes, 30 minutes, 1 hour and 5 hours. All five samples were then calcined in air at 1250 °C for 30 minutes. The temperature programme reduction profiles recorded from all five samples are shown in Figure 4.3.20.

The unmilled sample, and that milled for 15 minutes showed absorption of hydrogen between *ca.* 300 and 400 °C. Absorption of hydrogen at a similar temperature was observed when Co_3O_4 and CoO were examined by temperature programme reduction (Figure 4.3.18). It therefore seems that calcination at 1250 °C, of the unmilled mixture and that milled for 15 minutes does not result in all of the reactant cobalt oxide being converted to cobalt aluminate. The results recorded by temperature programme reduction from the other samples that were milled for longer periods of time prior to calcination at 1250 °C for 30 minutes, failed to show any evidence for the presence of un-reacted cobalt oxides. These results suggest that pre-milling the mixture of Co_3O_4 and γ-$Al(OH)_3$ for periods of time exceeding 30 minutes, promotes at least a more intimate mixing of reactants, which leads on subsequent calcination, to complete conversion of the reactants under the calcination conditions used here.

Peaks in the temperature programme reduction profiles with a maxima *ca.* 1000 °C and a shoulder *ca.* 850-950 °C, are probably caused by precursors to $CoAl_2O_4$ and possibly due to Co_2AlO_4. These peaks were evident in the profiles recorded from the sample that had not been pre-milled and from that pre-milled for 15 minutes. Similar features were also evident as a slight shoulder in the temperature programme reduction profiles recorded from samples pre-milled for 30 minutes and 1 hour. However, the features at *ca.*

1000 °C and at *ca.* 850-950 °C were absent from the temperature programme reduction profile recorded from the sample milled for 5 hours. The results suggest that calcination is able to achieve a greater extent of reaction between the cobalt- and aluminium-containing species when the mixture has been pre-milled for 5 hours. Peaks at *ca.* 1100 °C, were evident in the temperature programme reduction profiles recorded from all samples, and there was a trend to increased intensity in the peak at 1100 °C as pre-milling periods increased.

Figure 4.3.19 shows the colours of the materials produced after heating the mixture to 1250 °C for 30 minutes. This demonstrates that the colour of the samples ranged from dark, dull blue/green for the sample which had not been milled prior to calcination, to the bright intense blue colour associated with $CoAl_2O_4$ for the sample pre-milled for 5 hours prior to calcination at 1250 °C. It seems reasonable to conclude that $CoAl_2O_4$ is the cause of the peak in the temperature programme reduction profile at 1100 °C.

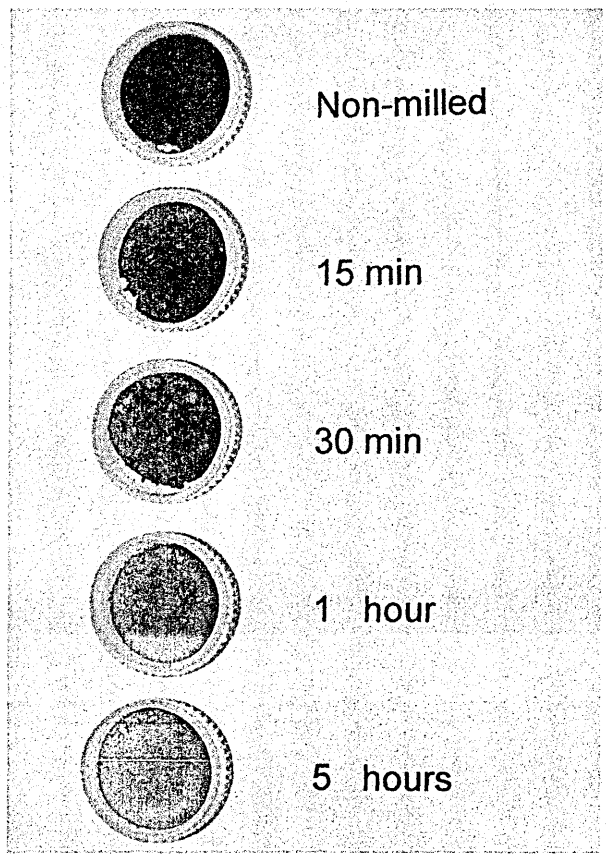

Figure 4.3.19 Photograph of the materials produced after heating at 1250 °C for 30 minutes (the times indicate the length of pre-milling prior to calcination).

The greater intensity of the two peaks at higher temperatures in the temperature programme reduction profiles suggest that the extent of $CoAl_2O_4$ formation after heating at 1250 °C is greater in materials subjected to longer pre-milling times. Presumably this is due to greater intimacy of reactant particles, achieved during the milling process. These results are consistent with the visual examination of the samples (Figure 4.3.19), which showed a poor, dull colour for the partially reacted samples containing residual CoO and Co_3O_4, and bright, intense colours for those that were fully reacted to form $CoAl_2O_4$.

A further experiment was performed where the temperature at which the materials were heated prior to examination by temperature programmed

reduction was reduced from 1250 °C to 1050 °C. Temperature programme reduction profiles recorded from pre-milled samples that were subsequently heated at 1050 °C for 30 minutes are shown in Figure 4.3.21. These profiles show reduction processes that occur below 450 °C and are associated with the presence of cobalt oxide (CoO and Co_3O_4) in all samples. The intensity of these peaks decreased with increasing milling time. The profiles also show the development of the absorption associated with $CoAl_2O_4$ at *ca.* 1100 °C and the corresponding reduction of the absorption between *ca.* 800-1000 °C that may be associated to precursors of $CoAl_2O_4$.

All the calcined samples were a dull blue/green colour without the distinctive intense blue colour associated with $CoAl_2O_4$ and close examination showed the presence of white grains in the non-milled sample (most likely α-Al_2O_3).

Taken together the temperature programme reduction results endorse the notion that pre-milling acts to promote the formation of $CoAl_2O_4$ during subsequent high temperature calcination by increasing the intimacy of mixing between Co_3O_4 and γ-$Al(OH)_3$ reactants.

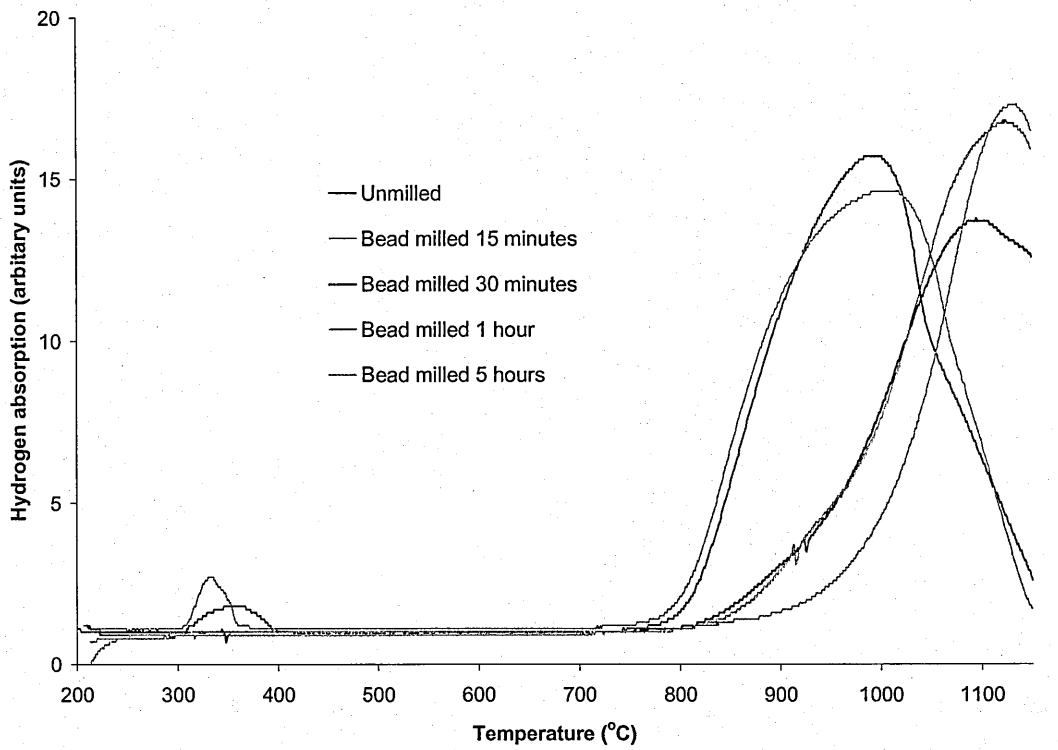

Figure 4.3.20. Temperature programme reduction profiles recorded from a mixture of M1275 (Co_3O_4) and MO150 (γ-$Al(OH)_3$) bead milled for up to 5 hours and subsequently heated in air at 1250 °C for 30 minutes.

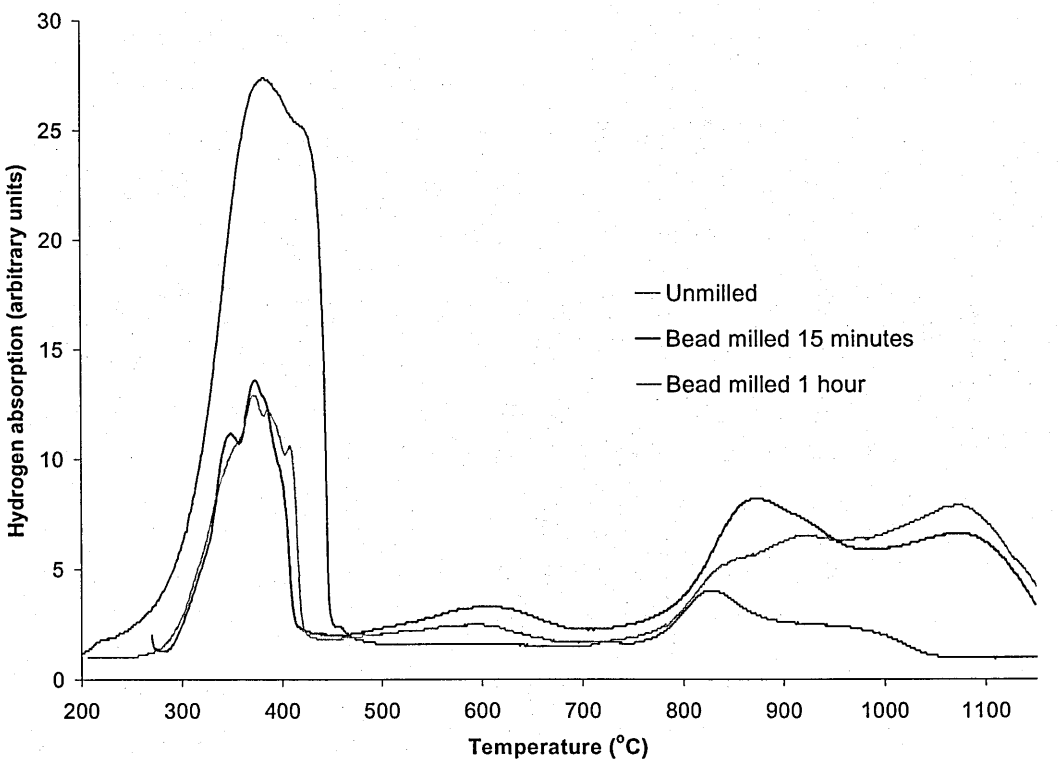

Figure 4.3.21. Temperature programme reduction profiles recorded from a mixture of M1275 (Co_3O_4) and MO150 (γ-$Al(OH)_3$) bead milled for up to 1 hour and subsequently heated in air at 1050 °C for 30 minutes.

4.3.4 Effect of bead milling on mixtures of M1275 (Co_3O_4) and SF11E (γ-$Al(OH)_3$)

Scanning electron micrographs recorded from a 1 mol : 6 mol mixture of M1275 and SF11E, bead milled for up to 16 hours are shown in Figure 4.3.22 to Figure 4.3.24. The results confirm the small particle size of the γ-$Al(OH)_3$ (SF11E) as previously described in section 4.3.2. Due to the smaller primary particle size, the intimacy of mixing between M1275 with SF11E was far greater after 1 hour of bead milling (Figure 4.3.23) than between MO150 (also γ-$Al(OH)_3$) with M1275 after 1 hour of bead milling (Figure 4.3.14).

There was no discernible difference between the scanning electron micrographs of the material milled for 1 hour and 5 hours (Figure 4.3.24) suggesting that the two components were randomly distributed after 1 hour and that the particle size was not being significantly reduced.

The temperature programme reduction profiles recorded from the materials bead milled for 1 hour and 5 hours and subsequently heated in air at 1250 °C for 30 minutes, are shown in Figure 4.3.25. These showed sharp peaks at *ca.* 1100 °C associated with the reduction of $CoAl_2O_4$. The absence of hydrogen absorption at lower temperatures demonstrates that the reaction between pre-milled M1275 (Co_3O_4) and SF11E (γ-$Al(OH)_3$) to form $CoAl_2O_4$ reaches completion after 30 minutes.

These results contrast with those recorded from similar mixtures produced using the larger particle sized γ-$Al(OH)_3$ (MO150) which did not react fully (Section 4.3.3). Visual inspection showed a greater intensity of the blue colour associated with $CoAl_2O_4$ for samples prepared from SF11E than for the comparable samples prepared using the MO150 form of γ-$Al(OH)_3$.

The results would also imply that particle size reduction by milling MO150 (γ-$Al(OH)_3$) in the presence of M1275 (Co_3O_4), appears to be inefficient compared to milling MO150 separately and suggests that the small particles of Co_3O_4 (M1275) cushion and thus hinder the milling process. Once the particle size of γ-$Al(OH)_3$ is reduced as demonstrated here by the use of SF11E rather than MO150, then the milling process acts to increase the intimacy and thus proximity of the components such that the subsequent calcination reaction proceeds in a more facile fashion.

Figure 4.3.22. Scanning electron micrograph from a mixture of M1275 and SF11E (x900).

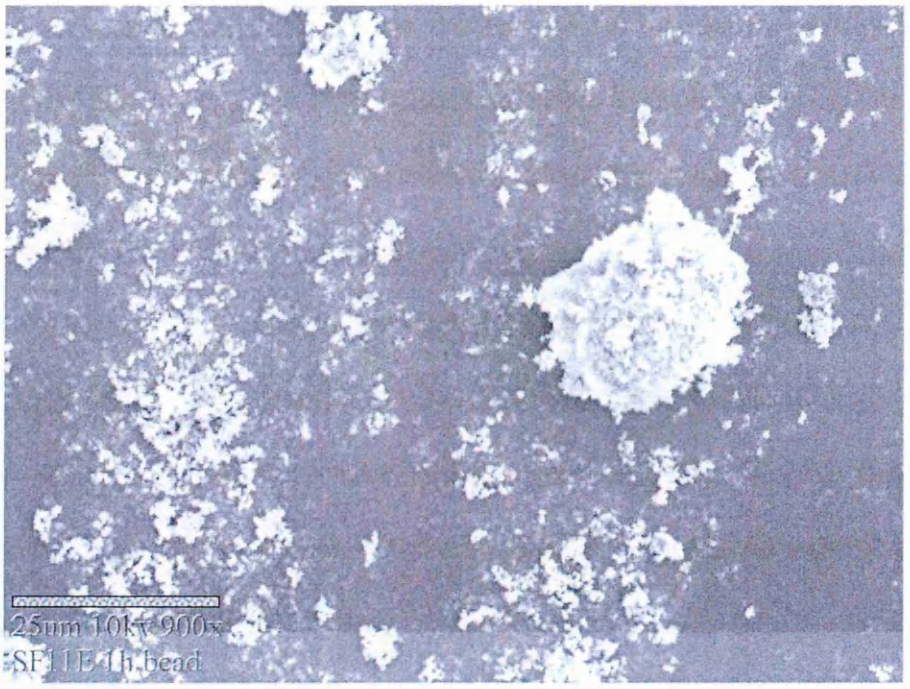

Figure 4.3.23. Scanning electron micrograph of M1275 (Co_3O_4) and SF11E (γ-$Al(OH)_3$), bead milled 1 hour, (x900).

Figure 4.3.24. Scanning electron micrograph of M1275 (Co_3O_4) and SF11E (γ-$Al(OH)_3$, bead milled 5 hours, (x900).

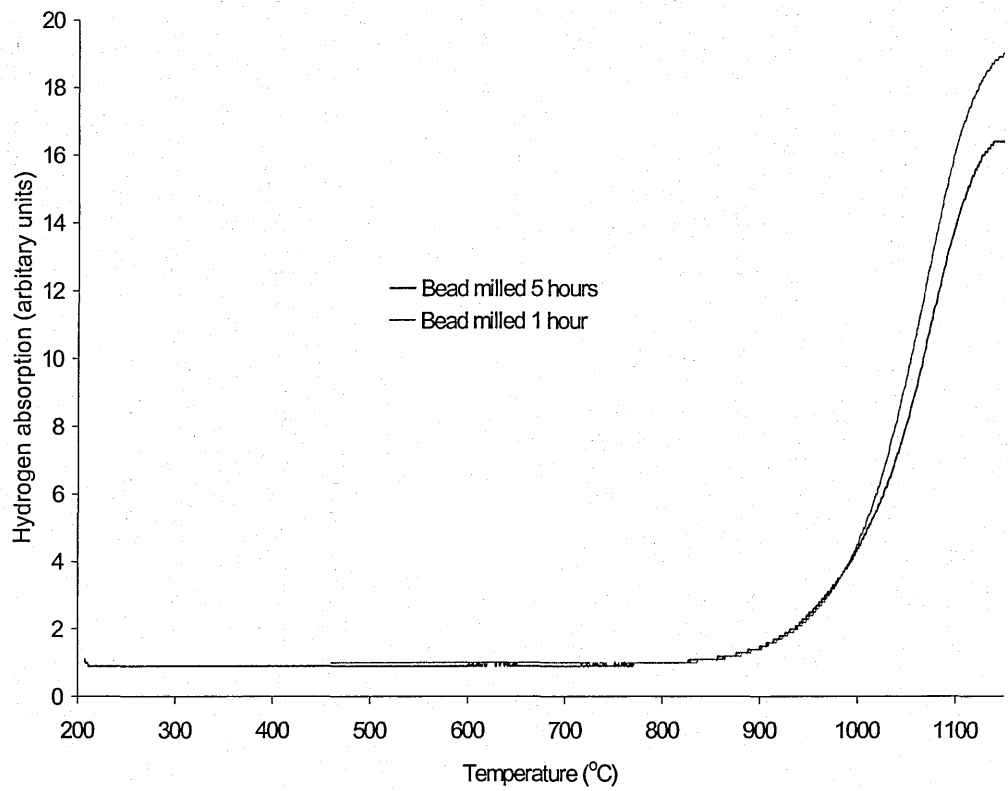

Figure 4.3.25. Temperature programme reduction profiles recorded from a mixture M1275 (Co_3O_4) and SF11E (γ-$Al(OH)_3$ following pre-bead milling for 1 hour and 5 hours and subsequently heated in air at 1250 °C for 30 minutes.

In summary, the work reported in Section 4.3 shows that;

- M1275 (Co_3O_4) particles are less than 0.1 μm diameter and form agglomerates less than 5 μm diameter.
- Bead milling does not significantly alter the primary particle size of M1275 (Co_3O_4).
- Bead milling significantly reduces the particle size of MO150 (γ-$Al(OH)_3$).
- The SF11E form of γ-$Al(OH)_3$ has a significantly smaller particle size (< 1 μm) than the MO150 form of γ-$Al(OH)_3$ (25-100 μm).
- Bead milling has little effect on the final particle size of SF11E (γ-$Al(OH)_3$).

- Bead milling acts to increase the proximity of reactant particles.
- Bead milling does not significantly reduce the primary particle size of reactant components in a mixture.
- The effectiveness of bead milling to increase the intimacy of mixing and subsequent efficiency of the calcination reaction is limited in cases where one of the components is significantly larger than the other.
- Increased intimacy of mixing reduces the time required for reagents to fully react forming $CoAl_2O_4$, hence M1275 (Co_3O_4) reacts more readily with SF11E (γ-$Al(OH)_3$) than with MO150 (γ-$Al(OH)_3$).
- Examination of cobalt aluminate formed from bead milled mixtures calcined at 1050 °C for 30 minutes, by temperature programme reduction shows peaks that are likely to be precursors of $CoAl_2O_4$ at *ca.* 800 to *ca.* 1000 °C
- The temperature programme reduction profiles also show a peak due to $CoAl_2O_4$ at *ca.* 1100 °C
- A single peak in the temperature programme reduction profile at *ca.* 1100 °C indicates that the reaction to form $CoAl_2O_4$ is complete.
- The observation of temperature programme reduction peaks below *ca.* 400 °C indicates that unreacted CoO and/or Co_3O_4 are present.
- Fully reacted $CoAl_2O_4$ products show a distinctive bright and intense blue colour.
- $CoAl_2O_4$ products containing unreacted phases are dull blue/green.

4.4 Effect of cobalt : aluminium ratio on products formed from M1275 (Co_3O_4) and Baco MA95 (α-Al_2O_3)

Samples were prepared from M1275 (Co_3O_4) and Baco MA95 (α-Al_2O_3) mixed in specific proportions to produce $Co_xAl_{(3-x)}O_4$ where, x=2.8 to x=1.0, bead milled for 1 hour as described in Section 3.1.1, and subsequently heated at 1400 °C for 90 hours.

X-ray powder diffraction patterns recorded from each of the samples are shown in Figure 4.4.1. and the crystalline phases identified from each X-ray powder diffraction pattern are summarised in Table 4.4.1.

x	CoO	Co_3O_4	$CoAl_2O_4$
2.8	√	√	
2.4	√	√	
2.2	√	√	√
2.0	√	√	√
1.8	√	√	√
1.6	√	√	√
1.5	√	√	√
1.4	√	√	√
1.2	√	√	√
1.1			√
1.0			√

Table 4.4.1. Summary of the crystalline phases identified by X-ray powder diffraction of mixtures of M1275 (Co_3O_4) and Baco MA95 (α-Al_2O_3) after heating to 1400 °C for 90 hours.

The X-ray powder diffraction patterns show, within the limits of detection, that there were no reflections that matched those reported in the literature characteristic of α-Al_2O_3[75] in any of the products. Reflections matching those reported in the literature for CoO[78] were present in products where $2 > x \geq 1.2$, i.e. where the amount of Co_3O_4 reagent in the starting mixture exceeded that required to form stoichiometric $CoAl_2O_4$. If the material of composition Co_2AlO_4 were formed, then the CoO detected in the products by X-ray powder diffraction would not be expected to be present and suggests that Co_2AlO_4 is not formed under these conditions.

It is noticeable that the intensity of reflections at *ca.* 49 $^{o}2\theta$, characteristic of $CoAl_2O_4$ increased as x tended towards 1.

A number of other observations could be made. The cobalt rich samples ($x > 2.2$) significantly decreased in volume during heating to approximately one quarter of the original volume without significant mass loss, other than that expected due to the structural rearrangement of spinel-related Co_3O_4 to form CoO and the corresponding loss of oxygen. These samples sintered and formed a single hard lump, in contrast to the crumbling products that were formed from materials where $x < 2.2$. This effect became progressively marked as the value of x increased to 2.8. This observation suggests that during the reaction between cobalt oxides and aluminium oxides at *ca.* 1400 ^{o}C, the cobalt oxide is more likely than aluminium oxide to be the mobile phase since it appears capable of migrating at these temperatures over a distance that exceeds the diameter of the individual particles.

X-ray powder diffraction patterns of similar samples quenched from the furnace at 1400 °C into water at 20 °C are shown in Figure 4.4.2. A summary of the phases identified from each X-ray powder diffraction pattern is shown in Table 4.4.2. These did not show any significant variation in composition from the products that were not quenched, other than the absence of Co_3O_4 after cooling due to the rapid temperature change.

These results show that, even upon rapid quenching from 1400 °C to 20 °C in less than 2 seconds, CoO and α-Al_2O_3 are not miscible across the range of compositions represented by the formula $Co_xAl_{(3-x)}O_4$ and where x = 1.0 to x = 2.8.

In summary, the work reported in Section 4.4. shows that, under the conditions of milling and calcination reported here, the continuous solid solution series in the system $Co_xAl_{(3-x)}O_4$ as suggested by Rasines and Garcia[79] was not identified.

X	CoO	$CoAl_2O_4$
1.6	√	√
1.5	√	√
1.4	√	√
1.2	√	√
1.1		√
1.0		√

Table 4.4.2. . Summary of the crystalline phases identified by X-ray powder diffraction from mixtures of M1275 (Co_3O_4) and Baco MA95 (α-Al_2O_3) with empirical formulae $Co_xAl_{(3-x)}O_4$ where x=1.6 to x=1.0 after quenching from 1400 °C.

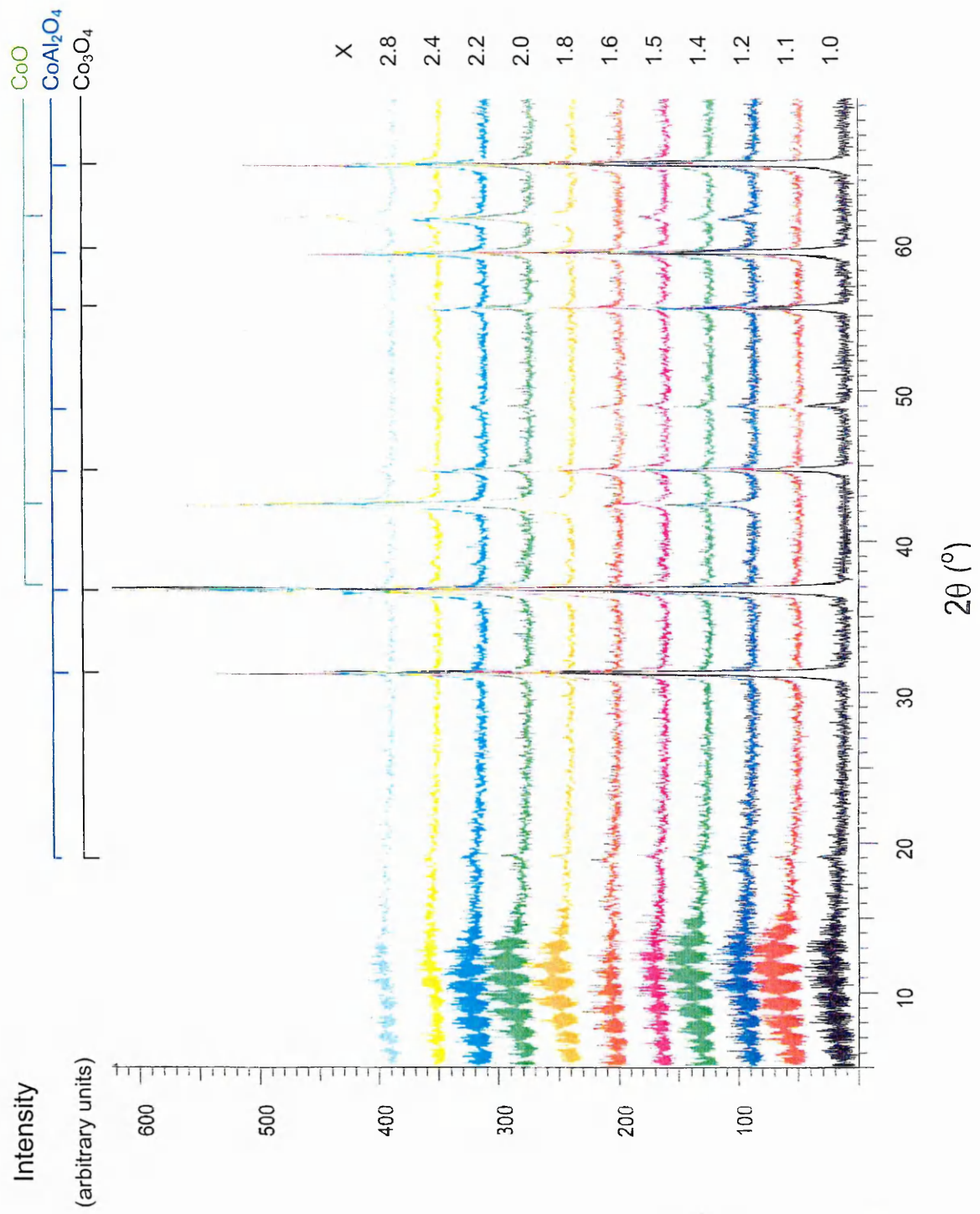

Figure 4.4.1. X-ray powder diffraction patterns recorded from mixtures of M1275 (Co_3O_4) and Baco MA95 (α-Al_2O_3) with empirical formulae $Co_xAl_{(3-x)}O_4$ where x=2.8 to x=1.0 heated to 1400 °C for 90 hours.

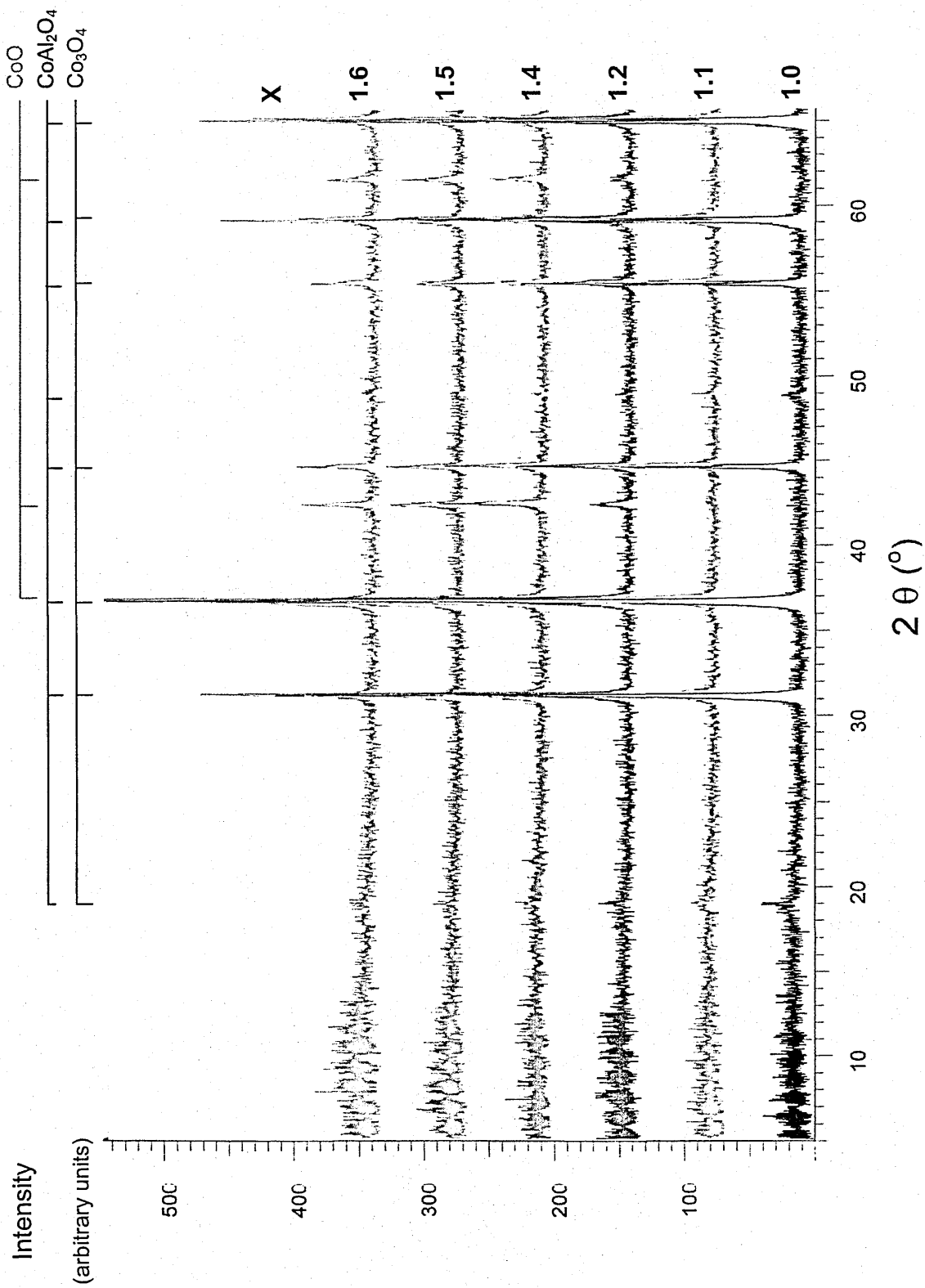

Figure 4.4.2. X-ray powder diffraction patterns recorded from mixtures of M1275 (Co_3O_4) and Baco MA95 (α-Al_2O_3) with empirical formulae $Co_xAl_{(3-x)}O_4$ where x=1.6 to x=1.0 heated to 1400 °C for 90 hours then quenched to 20 °C.

4.5 Conclusions

- The thermally induced phase changes resulting from the heating of Co_3O_4 and γ-$Al(OH)_3$ in air have been characterised.
- The formation of cobalt aluminate of composition $CoAl_2O_4$ from γ-$Al(OH)_3$ and Co_3O_4 is shown at temperatures exceeding 1000 ^oC and that more than one mechanism may contribute to the reaction pathway.
- The pre-milling of Co_3O_4 and γ-$Al(OH)_3$ prior to calcination, influences the reaction pathway to the formation of cobalt aluminate.
- Under the conditions used in this work, the continuous solid solution series in the system $Co_xAl_{(3-x)}O_4$ reported previously[79] cannot be identified.

Chapter 5

Formation of Perovskite-Related Structures and Structural Rearrangements Induced by Mechanical Milling

Results and Discussion

5.1 Formation of perovskite-related structures of the type $CaMO_3$ (M = Sn, Ti) by mechanical milling

5.1.1 Calcium stannate

Calcium stannate, $CaSnO_3$, was prepared by dry milling a stoichiometric mixture of calcium (II) oxide, CaO, and tin (IV) oxide, SnO_2, in air, using ten stainless steel balls and a stainless steel vial for periods of time up to 116 hours. The X-ray powder diffraction patterns recorded from these materials are shown in Figure 5.1.1. The pattern recorded from the material after 1 hour of milling showed reflections that coincided with those reported in the literature for CaO[80] and SnO_2[81]. The appearance after 22 hours of milling of reflections at *ca.* 22 and *ca.* 46 °2θ are characteristic of $CaSnO_3$[82]. As mechanical milling progressed, the intensity of these reflections also increased. The patterns also showed a corresponding decrease in intensity of those reflections associated with CaO (*ca.* 54 °2θ) and SnO_2 (*ca.* 26.7 °2θ).

The full width at half maximum (FWHM) of the peak at *ca.* 22 °2θ, which is characteristic of $CaSnO_3$ in the material milled for 22 hours was broad, *ca.* 0.49 °2θ and suggested that the calcium stannate formed in the mill after about one day was poorly crystalline. After 116 hours of milling the peak width, *ca.* 0.36 °2θ, was significantly narrower suggesting that the material became increasingly crystalline with the longer period of milling.

Overlapping reflections in the X-ray powder diffraction patterns precluded the determination of crystallite size from the powder diffraction data, however, transmission electron microscopy, (Figure 5.1.3),

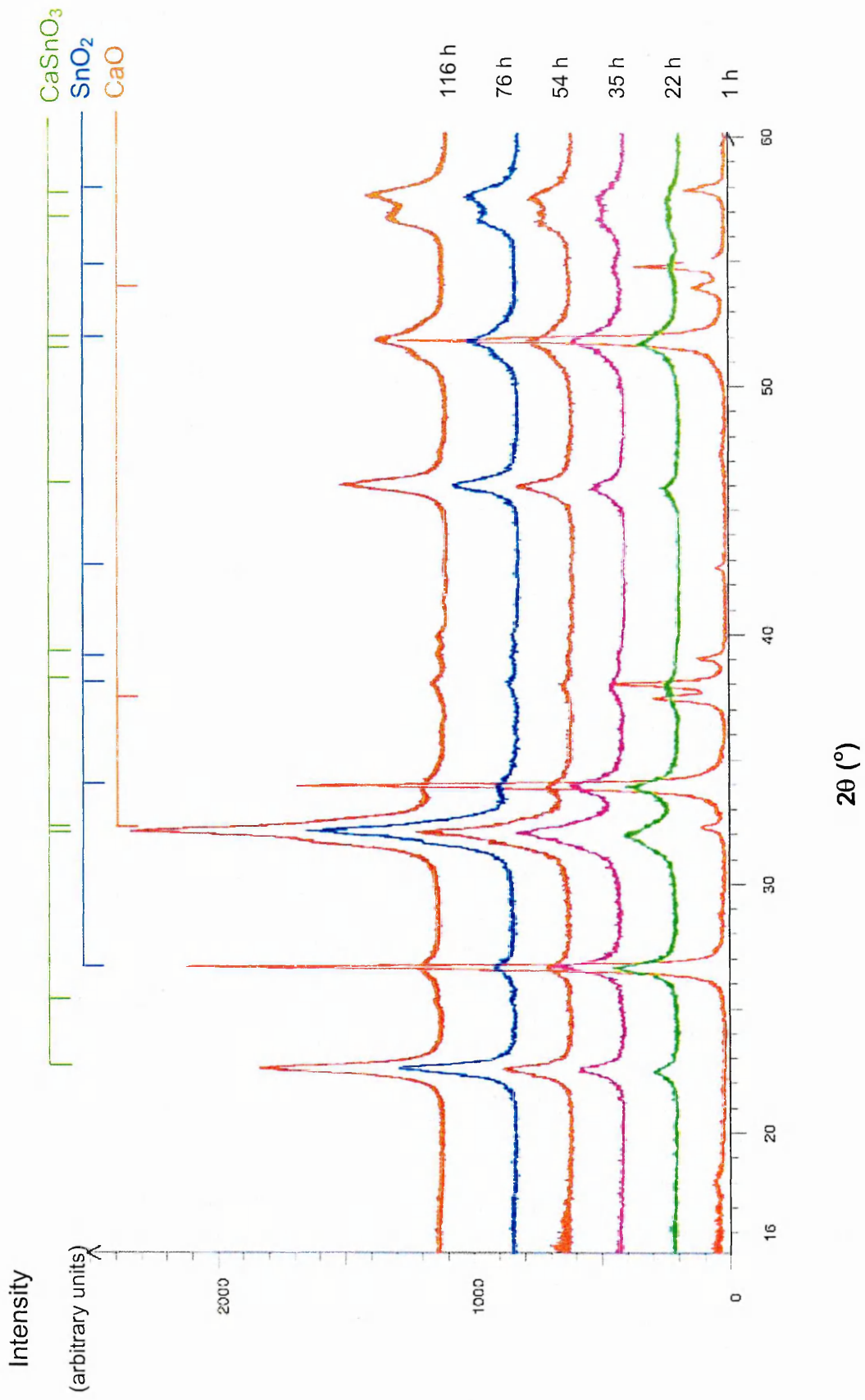

Figure 5.1.1 - X-ray powder diffraction patterns showing the transformation of a mixture of CaO and SnO_2 to $CaSnO_3$ as a function of milling time.

showed that the particle size of $CaSnO_3$ formed by ball milling for 116 hours to be less than 25 nm. This size was smaller than that determined by transmission electron microscopy of calcium stannate prepared by calcination of CaO and SnO_2 at 1400 $^{\circ}C$ for 5 days which was of the order of *ca.* 1 μm diameter (Figure 5.1.4). The products from the reactant mixture after 116 hours of milling also showed the presence of some unreacted calcium oxide and tin dioxide demonstrating that the reaction had not gone to completion.

Hence the X-ray powder diffraction data showed that mechanical milling induced a reaction between rock-salt-related calcium oxide and rutile-related tin dioxide to form perovskite-related calcium stannate of smaller particle size than that achieved by conventional calcination of the reactant oxides at elevated temperatures.

The ^{119}Sn Mössbauer spectra recorded from samples removed after 1, 22 and 116 hours of milling of the mixture of CaO and SnO_2 are shown in Figure 5.1.2.

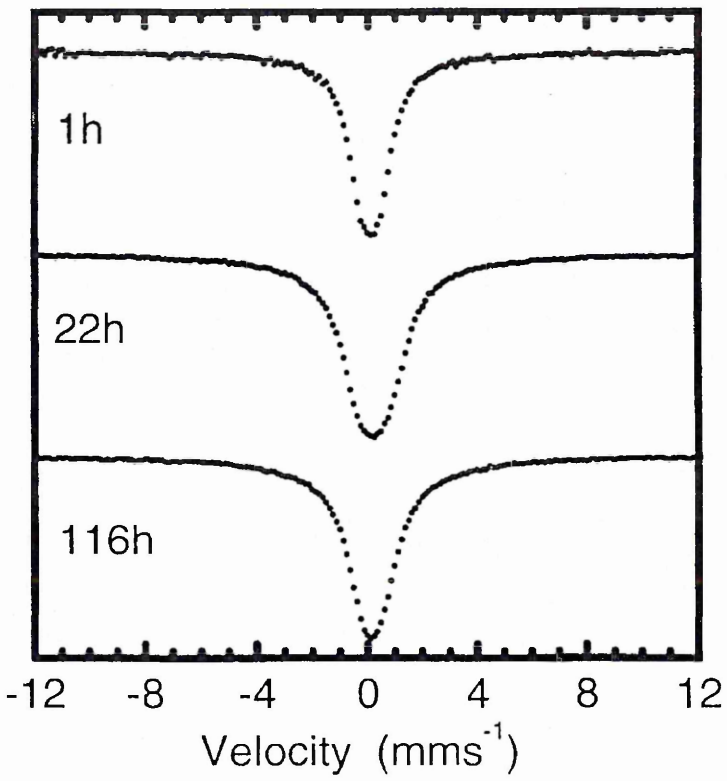

Figure 5.1.2 - ^{119}Sn Mössbauer spectra recorded from a mixture of CaO and SnO_2 ball milled for 1, 22 and 116 hours.

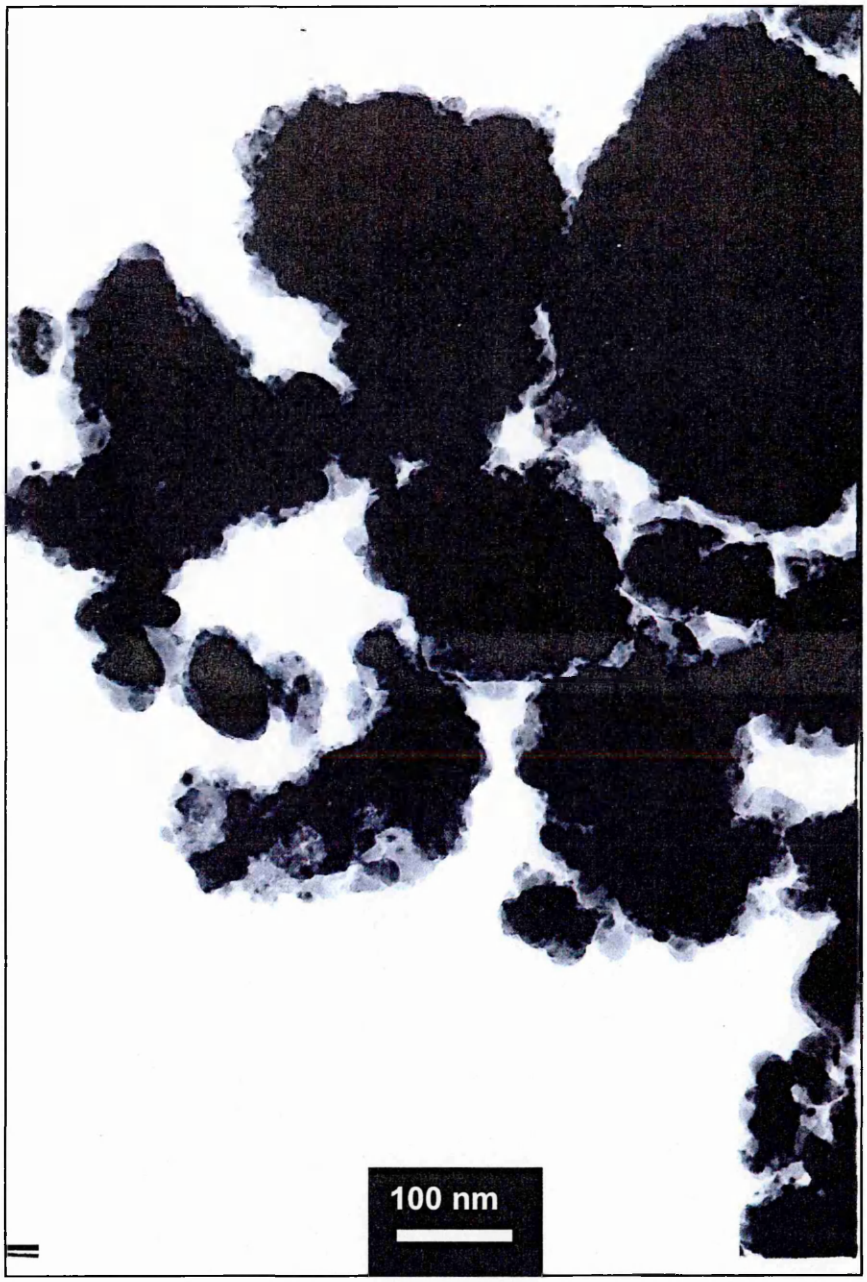

Figure 5.1.3 Transmission electron micrograph of $CaSnO_3$ formed from a mixture of CaO and SnO_2 ball milled for 116 hours (x80K).

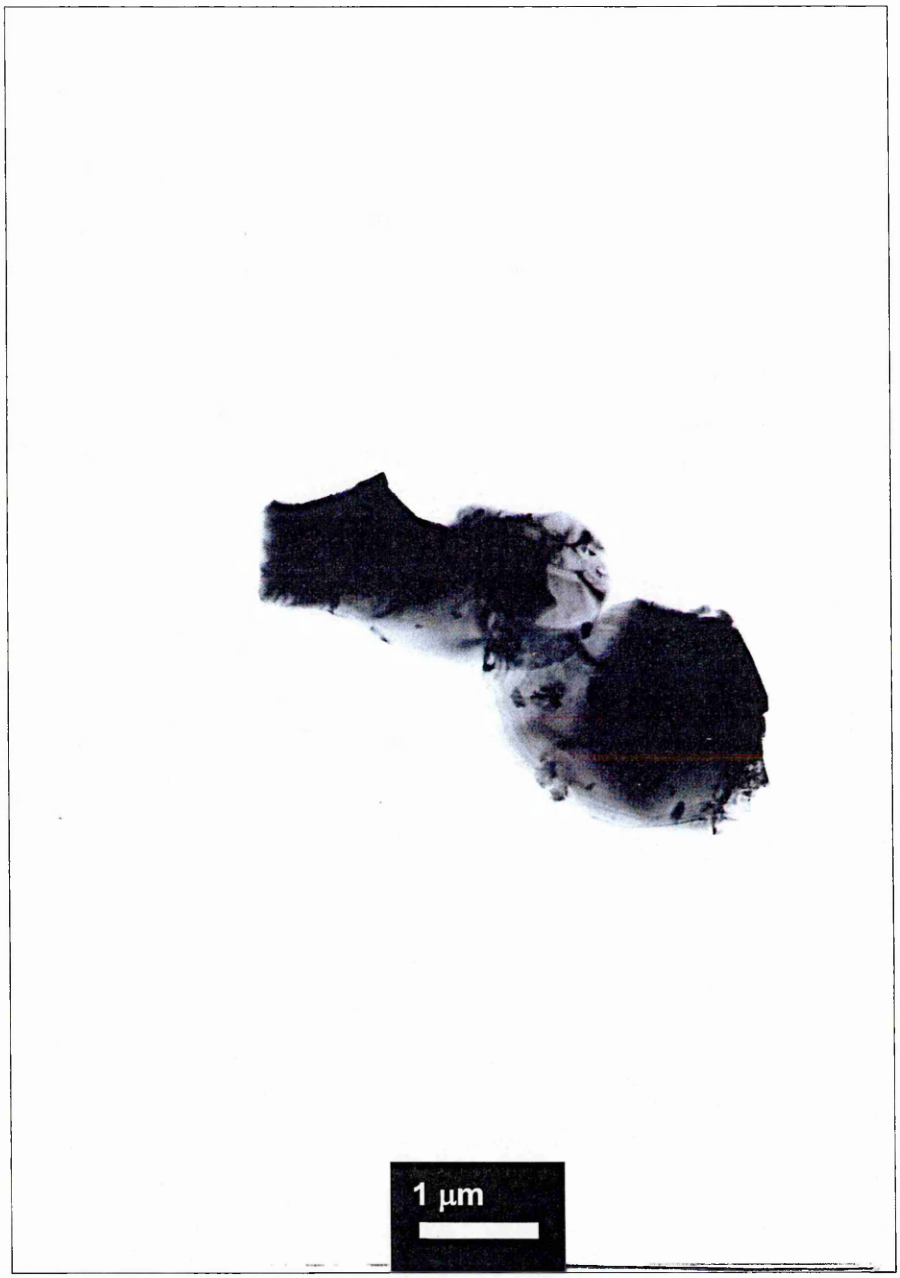

Figure 5.1.4 Transmission electron micrograph of $CaSnO_3$ formed by calcination at 1400 °C for 5 days (x8000).

The line widths of materials milled for 1 hour, 22 hours and 116 hours are shown in Table 5.1.1. The data showed that the material milled for 22 hours produced a ^{119}Sn Mössbauer spectrum with a broader line width than materials that had been milled for either 1 hour or 116 hours. This is consistent with the transformation of a single tin-containing phase (SnO_2) to a mixture containing two tin-containing phases (SnO_2 and $CaSnO_3$) and then to $CaSnO_3$ where tin was predominantly present in a single site.

Milling time	Γ /mms^{-1}	Sn phases present.
1 hour	1.55(5)	SnO_2
22 hour	2.28(5)	SnO_2 + $CaSnO_3$
116 hour	1.92(5)	$CaSnO_3$

Table 5.1.1 - Line widths of ^{119}Sn Mössbauer spectra recorded from a milled mixture of CaO and SnO_2 as a function of milling time.

Taken together the results demonstrate that mechanical milling of the two structurally unrelated oxides, calcium oxide and tin dioxide, results in the formation of small particle calcium stannate with a perovskite-related structure on a time scale comparable to that of conventional calcination methods, which produce large particle calcium stannate.

5.1.2 Calcium titanate

The phases formed during the milling of a mixture of calcium (II) oxide and the anatase modification of titanium (IV) oxide as a function of milling time were deduced from the X-ray powder diffraction patterns shown in Figure 5.1.5. Calcium hydroxide was present in the calcium (II) oxide reagent and appeared to undergo only limited change in the ball mill, illustrated by the modest reduction in the $Ca(OH)_2$[83] reflections at *ca* 18 and 34 °2θ over 110 hours of milling. In contrast, the reflections corresponding to calcium (II) oxide decreased with milling, illustrated by the reflection at *ca.* 37 °2θ which disappeared from the X-ray powder diffraction pattern recorded after 110 h of milling. Reflections corresponding to anatase[84] at *ca.* 25 °2θ demonstrated a gradual decrease in intensity as the milling time increased although, from Figure 5.1.5, it is clear that some anatase remained unchanged after 110 hours of milling.

The disappearance of reflections corresponding to CaO and the decrease in intensity of reflections corresponding to anatase and $Ca(OH)_2$ with increasing milling time was accompanied by a concomitant increase in intensity of the reflection at *ca.* 33 °2θ, corresponding to $CaTiO_3$[85]. The results suggest that CaO reacted preferentially in the ball mill with the anatase form of TiO_2 to produce $CaTiO_3$.

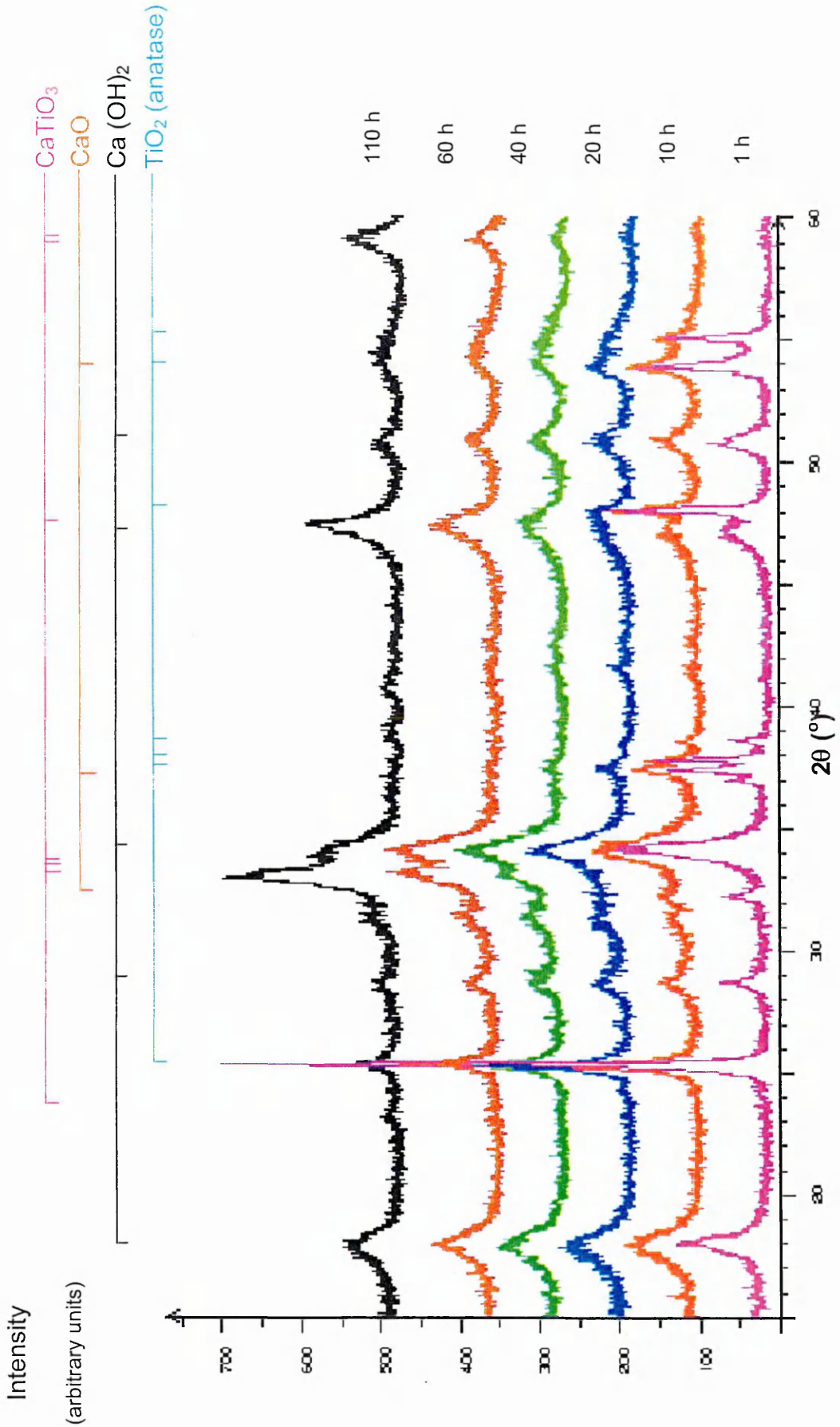

Figure 5.1.5 - X-ray powder diffraction patterns showing the transformation of a mixture of CaO and the anatase modification of TiO_2 to $CaTiO_3$ as a function of milling time.

It is interesting to note that the unreacted anatase did not undergo transformation to the rutile modification of titanium (IV) oxide, which is characterised[86] by a reflection at *ca.* 27.5 °2θ. This is somewhat surprising since X-ray powder diffraction patterns shown in Figure 5.1.6. recorded from pure anatase subjected to milling showed that, under similar conditions, the pure anatase modification of titanium (IV) oxide is converted to the rutile form after only 20 hours of milling. Recent reports[87] have shown that the kinetics of the phase transformation from anatase to rutile depends on the powder to ball weight ratio and the nature of the grinding media. The results reported here from experiments in which both of these parameters were unchanged suggest that the kinetics and mechanisms of the phase transformation are both complex and are influenced by the presence of other phases.

A striking difference in the formation of $CaTiO_3$ was observed when calcium (II) oxide (which also contained calcium hydroxide contamination) was milled with the rutile modification of titanium (IV) oxide. The X-ray powder diffraction patterns of samples removed after different periods of milling are shown in Figure 5.1.7. The reflections showed that the calcium hydroxide and calcium (II) oxide reacted with rutile to give monophasic $CaTiO_3$ after only 10 hours of milling. This demonstrates that the crystal modification of titanium dioxide has considerable influence on the ease by which $CaTiO_3$ can be made by milling TiO_2 and CaO and indicates that the rutile modification of TiO_2 undergoes a more facile reaction with CaO in the ball mill than the anatase polymorph of TiO_2. It is also clear that rutile reacts more readily in the mill with CaO than rutile-related SnO_2 (Section 5.1.1) showing that chemical composition plays an important role in governing the ease of chemical reactions in ball mills.

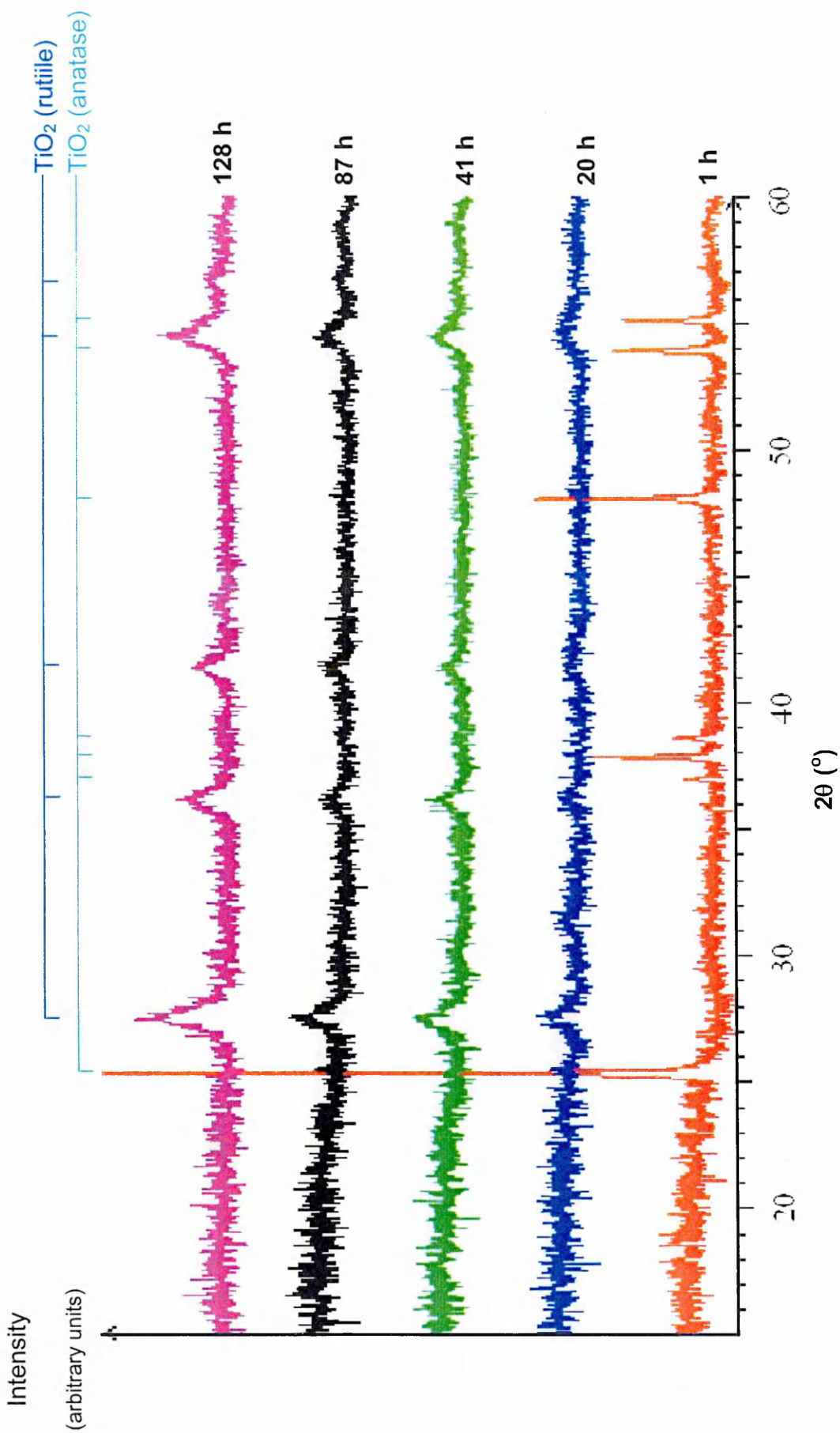

Figure 5.1.6 X-ray powder diffraction patterns showing the transformation of the anatase modification of TiO_2 to the rutile form as a function of mechanical milling time.

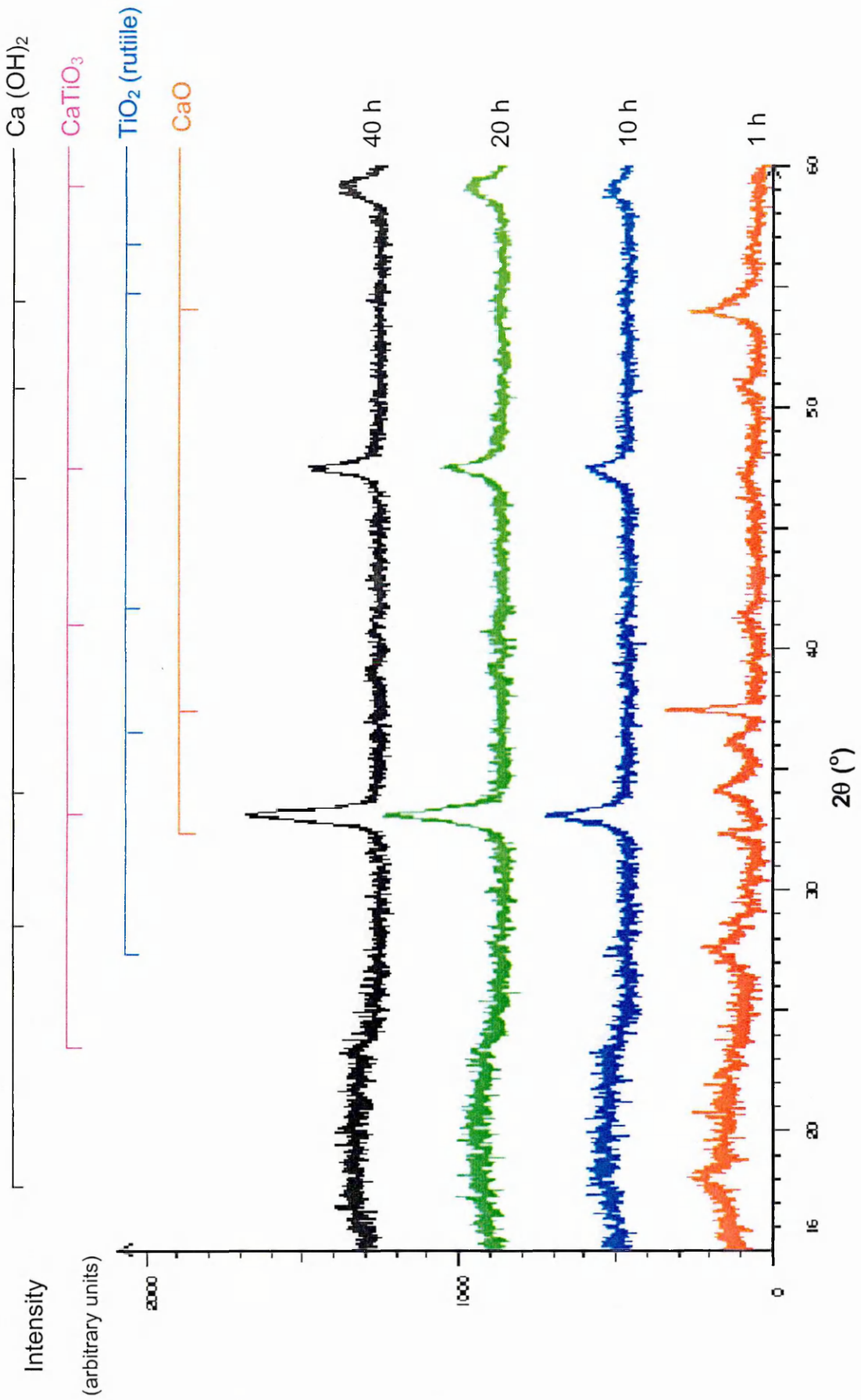

Figure 5.1.7 X-ray powder diffraction patterns showing the transformation of a mixture of CaO and the rutile modification of TiO_2 to $CaTiO_3$ as a function of mechanical milling time.

The results therefore demonstrate that the mechanical milling of CaO with SnO_2 and of CaO with either the anatase or rutile modifications of TiO_2 produces perovskite-related $CaMO_3$ (M= Sn/Ti) of smaller particle size than that prepared over comparable time scales by conventional calcination techniques. The enthalpy of formation for compounds of composition $CaMO_3$ (M = Sn/Ti) from the component oxides is large[88], for example it is -67.76 KJ mol^{-1} for $CaSnO_3$, and the temperatures required for preparation by solid-state methods are large. The results reported here suggest that ball milling enhances the inter-diffusion rates of the reaction mixture. It is also clear that the crystal structure of a reactant is important in governing the ease of reaction, hence the rutile form of TiO_2 undergoes more facile reaction with CaO in the ball mill than the anatase polymorph.

5.2 Rearrangement of the spinel-related $ZnFe_2O_4$ structure by mechanical milling

Polycrystalline $ZnFe_2O_4$ with a *normal* spinel-related structure was synthesised by the solid-state reaction of α-Fe_2O_3 and ZnO in stoichiometric quantities. This mixture was heated to 1400 $^{\circ}$C for 2 days and the single-phase nature of the material was confirmed[89] as $ZnFe_2O_4$ using X-ray powder diffraction (Figure 5.2.1).

X-ray powder diffraction patterns recorded from zinc ferrite which had been dry milled with 10 hardened stainless steel balls and vial for various periods of time, whilst pneumatically open to the atmosphere are shown in Figure 5.2.1. The reflections in the X-ray powder diffraction patterns coincided with those reported in the literature recorded from $ZnFe_2O_4$[89] and did not significantly

alter position throughout the experiment. Decomposition has been reported[90] to occur during thermal treatments of $ZnFe_2O_4$. The absence of reflections corresponding to zinc oxide and iron oxide demonstrate that milling under the conditions used here resulted in no decomposition of the zinc ferrite.

Scanning electron microscopy (SEM) with an energy dispersive X-ray (EDX) facility was used to determine the chromium content of the material. This corresponded to less than 1 wt. % contamination of the material from the stainless steel milling equipment after 50 hours of milling.

The ^{57}Fe Mössbauer spectra recorded at 295 K from samples of $ZnFe_2O_4$ milled for periods of between 10 minutes and 50 hours are shown in Figure 5.2.2. The spectra recorded from the material milled for 10 minutes were fitted to a narrow line (Γ=0.35(1) mm s^{-1}) quadrupole split absorption (Δ=0.40(2) mm s^{-1}) corresponding to high spin Fe^{3+} in an oxygen environment. The spectra recorded from materials subjected to longer periods of milling showed a broadening of line width (Γ=0.72(1) mm s^{-1}) for the material milled for 50 hours.

The spectra were amenable to fitting using a model in which a quadrupole split absorption was superimposed upon a magnetic hyperfine split absorption. Figure 5.2.3 shows the corresponding reduction of the quadrupole split component as a proportion of the total resonance area.

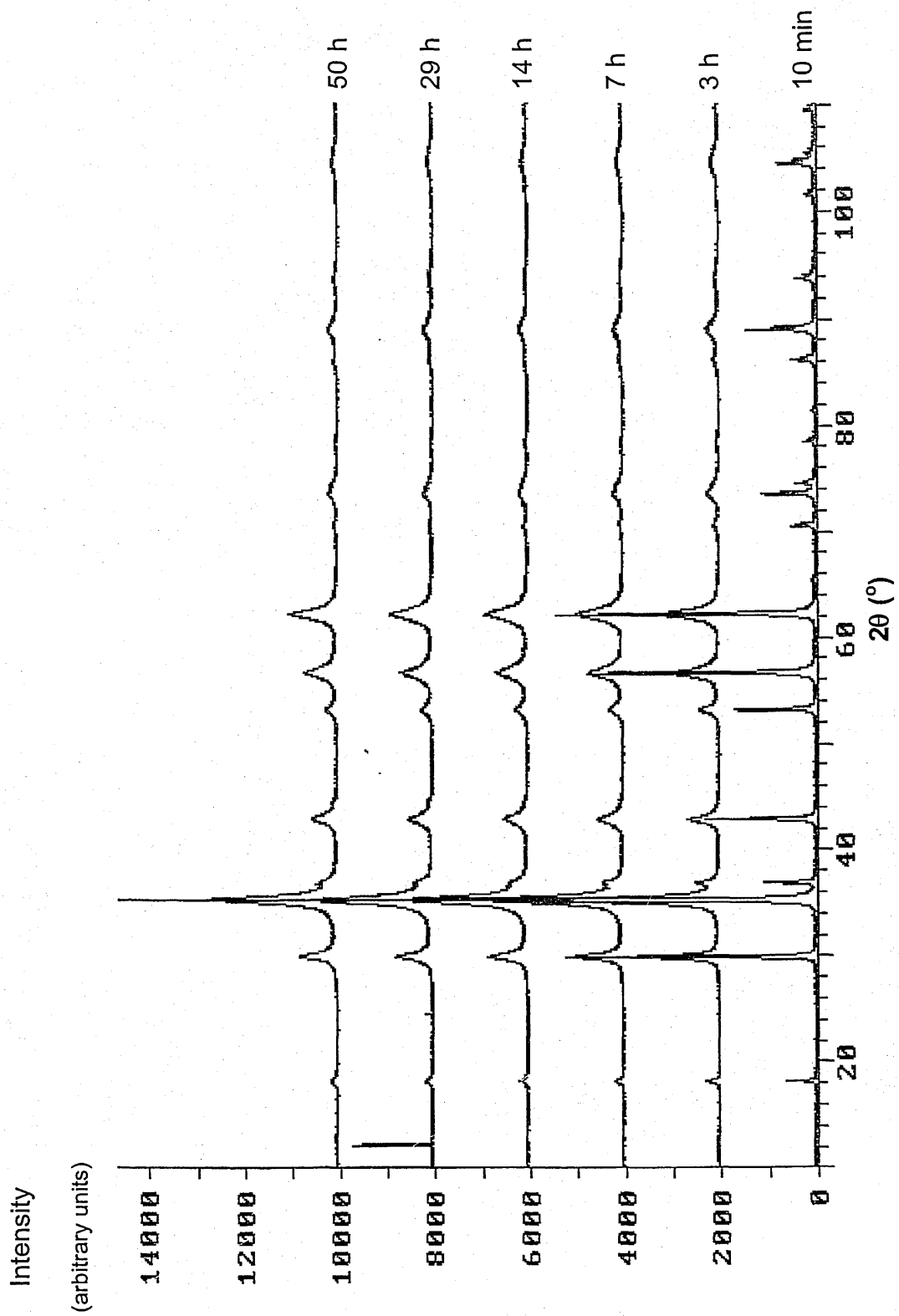

Figure 5.2.1 - X-ray powder diffraction patterns recorded from $ZnFe_2O_4$ following milling for periods of time between 10 minutes and 50 hours.

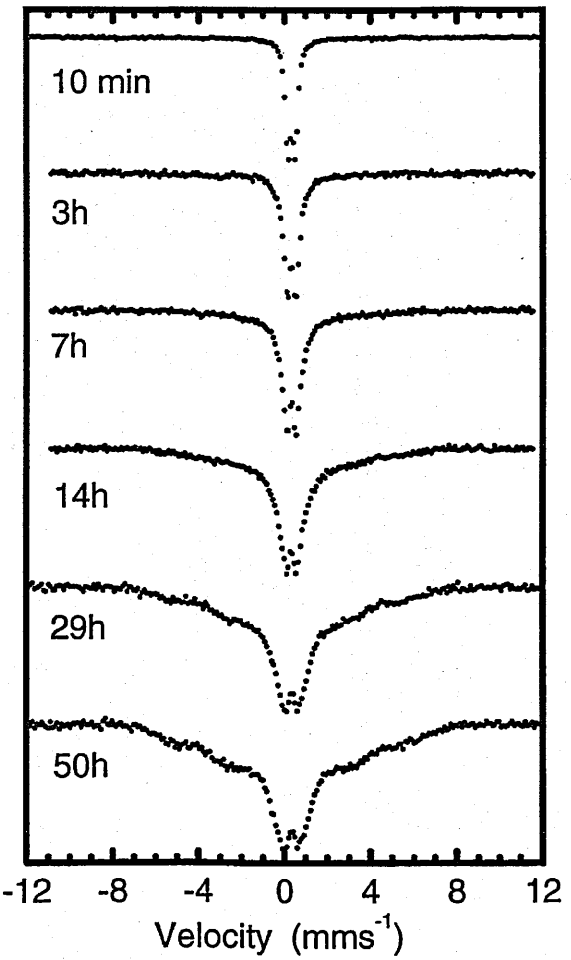

Figure 5.2.2 – ^{57}Fe Mössbauer spectra recorded at 295K from samples of $ZnFe_2O_4$ milled for periods of time between 10 minutes and 50 hours.

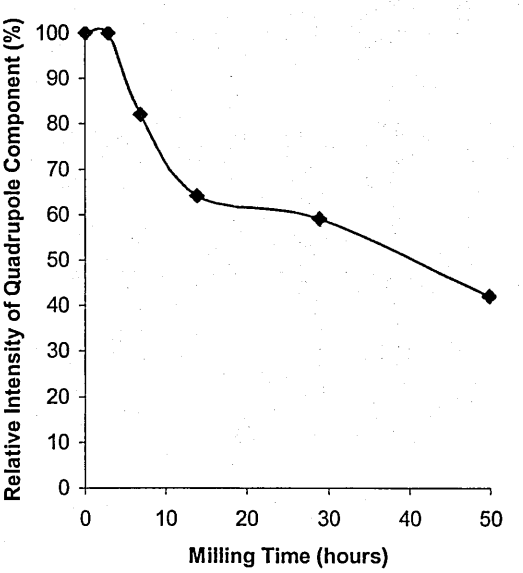

Figure 5.2.3 - Decrease in intensity of quadrupole split component in ^{57}Fe Mössbauer spectra recorded from $ZnFe_2O_4$ at 295 K as a function of milling time.

Normal spinel-related zinc ferrite is antiferromagnetic with a Néel temperature of ca. 10 K. The observation of magnetic order in the ^{57}Fe Mössbauer spectra recorded at 295 K is consistent with a ferro- or a ferri-magnetically ordered structure and suggests mechanical milling causes a movement of Fe^{3+} ions from the octahedral oxygen co-ordinated sites into tetrahedral sites. *i.e.* partial inversion of the structure.

The inducement of magnetic order in zinc ferrite as a result of mechanical milling was more pronounced in the Mössbauer spectra recorded from the materials at 80 K, which are shown in Figure 5.2.4. These spectra showed evidence of a magnetic hyperfine sextet after only 3 hours of milling and no evidence of the quadrupole split component in the Mössbauer spectra could be detected after 50 hours of milling.

The variation of intensity of the quadrupole split component in the Mössbauer spectra recorded at 80K as a function of milling time is shown in Figure 5.2.5.

The ^{57}Fe Mössbauer spectra recorded from the milled material at 15 K are shown in Figure 5.2.6. Here the onset of magnetic order due to mechanical milling caused features that were even more apparent and a degree of magnetic splitting was visible after just 10 minutes of milling. The lines characteristic of the magnetically split component became sharper and the intensity of the quadrupole split component decreased dramatically with increased milling time. After 14 hours of ball milling, almost no quadrupole component was detectable. The relative intensity of the quadrupole component as a function of milling time is shown in Figure 5.2.7. Since the Néel temperature occurs at *ca.* 10 K for *normal* spinel-related $ZnFe_2O_4$ the

results suggest that mechanical action alters the magnetic structure of the material.

In order to characterise the magnetic properties of the mechanically milled zinc ferrite further, ^{57}Fe Mössbauer spectra of the material ball milled for 50 hours were also recorded in a magnetic field of 0.7 Tesla applied perpendicular to the γ-ray direction at both 295 K and 80 K. These spectra are shown in Figure 5.2.8.

The spectra recorded at 295 K showed an enhancement of the magnetically split component in the presence of an applied field. The spectra recorded at 80 K were more informative, showing an enhancement of the 2^{nd} and 5^{th} lines of the sextet when a magnetic field was applied. This corresponds to the alignment of magnetic moments with the applied field and demonstrates that the material ball milled for 50 hours is ferrimagnetic or ferromagnetic and not antiferromagnetic as is characteristic of normal spinel-related $ZnFe_2O_4$.

In summary the results demonstrate an inversion of the spinel-related $ZnFe_2O_4$ structure as a result of mechanical action with a concurrent change in magnetic properties.

The results imply that mechanical milling induces a movement of Fe^{3+} ions from octahedral sites to tetrahedral sites and of Zn^{2+} ions from tetrahedral sites to octahedral sites.

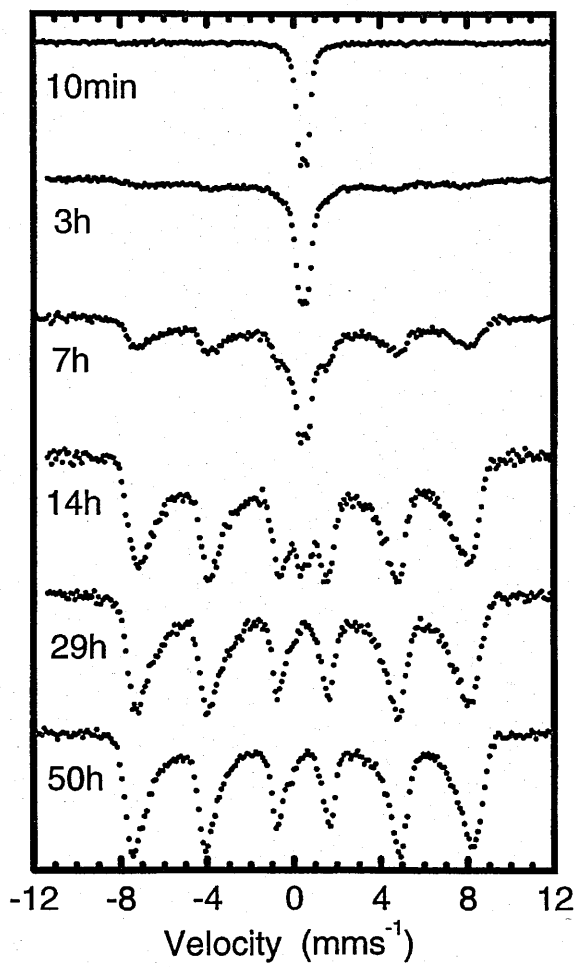

Figure 5.2.4 ^{57}Fe Mössbauer spectra recorded at 80K from samples of $ZnFe_2O_4$ milled for periods of between 10 minutes and 50 hours.

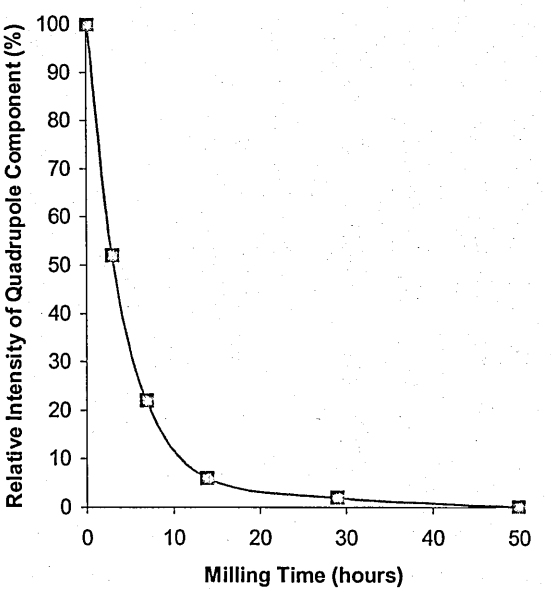

Figure 5.2.5 - Variation of intensity of quadrupole split component in the ^{57}Fe Mössbauer spectra recorded from $ZnFe_2O_4$ at 80K as a function of milling time.

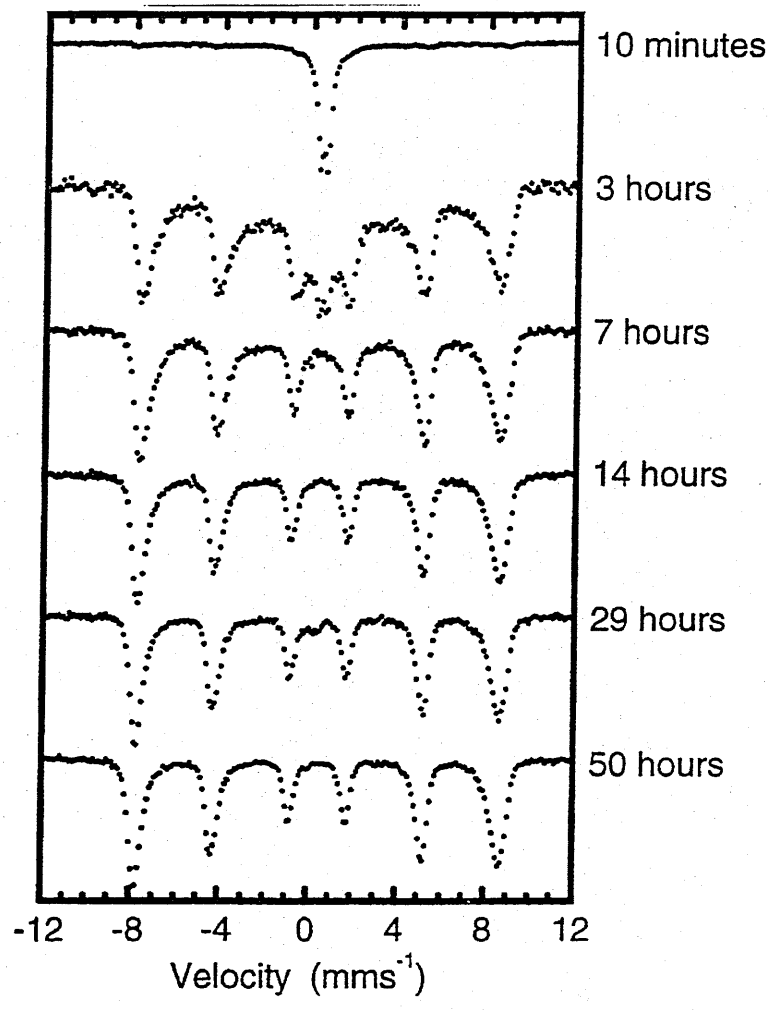

Figure 5.2.6 - ^{57}Fe Mössbauer spectra recorded at 15K from samples of $ZnFe_2O_4$ milled for periods of between 10 minutes and 50 hours.

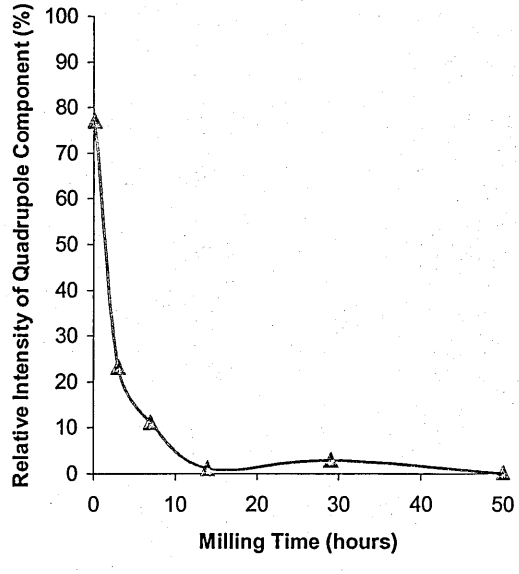

Figure 5.2.7 - Variation of intensity of quadrupole split component in ^{57}Fe Mössbauer spectra recorded from $ZnFe_2O_4$ at 15 K as a function of milling time

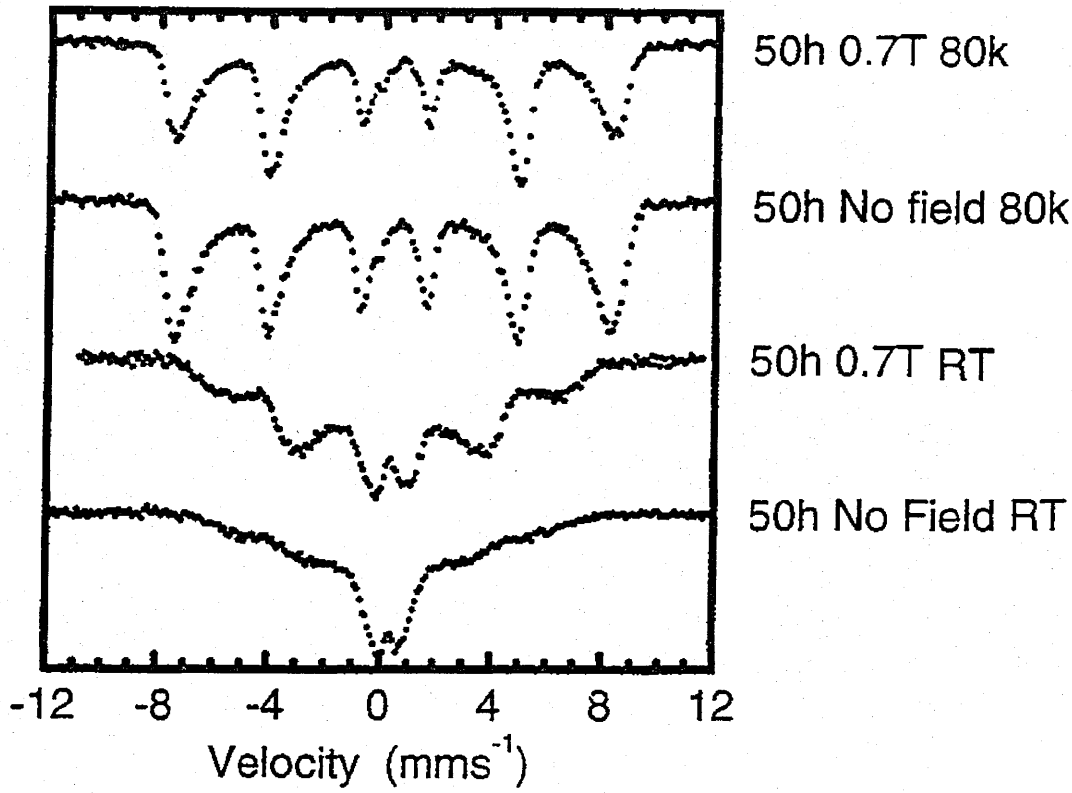

Figure 5.2.8 - ^{57}Fe Mössbauer spectra recorded at 295 K and 80 K from zinc ferrite ball milled for 50 hours, in a magnetic field of 0.7 Tesla, applied perpendicular to the γ-ray direction and compared to those recorded in the absence of an applied external magnetic field.

5.3 Effect of annealing ball milled $ZnFe_2O_4$

X-ray powder diffraction patterns recorded from $ZnFe_2O_4$ which had been ball milled for 50 hours, and annealed at various temperatures between 25 °C and 600 °C for 2 hours are shown in Figure 5.3.1. The position of reflections from these materials coincided with those reported in the literature[89] from $ZnFe_2O_4$ and did not significantly alter throughout the experiment. The absence of reflections corresponding to zinc oxide and iron oxide demonstrate that no decomposition of the zinc ferrite occurred. The reflections within the X-ray powder diffraction patterns narrowed and became sharper as the temperature at which the materials were calcined increased, presumably as the result of thermally induced sintering of the small particles formed by mechanical milling. The ^{57}Fe Mössbauer spectra recorded at 295K from samples annealed at temperatures between 200 °C and 600 °C are shown Figure 5.3.2. The spectrum recorded after heating at 300 °C for 2 hours showed a reduction in the intensity of the magnetically split component and a corresponding increase in the intensity of the quadrupole split component. Following annealing at 600 °C for 2 hours the quadrupole split absorption accounted for the whole of the spectral area as demonstrated in Figure 5.3.3. These results indicate the thermally induced redistribution of Fe and Zn cations to form a *normal* spinel-related structure in a reversal of the processes induced by mechanical milling (5.2.).

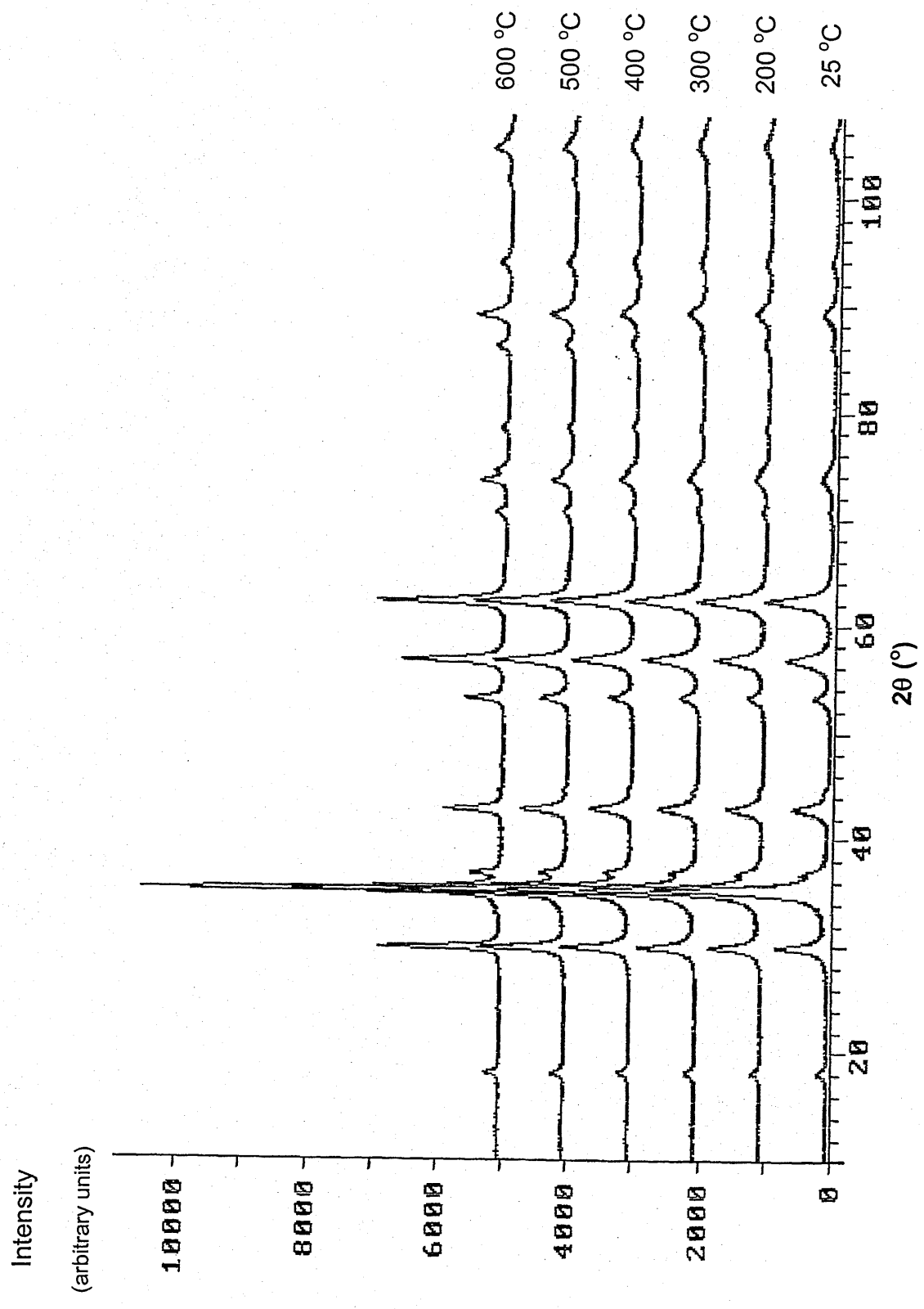

Figure 5.3.1 - X-ray powder diffraction patterns recorded from $ZnFe_2O_4$ which had been ball milled for 50 hours, following annealing in air at temperatures between 200 and 600 °C .

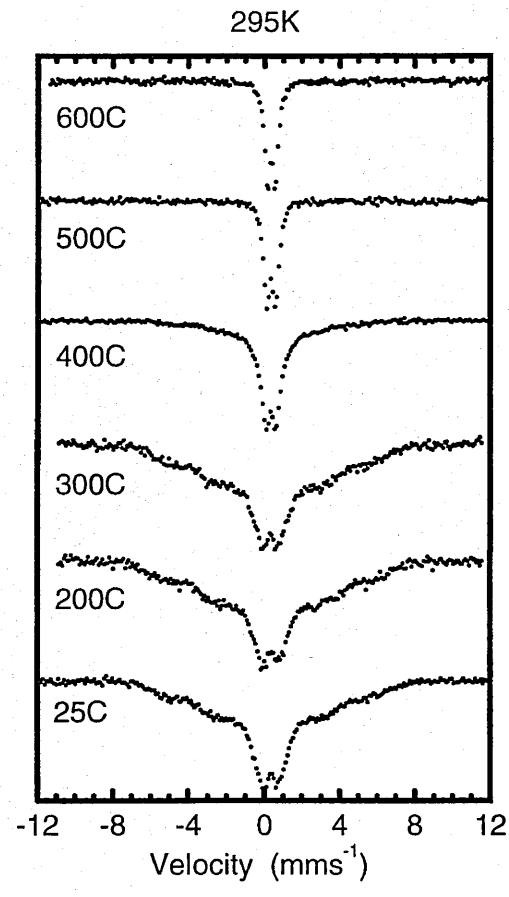

Figure 5.3.2 - ^{57}Fe Mössbauer spectra recorded at 295K from ball milled $ZnFe_2O_4$ following annealing at temperatures between 200 °C and 600 °C.

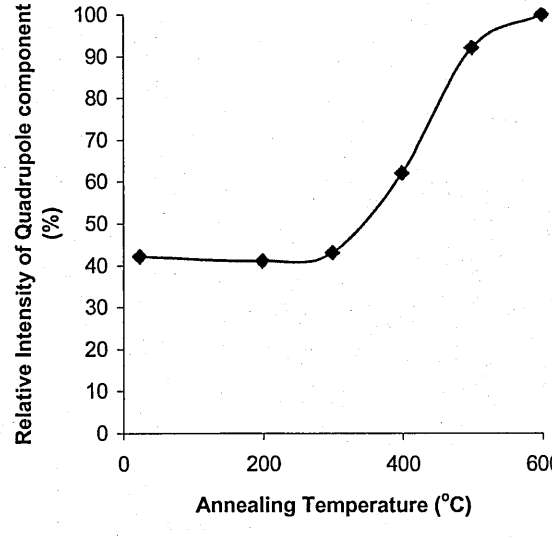

Figure 5.3.3 - Intensity of quadrupole split component in ^{57}Fe Mössbauer spectra recorded at 295 K from ball milled $ZnFe_2O_4$ as a function of subsequent annealing temperature.

5.4 Effect of milling ZnO and MO150 (γ-Al(OH)$_3$)

The results reported in Sections 5.1 and 5.2 indicate the possibility of mechanical milling inducing a reaction between structurally unrelated oxides to form mixed oxides with different structures. No evidence was obtained by X-ray powder diffraction during the work described in Section 4.3 for the formation of spinel-related $CoAl_2O_4$ by the mechanical milling of cobalt- and aluminium-oxides. However, it must be acknowledged that X-ray powder diffraction techniques are not sensitive to subtle changes in the coordination of either cobalt or aluminium which might be induced by milling and which might be associated with the more facile reactions induced by calcination of the pre-milled mixtures (Section 4.3).

A technique more suitable for monitoring any changes in coordination induced by mechanical milling is magic angle spinning (MAS) nuclear magnetic resonance (NMR) spectroscopy. However, the paramagnetic nature of cobalt precludes an examination by ^{27}Al NMR spectroscopy of mixtures containing cobalt- and aluminium-oxides.

In order to determine if the action of milling alone has the potential to evoke a reaction between CoO and γ-Al(OH)$_3$ (MO150) an experiment was performed using ZnO as a model for CoO. ZnO has a rock salt-related structure similar to that of CoO, the high temperature phase formed during heating of Co_3O_4. Hence replacement of cobalt oxide by zinc oxide which is not paramagnetic, allows modelling of the cobalt system and the ^{27}Al MAS NMR spectrum can be recorded to elucidate information about the milling induced changes in co-

ordination of aluminium atoms. This in turn may give clues to those changes induced in the aluminium- and cobalt-containing system.

The X-ray powder diffraction patterns recorded from a mixture of ZnO and MO15O after ball milling for up to 24 hours are shown in Figure 5.4.1. As milling time increased, the X-ray powder diffraction patterns show broadening and flattening of those reflections associated with γ-$Al(OH)_3$ but very little change to the reflections associated with ZnO.

The ^{27}Al solid state MAS NMR spectra recorded from samples milled for up to 24 hours are shown in Figure 5.4.2. The non-milled sample showed a peak at *ca.* 0 ppm with spinning side bands, indicative of the octahedrally co-ordinated aluminium nuclei expected for aluminium in γ-$Al(OH)_3$. As milling time increased the formation of a small peak at *ca.* 30 ppm was observed, indicative of tetrahedrally co-ordinated aluminium nuclei. These data are consistent with the onset of a precursor to the formation of spinel-related $ZnAl_2O_4$. These results demonstrate that there is the potential for $CoAl_2O_4$ formation during the milling of cobalt- and aluminium-oxides.

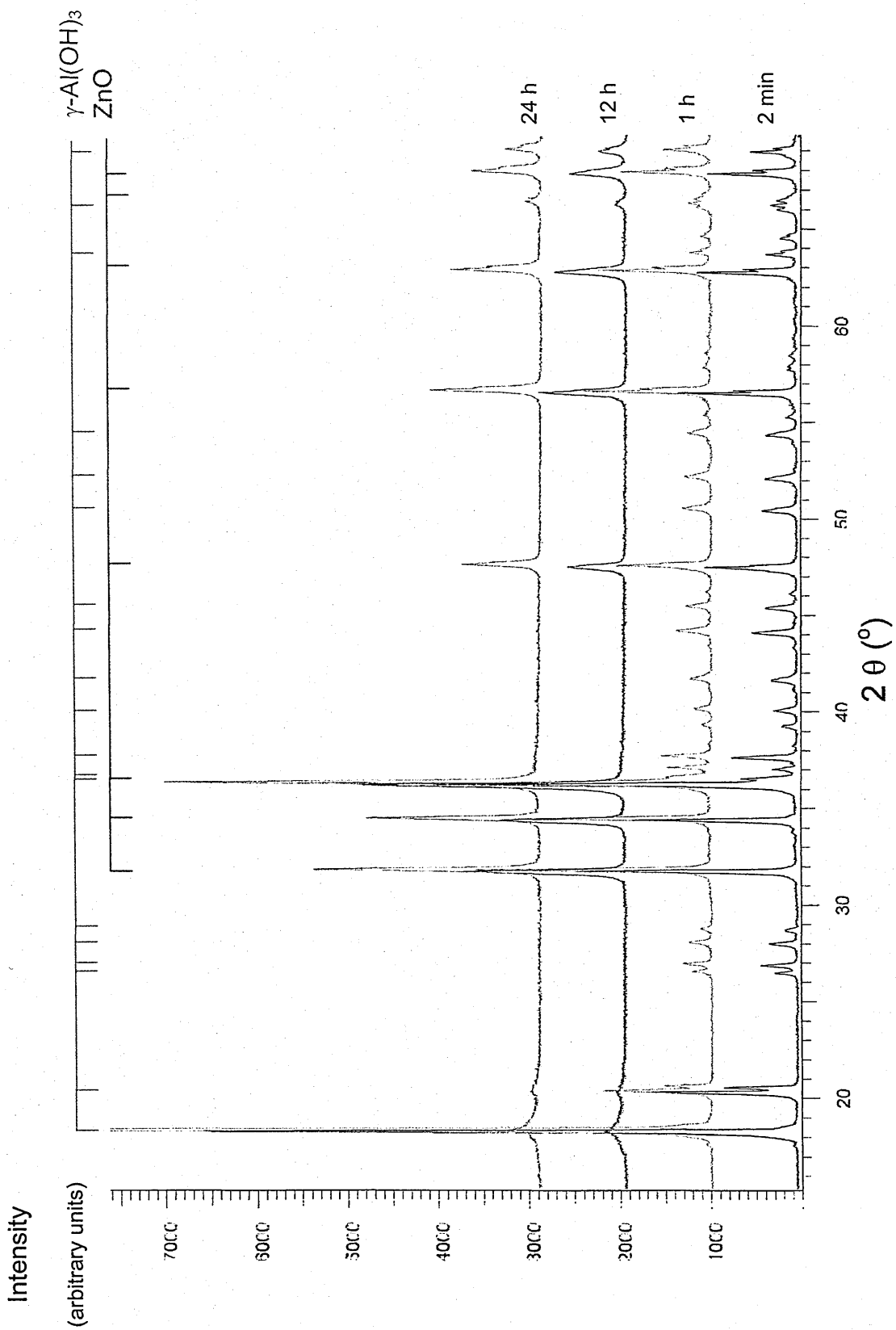

Figure 5.4.1. X-ray powder diffraction patterns recorded from a mixture of ZnO and MO150 (γ-Al(OH)$_3$) after ball milling for up to 24 hours.

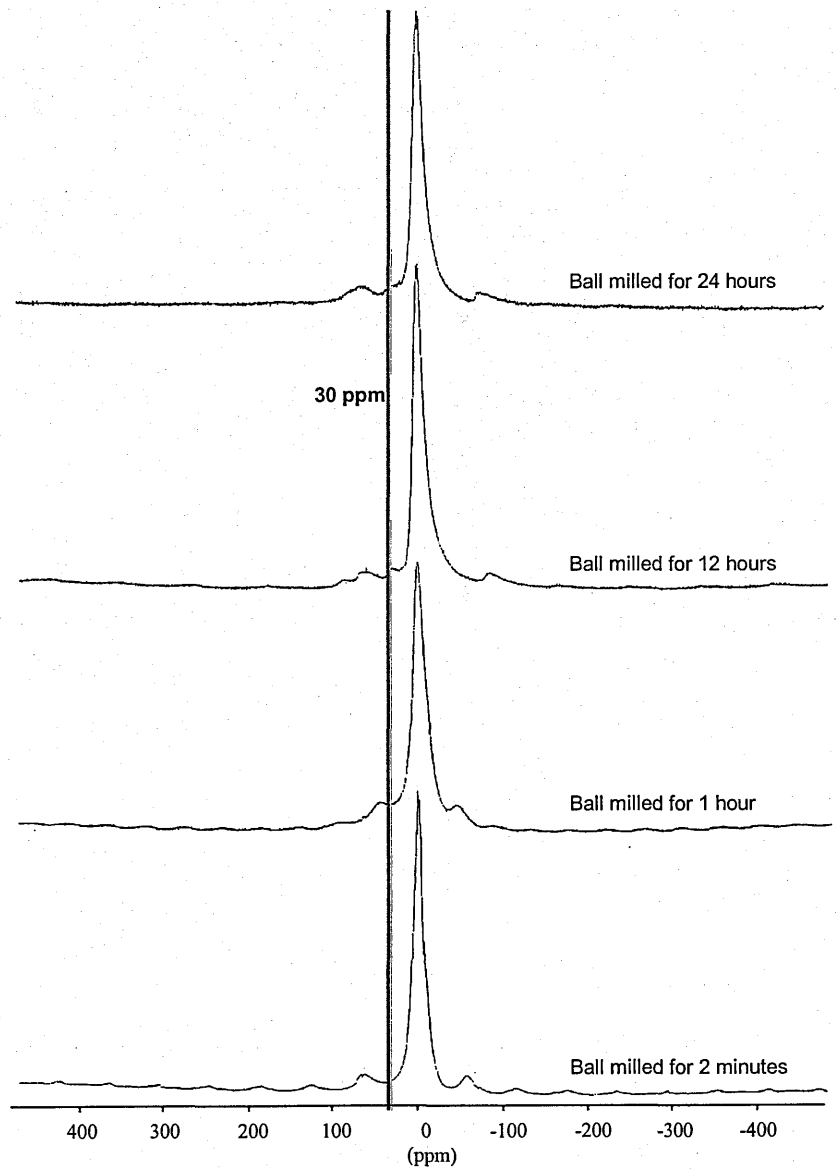

Figure 5.4.2. MAS NMR spectra recorded from samples of ZnO and MO150 (γ-Al(OH)$_3$) after milling for up to 24 hours.

In summary of the work reported in chapter 5,

- Mechanical milling can be used to prepare perovskite related materials of the type $CaMO_3$ (M= Sn, Ti) from rock salt-related CaO and either rutile-related TiO_2 or SnO_2 or from anatase structured TiO_2.

- The ease by which the perovskite-related $CaTiO_3$ structure can be prepared depends on the polymorph of TiO_2 used in the milling process.

- The milling of normal-spinel-related $ZnFe_2O_4$ produces an inversion of the structure that can be reversed by mild thermal annealing.

- The milling of ZnO and MO150 (γ-$Al(OH)_3$) has been monitored by ^{27}Al MAS NMR spectroscopy and the results are consistent with the onset of formation of a precursor to spinel-related $ZnAl_2O_4$. This suggests that an analogous effect may be possible in the CoO / γ-$Al(OH)_3$ system, which is responsible for the more facile formation of $CoAl_2O_4$ from pre-milled mixtures of aluminium- and cobalt-containing oxides.

Chapter 6

Conclusions and Further Work

6.1 Conclusions

The calcination in air of Co_3O_4 induces reduction to CoO. Cooling in air leads to re-oxidation, the extent of which is determined by the conditions of the cooling process. γ-$Al(OH)_3$ is initially converted to γ-AlO(OH) which is subsequently converted via transitional alumina phases to α-Al_2O_3.

Calcination in air of aluminium-oxides, -oxyhydroxides or –hydroxides with Co_3O_4 gives rise to spinel-related $CoAl_2O_4$. The extent of the reaction and the conditions under which the reaction reaches completion reflect the nature of the reactants. The intensity of the blue colour of $CoAl_2O_4$ is influenced by the purity of the product.

Pre-milling of cobalt- and aluminium-oxide, -oxyhydroxide or -hydroxide reactants renders the formation by calcination in air a more facile process.

The formation of monophasic materials in the solid solution series $Co_xAl_{3-x}O_4$ was not successful.

Perovskite-related nanoparticle calcium stannate and calcium titanate ($CaMO_3$, M = Sn, Ti) have been prepared by the mechanical milling of 1:1 mixtures of calcium (II) oxide with either tin (IV) oxide or titanium (IV) oxide. The milling of the rutile modification of titanium dioxide with calcium (II) oxide gives $CaTiO_3$ in a shorter period of time than an analogous experiment using the anatase modification of titanium dioxide. The anatase form of titanium dioxide is readily converted to the rutile form by mechanical milling.

Nanoparticle partially inverted spinel-related zinc ferrite, $ZnFe_2O_4$, has been synthesised by the mechanical milling of bulk normal spinel-related zinc

ferrite. The process induces a change from antiferromagnetic to ferro- or ferri-magnetic zinc ferrite.

The mechanical milling of γ-$Al(OH)_3$ with zinc (II) oxide induces a partial change in the local coordination around aluminium from octahedral to tetrahedral. The results may have implications for the more facile formation of $CoAl_2O_4$ by calcination of pre-milled mixtures of cobalt- and aluminium-oxides.

6.2 Further work

1. Monitoring by ^{27}Al MAS NMR spectroscopy of the effect of mechanical milling on the local environment of aluminium in (i) pure γ-$Al(OH)_3$, γ-AlO(OH) and α-Al_2O_3 phases, and (ii) such phases when mixed with other cations which would form spinel-related structures.
2. Further investigation by a combination of ^{27}Al MAS NMR spectroscopy and Zn K-edge EXAFS of milled mixtures of zinc- and aluminium-oxides, -oxyhydroxides and –hydroxides to elucidate changes in the local coordination around aluminium and zinc induced by mechanical milling.
3. Investigations by ^{27}Al MAS NMR spectroscopy and Zn K-edge EXAFS of milled mixtures of zinc- and aluminium-oxides, -oxyhydroxides and -hydroxides following calcination to elucidate further influences of pre-milling on the ease of formation and nature of products formed by subsequent calcination.
4. Application of knowledge gained from 1 - 3 above, to elucidate the mechanism of the reaction between cobalt- and aluminium-oxides, -oxyhydroxides and -hydroxides during the formation of cobalt aluminate with an exceptional blue colour.

5. Investigation by Zn K-edge and Fe K-edge EXAFS of changes in local coordination around zinc and iron induced by milling normal spinel-related zinc ferrite and relating this to the mechanically induced inversion of the structure.
6. Investigation by Zn K-edge and Fe K-edge EXAFS of changes in local coordination around zinc and iron in inverse spinel-related zinc ferrite, upon subsequent annealing and relating this to the thermally induced normalisation of the structure.
7. Investigation of whether more complex perovskite-related phases such as those with a K_2NiF_4-type structure can be formed using milling techniques.
8. Investigate the effects of ultra-high pressure upon the thermal preparation of perovskite-related structures using a high temperature diamond anvil relating these results to those effects observed in the high-energy ball mill.

REFERENCES

[1] B. Denison, *J. Oil and Colour Chemists Assoc.*, 1990, **73**, 256.

[2] R.M. Davies, B. McDermott, C. Koch, *Metallurgical Trans A.*, 1988,. **19A**, 2867.

[3] J.S. Benjamin, *Metal. Trans.,* 1970, **1**, 2943.

[4] J.S. Benjamin, *Scientific American,* 1976, **234**, 48.

[5] W.E. Kahn, I.L. Friedman, W. Summers and A. Szeguari, *Metals Handbook*, 1984, **7**, 56.

[6] P. Matteazzi and G. Le Caer, *J. Amer. Ceram. Soc.,* 1992, **75**, 2749.

[7] L. Takacs, *Nanonstructured. Mat.* 1993, **2**, 241.

[8] A.Y. Yermakov, *Mater. Sci. Forum.*, 1992, **88**, 577.

[9] H.J. Fecht, *Nanonstructured. Mat.*1992, **1**, 125.

[10] G. Le Caer and P. Matteazzi, *Hyperfine Interactions*, 1994, **90**, 229.

[11] I.J. Lin and S. Nadiv, *Mater. Sci. Eng.*, 1979, **39**, 193.

[12] J.Z. Jiang, C. Gente and R. Bormann, *J. Materials Sci and Engin.* A, 1998, **242**, 268.

[13] J.Z. Jiang, R. Lin, S. Mørup, K. Nielsen, F. Poulsen, F. Berry and R, Clasen, *Phys Rev B.* 1997, **55**, 11.

[14] A. Trovarelli, F. Zamar, J. Llorca, C. Leitenburg, G. Dolcetti and J. Kiss, *J.Catalysis* 1997, **169**, 490.

[15] R. Lin, J.Z. Jiang, R.K. Larsen, S. Mørup and F.J. Berry, *Hyperfine Interactions* (C), 1998, **3,** 45.

[16] H. Zhang and E. Kisi, *J. Phys., Condens. Matter,* 1997. **9**, 185.

[17] D.R. Maurice and T.H. Courtney, *Metal. Trans.,* 1990, **21A**, 289.

[18] H. Huang, J. Pan and P.G. McCormick, *Mater. Sci. and Engineering,* 1997, **A** , 55.

[19] W. Carr, *J. Oil and Colour Chemists Assoc.*,. 1972, **55**, 663.

[20] M. Abdellasni and E. Gaffet, *Mater. Sci. Forum*, 1995, **179**, 339.

[21] J. Uchcrin, R. Uchsin and E.G. Avvakumov, *Mater. Sci. Forum,* 1995, **179**, 425.

[22] V.V. Boldyrev, S.V. Pavlov, V.A. Poluboyarov and A.V. Dushkin, *Inorg. Mat.* 1995, **31**, 1034.

[23] P. Shrewman and G. Sundararajan, *Ann. Rev. Mater. Sci.*, 1997, **13**, 301.

[24] J.S. Benjamin, Scientific America., 1976, **40**, 234.

[25] B. McDermot and C. Koch, *Scripta Metall.*, 1986, **20**, 669.

[26] J.Z.Jiang, S. Linderoth and S. Mørup, *Materials Sci. Forum.,* 1997., **235**., 205.

[27] N.N. Greenwood and A. Earnshaw, "*Chemistry of the Elements".* 1990, Pergamon Press, Oxford. 279.

[28] H. O'Neill, *Eur. J. Mineral.* 1994, **6**, 603.

[29] T. He and K.D. Becker, *Solid State Ionics*, 1997, **101**, 337.

[30] Personal communication, Dr. D. Eden, Cookson Matthey Ceramics, Meir, Stoke –on-Trent

[31] L. Ferrer, M. Seles and J. Alarcón, *Int Ceramics Journal.*, 1995, 18

[32] A.R.West, "*Solid State Chemistry and It's Applications*", John Wiley & Sons, Chichester, 1992.

[33] N.N. Greenwood and A. Earnshaw, *Chemistry of the Elements.* 1990, Pergamon Press, Oxford. p1089.

[34] K. Nassau, *The Physics and Chemistry of Color: The Fifteen Causes of Color*, 2nd Edition John Wiley & Sons, Somerset NJ, 1983.

[35] JCPDS data file 09-0418, Co_3O_4.

[36] P.Garcia Casardo and I.Rasines, *J.Solid State Chem.* 1984, **52**, 187.

[37] D. Bonnenberg. *Landolt-Bornstein numerical values and functions of natural sciences a technical new series*, 1970, **3**, 446.

[38] JCPDS data file 42-1300, CoO.

[39] JCPDS data file 38-0814, Co_2AlO_4.

[40] JCPDS data file 10 458, $CoAl_2O_4$/CoO Al_2O_3.

[41] JCPDS data file 43 1003, Co_3O_4.

[42] N.N. Greenwood and A. Earnshaw, *Chemistry of the Elements*, 1990, Pergamon Press, Oxford, p274.

[43] H. Saalfeld, M. Wedde, Magazine for Crystallography, Crystallgeometry, Crystallphysics, Crystallchemistry, 1974, **139**, 129.

[44] G.G. Christoph, C.E. Corbato, D.A. Hofmann and R.T. Tettenhorst, *Clays and Clay Minerals, 1979,* **27**,81.

[45] B. Winkler, V. Milman, B. Hennion, M.C. Payne, M. Lee and J.S. Lin, *Physics and Chemistry of Minerals*, 1995, **22**, 461.

[46] E.N. Maslen, V.A. Streltsov, N.R. Streltsova, N. Ishizawa and Y. Satow, *Acta Crystallographica B,* 1993, **49**, 973.

[47] K.K. Singh and P.P. Edwards., *Adv. Solid State Chem.,* 1993, **3**, 99.

[48] L.G. Tejuca, M. Vallet-Regí, J.M. González-Calbet and M.A. Alario-Franco., *Acta Cryst. B,* 1986, **42**, 167.

[49] N.N. Greenwood and A. Earnshaw, *Chemistry of the Elements* 1990, Pergamon Press, Oxford. p1122.

[50] R. Hines, N. Allan and W. Flavell, *Philosophical Magazine B*, 1996, **73**, 33.

[51] H. Tang, Y. Du, Q. Qui and J.C. Walker, *J. Appl. Phys.,* 1998, **63**, 4105.

[52] X. Li, G. Lu and S. Li, *J. Alloys and Compounds,* 1996, **235**, 150.

[53] P. Druska, U. Steinike and V. Sepelak, *J. Solid State Chem*, 1999, **146**, 13.

[54] P.K. Baltzer, P.J. Wojtowicz, M. Robbins and E. Lopatin, *Phys. Rev. B.* 1966, **151**, 367.

[55] JCPDS data file 22-1012, $ZnFe_2O_4$.

[56] W. Schiessl, W. Potzel, H. Karzel, M. Steiner and G. Kalvius, *Phys. Rev. B.* 1996, **53**, 9143.

[57] V. Sepelák, K. Tkácová, V. Boldyrev and U. Steinike, *Mat. Sci. Forum.* 1996, **228**, 783.

[58] H. Hamdeh, J. Ho, S. Oliver, R. Willey, G. Oliveri and G. Busca, *J. Appl. Phys.,* 1997, **81**, 1851.

[59] K.Tanaka, M.Makita, Y.Shimizugawa, K.Hirao and N.Soga, *J. Phys. Chem Solids*, 1998, **59**, 1611.

[60] C.Kittel, *"An Introduction to Solid State Physics"*, John Wiley & Sons, New York, 7th Ed., 1996.

[61] M.J.Buerger, *"X-ray Crystallography"*, John Wiley & Sons, New York, 1942.

[62] W.L Bragg, *Proc. Cambridge Phil Soc*, 1913, **17**, 43.

[63] W,Kraus and G.Nozle, PowderCell for Windows v2.3, 1999.

[64] H.P. Klug and L.E Alexander, *"X-ray Diffraction Procedures for Polycrystalline and Amorphous Materials"*, Wiley, 1974.

[65] N.N Greenwood and T.C Gibb, *"Mössbauer Spectroscopy"*, Chapman and Hall, London, 1971

[66] D.P.E Dickson and F.J Berry, "*Mössbauer Spectroscopy*", Cambridge University Press, Great Britain, 1986.

[67] F.J. Berry "*The Mössbauer Effect in Supported Microcrystallites"*, Advances in Inorganic Chemistry and Radiochemistry, vol. 21, Ed. H.J. Emeleus and AG. Sharp, Academic Press, 1978.

[68] D.A.M. Monti and A Baiker, *J. Catal.*, 1983,83,323.

[69] N.W. Hurst, S.J. Gentry, A. Jones and RD. McNicol, *Catal. Rev. Sci. Eng.* 1982,24,233.

[70] N.N. Greenwood, A. Earnshaw, *Chem. of the Elements* 1990, Pergamon Press, Oxford. 1297.

[71] JCPDS data file 04-0802, Platinum, Pt

[72] N.N. Greenwood, A. Earnshaw, *Chem. of the Elements* 1990, Pergamon Press, Oxford. pp 1122, 1296-1297.

[73] JCPDS data file 21-1307, Boehmite, syn, AlO(OH).

[74] N.N. Greenwood, A. Earnshaw, *Chem. of the Elements* 1990, Pergamon Press, Oxford. 273

[75] JCPDS data file 43-1482, Corundum, syn, Al_2O_3.

[76] JCPDS data file 33-0018, Gibbsite, syn, $Al(OH)_3$.

[77] JCPDS data file 44-0160, Cobalt aluminium oxide, $CoAl_2O_4$.

[78] JCPDS data file 09-0402, Cobalt oxide, CoO.

[79] P.Garcia Casardo, I.Rasines, *J.Solid State Chem.* 1984 52, 187-193.

[80] JCPDS data file 04-0777 – Lime, CaO.

[81] JCPDS data file 21-1250 – Cassiterite, SnO_2.

[82] JCPDS data file 31-0312 – Calcium tin oxide, $CaSnO_3$.

[83] JCPDS data file 44-1481 – Portlandite/ Calcium hydroxide, $Ca(OH)_2$.

[84] JCPDS data file 21-1272 – Anatase / TiO_2.

[85] JCPDS data file 03-0808 – Perovskite / Calcium titanium oxide, $CaTiO_3$.

[86] JCPDS data file 21-1276 – Rutile / TiO_2.

[87] S.Bégin-Colin, T.Girot, G.Le Caer and A.Mocellin, *J.Solid State Chem.* 2000, **149**, 41.

[88] R.I.Hines, N.L.Allan and W.R.Flavel, *Phil. Mag.* **B**.,1996, 73, 33.

[89] JCPDS data file 22-1012 – Franklinite, $ZnFe_2O_4$.

[90] K.Tkacova, V.Sepelak, N.Stevulova, and V.V.Boldyrev, *J. Solid State Chemistry*, 1996,**123**, 100.